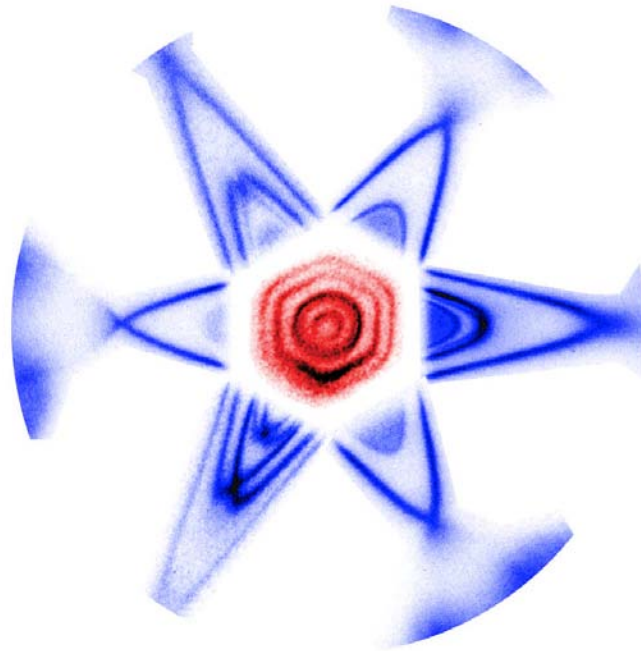


AARHUS UNIVERSITY  
DEPARTMENT OF PHYSICS AND ASTRONOMY

PHD THESIS

**Electronic structure and electron  
dynamics of the topological insulator  
 $\text{Bi}_2\text{Se}_3$**



PHD STUDENT:  
Marco Bianchi

SUPERVISOR:  
Prof. Philip Hofmann

ACADEMIC YEAR 2012-2013



# Acknowledgments

In Science, like in other fields, the interactions between researchers are both vital and fundamental for scoring an innovative and competitive result. Furthermore when people are seriously committing themselves to reality, the great humanity brought forth always impresses. For this reason it is important to mention my gratitude to all the people who have accompanied me or have been involved in the projects presented in this thesis making it possible.

First of all, I would like to express my gratitude to Philip Hofmann whose teaching and guidance have inspired and corrected each step of this research on a daily basis and whose humanity has been of great support. Edward W. Perkins must also be mentioned as he has followed and shared with me life and work on the beamline, and whose patience and precision have been decisive also in proofreading the thesis. I would like to thank all the members of our group (past and present) and in particular: Dandan G., Federico M., Jens C. J., Lucas M. A. B., Richard C. H., Søren U. and Wendell S. S. Furthermore I thank all the ISA staff and the workshops for their assistance and confidence allowing me to use all the equipment whenever I needed, in particular: Jens V., Kate A., Lone T., Niels H., Nikola J., Peter L., Søren V. H., Torben H. T. and Zheshen L. From all the collaborators a great deal of teaching, help and suggestions came and especially from: A. Baraldi, M. Bode, P.D.C. King, S. Lizzit, J. Mudd, E. Rienks, A. Stróżecka and J. Wells.

Secondly, I would like to thank all my friends and in particular: Bernardo, Dainius, Daniela, Filippo & Chiara, Gabriele, Giampaolo, Greg, Jonathan, Lynn, Maria, Milagros, Oksana, Piermatteo, Raffaella and Silvia. Without their presence my stay here would have been much less enjoyable.

Last, but most important, are my warmest thanks to both my wife Roberta for her support and patience, and to our families.

# Preface

The research presented in this dissertation was conducted from November 2009 to December 2012. The official enrolment in the PhD program at the Aarhus Graduate School of Science was accepted from August 2009.

The work was performed under the supervision of: **Professor Philip Hofmann**

*Department of Physics and Astronomy, Interdisciplinary Nanoscience Center, Aarhus University, 8000 Aarhus C, Denmark.*

This thesis is submitted to the Faculty of Science at Aarhus University in order to fulfil the requirements for obtaining a PhD degree in physics. The work has been carried out primarily at the Department of Physics and Astronomy (IFA) and at the Institute for Storage Ring Facilities in Aarhus (ISA).

This PhD project had two main aims, one didactical and one concerned with pure research. The 3-year project has consequently been divided into two parts, consistent with the scheme of the AGSOS 3-year PhD program.

The first 18 months have been devoted to the acquisition of the appropriate experimental and theoretical know-how concerning angle-resolved photoemission for the study of band structures and life-time, and more generally photoelectron spectroscopy. Experimental and practical skills have been acquired in the main on the SGM 3 beamline on ASTRID but also via the collaboration of the ISA surface science group with the STM group and the Center for Materials Crystallography in Aarhus, the iNANO centre and other international collaborators. During this first period, in parallel with courses and exams that allowed me to acquire the required ECTS credits, I have performed measurements on different systems that for the most part ended up in publications in peer-reviewed journals. In this training period I have assisted external users coming to the SGM 3 beamline and actively trained and supported them in carrying out their tasks. At the same time I have followed an upgrade to the software and macros needed to load and analyse the acquired data.

The second 18 months have been devoted to the experimental work more strictly connected to the subject of my PhD and opening new possible projects, including visiting different European research centres and conferences. In this period I also took care of the upgrade of the end-station in the context of moving it to the new SGM 3 beamline on ASTRID2.

In this dissertation only the main subject of my PhD will be presented, even though I participated in various side-projects in collaboration with other international experimental and theoretical groups.

## Dansk résumé

I de seneste ti år er et nyt forskningsfelt udsprunget af faststoffysikken, som forener den traditionelle viden om overfladetilstande med teorien om topologi. Indenfor topologi forudsiges et væld af nye fysiske fænomener relateret til faste stoffer, hvor især spin-bane interaktionen fører til en ny materiel tilstandsform – en såkaldt topologisk isolator [1, 2, 3]. En topologisk isolator er et materiale, hvor bulken opfører sig som en isolator karakteriseret ved et elektronisk excitationsgab frembragt af spin-bane koblingen, mens elektrontilstande uden excitationsgab kan detekteres ved materialets overflade pga. såkaldt “time reversal” symmetrier [4, 5, 6, 7, 8, 9].

Dette felts nyskabende karakter og mulige vidtrækkende konsekvenser i forskellige forskningsområder er ideelt i konteksten af et PhD studie, idet erfaring med konventionelle eksperimentelle teknikker opbygges og bruges til at udforske nyt territorie. Dette er den grundlæggende motivation for at vælge topologiske isolatorer som overordnet emne for mine PhD studier, der i øvrigt er gennemført med et eksperimentelt fokus.

Adskillige topologiske isolatorer og lignende systemer er blevet undersøgt via teknikken vinkelopløst fotoemissionsspektroskopi, hvor udgangspunktet er et studie af det topologiske ikke-trivielle semi-metal Sb(110). Teknikken er efterfølgende blevet udnyttet til en detaljeret undersøgelse af elektronstrukturen og elektronernes dynamik i  $\text{Bi}_2\text{Se}_3$  – et materiale der anses som prototypen på en topologisk isolator. Den rene overflade udviser topologiske overfladetilstande i båndgabets af bulk materialet samt en aldringseffekt, som forskyder Dirac punktet mod højere bindingsenergier. Det diskuteres, hvordan denne effekt er relateret til kontaminering af overfladen, hvilket fører til en forstærket nedadrettet båndbøjning tæt på overfladen. Denne hypotese understøttes yderligere, idet en række eksperimenter viser, at denne båndbøjningseffekt accelereres, når overfladen eksponeres for kontrollerede mængder af specifikke partikler såsom kulilte. Ydermere observeres dannelsen af kvantebrønds-tilstande i både valens- og ledningsbånd ved forskellig båndbøjning. Kvantebrønds-tilstandene i ledningsbåndet viser sig at være Rashba splittet, og det vises hvordan disse observationer er konsistente med en simpel Schottky model. Dog inddrages også andre fortolkninger. Stabiliteten af den topologiske overfladetilstand er blevet undersøgt med fokus på elektron-fonon koblingsstyrken og elektron-defekt spredning. Det vises også, hvordan kontrolleret magnetisk doping af den topologiske tilstand er muligt via deponering af Fe atomer på den kolde overflade og efterfølgende indlejring i bulken ved opvarmning. Endelig præsenteres en kortlægning af bulk båndstrukturen for  $\text{Bi}_2\text{Se}_3$ .

Et sideløbende projekt i PhD studiet bestod af planlægning og design af en ny endestation til den nye SGM3 beamline ved den kommende synkrotronring ASTRID2. Der gives en detaljeret beskrivelse af denne endestation samt en gennemgang af udviklingen af en ny heliumkølet manipulator med seks frihedsgrader.

# Motivation

The combination of strong spin-orbit interaction and loss of symmetry at surfaces and interfaces often leads to an electronic band structure in which the degeneracy with respect to spin is completely lifted. This is frequently called the Rashba effect and it has emerging applications for spin-filtering and spintronics, as well as implications for the understanding of the intrinsic spin Hall effect and the quantum spin Hall effect [10].

The electronic structure of systems characterised by such a strong spin-orbit splitting is not only of fundamental interest in solid-state physics and spintronics technologies by itself, but in the last ten years a new field has emerged coupling the traditional knowledge of surface states with the theory of topology. The latter predicts a plethora of novel phenomena in condensed matter physics such as Majorana fermions [1], unconventional superconductivity [2] and magnetic monopoles [3], showing that the spin-orbit interaction (SOI) can lead to a new state of matter called topological insulators. A topological insulator is a material with an insulating bulk, characterised by an electronic excitation gap generated by the SOI, while time-reversal symmetry requires the presence of gapless electronic states at the edges (i.e. the surface in three-dimensions) [4, 5, 6, 7, 8, 9].

The novelty of this field represents the perfect opportunity in the context of a PhD study. Because of its wide-ranging character and the possible ramifications in different fields it allows the possibility of high quality professional training which exploits conventional experimental techniques in unexplored fields. For these reasons it has been chosen as the main subject of my PhD studies, which have been pursued with an experimental focus.

# Contents

|   |            |
|---|------------|
| <b>Abstract</b>   | <b>iii</b> |
| <b>1 Basic Theory</b>   | <b>1</b>   |
| 1.1 Bulk and surface-confined electronic states . . . . .                         | 1          |
| 1.1.1 Surface-confined states . . . . .   | 3          |
| 1.1.2 Spin-orbit coupling: From atoms to the crystal . . . . .                    | 5          |
| 1.2 A special family of semiconductors: <i>Topological insulators</i> . . . . .   | 8          |
| 1.2.1 Towards the quantum spin Hall insulator . . . . .                           | 10         |
| 1.2.2 Counting Fermi surface crossings and topology . . . . .                     | 11         |
| 1.2.3 Strong 3D topological insulators: Bismuth chalcogenide alloys . . . . .     | 12         |
| 1.2.4 A topological <i>resumé</i> . . . . .                                       | 13         |
| 1.3 Introduction to photoemission . . . . .                                       | 16         |
| 1.3.1 ARPES: The spectral function $\mathcal{A}(\omega, \mathbf{k})$ . . . . .    | 17         |
| 1.3.2 X-ray spectroscopy: Core levels and line-shape . . . . .                    | 21         |
| <b>2 Experimental Set-up: ARPES at ASTRID</b>                                     | <b>23</b>  |
| 2.1 ASTRID . . . . .  | 23         |
| 2.2 The SGM3 beamline . . . . .   | 25         |
| 2.3 The ARPES end-station . . . . .   | 26         |
| 2.3.1 Mapping the 2D and 3D k-space with the SPECS Phoibos 150 analyser . . . . . | 28         |
| <b>3 Projects and Results</b>   | <b>33</b>  |
| 3.1 Sb(110): Fermi surface mapping and topology . . . . .                         | 33         |
| 3.2 Bi <sub>2</sub> Se <sub>3</sub> , Rashba and quantum well states . . . . .    | 40         |
| 3.2.1 Sample growth and preparation . . . . .                                     | 40         |
| 3.2.2 Basic spectral features . . . . .   | 42         |
| 3.2.3 Confinement of conduction band states . . . . .                             | 45         |
| 3.2.4 Confinement of valence band states . . . . .                                | 53         |
| 3.2.5 Rashba splitting of the conduction band 2DEG . . . . .                      | 59         |
| 3.2.6 Surface doping via alkali deposition . . . . .                              | 63         |
| 3.2.7 Fe on Bi <sub>2</sub> Se <sub>3</sub> . . . . .                             | 70         |
| 3.2.8 Stability of Bi <sub>2</sub> Se <sub>3</sub> . . . . .                      | 74         |
| 3.2.9 Bi <sub>2</sub> Se <sub>3</sub> bulk electronic structure . . . . .         | 79         |
| <b>4 Outlook</b>  | <b>87</b>  |
| 4.1 The new ARPES end-station on ASTRID2 . . . . .                                | 88         |
| 4.1.1 The 6 axis manipulator . . . . .  | 92         |

|                              |           |
|------------------------------|-----------|
| <b>5 Conclusions</b>         | <b>95</b> |
| <b>List of abbreviations</b> | <b>97</b> |

# Abstract

Several topological insulators and similar system have been studied with angle-resolved photoemission spectroscopy as described in the following:

- The surface states on the topologically non-trivial semimetal Sb(110) have been investigated and compared to topological predictions of its Fermi surface. The limits of the applicability of this theory to semimetals is also discussed.
- A thorough study of the electronic structure and electron dynamics of the prototypical topological insulator  $\text{Bi}_2\text{Se}_3$  is presented. Nominally stoichiometric and calcium-doped samples were investigated. The pristine surface shows the topological surface state in the bulk band gap and an ageing effect that moves the Dirac point towards higher binding energies over time.
- The ageing effect is studied and interpreted as an increasingly strong downward bending of the bands near the surface, and this is related to a surface contamination. It is shown how this effect can be accelerated by intentionally exposing the surface to carbon monoxide and other species. For a sufficiently strong band bending, additional states also appear at the Fermi level and are interpreted as quantised conduction band states. For large band bendings these are found to undergo a strong Rashba splitting. The formation of quantum well states is observed also for the valence band states, supporting the hypothesis of band bending, although different interpretations of similar data are also discussed.
- The stability of the topological state is investigated, prior to the ageing effect becoming appreciable. The electron-phonon coupling strength and electron-defect scattering are also discussed in the context of this work.
- The possibility of a controllable magnetic doping of the topological surface state has been investigated through Fe deposition on the cold surface and subsequent incorporation into the bulk through annealing.
- Finally, a mapping of the  $\text{Bi}_2\text{Se}_3$  bulk band structure is presented.

## Keywords:

Surface electronic structure, ARPES, Topological insulator, Sb(110),  $\text{Bi}_2\text{Se}_3$ , band bending, 2DEG, Rashba splitting, electron-phonon coupling.

## Publications relevant for this thesis

1. *Coexistence of the topological state and a two-dimensional electron gas on the surface of  $Bi_2Se_3$* , M. Bianchi, D. Guan, S Bao, J. L. Mi, B. B. Iversen, Philip D. C. King and Ph. Hofmann, **Nature Communications** **1**, 8, 128 (2010).
2. *Stability of the topological state on  $Bi_2Se_3$* , R. C. Hatch, M. Bianchi, D. Guan, B. B. Iversen, J. L. Mi and Ph. Hofmann, **Phys. Rev. B** **83**, 241303(R) (2011).
3. *Large tuneable Rashba spin splitting of a two-dimensional electron gas in  $Bi_2Se_3$* , P. D. C. King, R. C. Hatch, M. Bianchi, R. Ovsyannikov, C. Lupulescu, G. Landolt, B. Slomski, J. H. Dil, D. Guan, J. L. Mi, E. D. L. Rienks, J. Fink, A. Lindblad, S. Svensson, S. Bao, B. B. Iversen, W. Eberhardt, F. Baumberger, and Ph. Hofmann, **Phys. Rev. Lett.** **107**, 096802 (2011).
4. *Simultaneous quantization of bulk conduction and valence states through adsorption of nonmagnetic impurities on  $Bi_2Se_3$* , R. C. Hatch, M. Bianchi, D. Guan, B. B. Iversen, J. L. Mi and Philip Hofmann, **Phys. Rev. Lett.** **107**, 086802 (2011).
5. *Surface states on a topologically non-trivial semimetal: The case of  $Sb(110)$* , M. Bianchi, D. Guan, A. Strozecka, C. H. Voetmann, S. Bao, J. I. Pascual, A. Eiguren, Ph. Hofmann, **Phys. Rev. B** **85**, 155431 (2012).
6. *Robust surface doping of  $Bi_2Se_3$  by Rb intercalation*, M. Bianchi, R. Hatch, Z.S. Li, Ph. Hofmann, F. Song, J. Mi, B. B. Iversen, M. Z. Abd El-Fattah and J.W. Wells, **ACS Nano** **8**, 7009-15 (2012).
7. *The electronic structure of clean and adsorbate-covered  $Bi_2Se_3$ : an angle-resolved photoemission study*, M. Bianchi, R.C. Hatch, D. Guan and Ph. Hofmann, **Semicond. Sci. Technol.** **27** 124001(2012).
8. *Controllable magnetic doping of the surface state of a topological insulator*, T. Schlenk, M. Bianchi, M. Koleini, A. Eich, O. Pietzsch, T. O. Wehling, T. Frauenheim, A. Balatsky, J. L. Mi, B. B. Iversen, J. Wiebe, A. A. Khajetoorians, Ph. Hofmann, R. Wiesendanger, **Phys. Rev. Lett.** (accepted).
9. *Evidence for a direct band gap in the topological insulator  $Bi_2Se_3$  from theory and experiment*, I. A. Nechaev, R. C. Hatch, M. Bianchi, D. Guan, C. Friedrich, J. L. Mi, B. B. Iversen, S. Blügel, Ph. Hofmann and E. V. Chulkov, (submitted).

## Other publications

1. *Surface core level shifts of clean and oxygen covered  $Ir(111)$* , M. Bianchi, D. Cassese, A. Cavallin, R. Comin, F. Orlando, L. Postregna, E. Golfetto, S. Lizzit and A. Baraldi, **New Journal of Physics** **11**, 063002 (2009).
2. *Electron-phonon coupling in potassium-doped graphene: Angle-resolved photoemission spectroscopy*, M. Bianchi, E. D. L. Rienks, S. Lizzit, A. Baraldi, R. Balog, L. Hornekær, and Ph. Hofmann, **Phys. Rev. B** **81**, 041403(R) (2010).
3. *Band Gap Opening in Graphene Induced by Patterned Hydrogen Adsorption*, R. Balog, B. Jørgensen, L. Nilsson, M. Andersen, E. Rienks, M. Bianchi, M. Fanetti, E. Lægsgaard, A. Baraldi, S. Lizzit, Z. Sljivancanin, F. Besenbacher, B. Hammer, T. G. Pedersen, Ph. Hofmann and L. Hornekær, **Nature Materials** **9**, 315–319 (2010).

4. *Strongly enhanced electron-phonon coupling in the Rashba-split state of the Bi/Ag(111) surface alloy*, D. Guan, M. Bianchi, S. Bao, E. W. Perkins, F. Meier, J. H. Dil, J. Osterwalder, and Ph. Hofmann, **Phys. Rev. B** **83**, 155451 (2011).
5. *High-temperature behaviour of supported graphene: electron-phonon coupling and substrate-induced doping*, S. Ulstrup, M. Bianchi, R.C. Hatch, D. Guan, A. Baraldi, D. Alfè, L. Hornekær and Ph. Hofmann, **Phys. Rev. B** **86**, 161402(R) (2012).
6. *Transfer-Free Electrical Insulation of Epitaxial Graphene from its Metal Substrate*, S. Lizzit, R. Larciprete, P. Lacovig, M. Dalmiglio, F. Orlando, A. Baraldi, L. Gammelgaard, L. Barreto, M. Bianchi, E. W. Perkins, and Ph. Hofmann, **Nano Letters** **12**, issue 9, pp. 4503-4507 (2012).
7. *Oxygen Switching of the Epitaxial Graphene-Metal Interaction*, R. Larciprete, S. Ulstrup, P. Lacovig, M. Dalmiglio, M. Bianchi, F. Mazzola, L. Hornekær, F. Orlando, A. Baraldi, Ph. Hofmann and S. Lizzit, **ACS Nano** **6** (11), pp 9551–9558 (2012).
8. *Phase Separation and Bulk p-n Transition in Single Crystals of Bi<sub>2</sub>Te<sub>3</sub>Se Topological Insulator*, J.L. Mi, M. Bremholm, M. Bianchi, K. Borup, S. Johnsen, M. Søndergaard, D. Guan, R. C. Hatch, Ph. Hofmann and B. B. Iversen, **Advanced Materials**, (in press).
9. *Electron-phonon coupling in quasi free-standing graphene*, J.C. Johannsen, S. Ulstrup, M. Bianchi, R.C. Hatch, D. Guan, F. Mazzola, L. Hornkær, F. Fromm, C. Raidel, T. Seyller and Ph. Hofmann, **J. Phys. Condens. Matter**, (in press).
10. *Phase Separation and Bulk p-n Transition in Single Crystals of Bi<sub>2</sub>Te<sub>3</sub>Se Topological Insulator*, J.L. Mi, M. Bremholm, M. Bianchi, K. Borup, S. Johnsen, M. Søndergaard, D. Guan, R. C. Hatch, Ph. Hofmann and B. B. Iversen, **Advanced Materials**, (in press).
11. *Electron-phonon coupling in the two-dimensional electron gas on Bi<sub>2</sub>Se<sub>3</sub>*, L. Barreto, M. Bianchi, D. Guan, R. C. Hatch, J. Mi, B. B. Iversen and Ph. Hofmann (submitted).



# Chapter 1

## Basic Theory

In order to understand the electronic dispersion of electrons in solids one should solve the general Schrödinger equation for the whole system of electrons and atoms including the interactions. This problem immediately becomes too complicated to be handled without simplification, and for this reason a thorough introduction to the electronic structure of solids starts typically from the Drude model, passing through a quantum mechanical treatment of free independent electrons, introducing then a periodic potential representing the atoms placed in the ordered array of the crystal and so on. All this is beyond the task of this dissertation and it has already been done masterfully by the giants of solid state physics and can be found in these well known text books [11, 12, 13, 14].

The more advanced theory needed to understand the systems and properties we are interested in is varied and complex, spanning from topology, passing through many-body theory towards more frontier surface science. Therefore the following section only recalls the most elementary concepts and definitions needed in order to understand what will be presented in this work. For the sake of brevity what follows has to be considered just a summary condensing the classic literature. Deeper and more complete information can be found in the cited literature from which this chapter is genuinely and frankly inspired.

### 1.1 Bulk and surface-confined electronic states

In a naive picture, electrons in a solid can be grouped into two classes: the strongly bound electrons making up the inner atomic orbitals (core levels), modified to some degree by the local chemical environment, and the less bound ones (valence electrons) making up the bands, which lead to the particular electronic properties of the solid.

While in a single atom an electron is allowed to occupy a localised state in energy, if it is placed in a periodic potential generated by  $N_a$  atoms placed in an ordered array (the crystal) the allowed energy levels become continuous within a certain range. A bulk band is therefore nominally a subset indexed by  $n$  of allowed electronic eigenvalues  $\epsilon_n(\mathbf{k})$  in the solid. The conceptual pillar in this context is the Bloch theorem [11] which describes the wavefunction (w.f.) as

$$\psi_{\mathbf{k}}(\mathbf{r}) = u_{\mathbf{k}} \exp(i\mathbf{k} \cdot \mathbf{r}) . \quad (1.1)$$

These are solutions of the Schrödinger equation for electrons in a periodic potential  $U(\mathbf{r})$

$$\left(-\frac{\hbar^2}{2m}\nabla^2 + U(\mathbf{r})\right)\psi(\mathbf{r}) = \epsilon\psi(\mathbf{r}) . \quad (1.2)$$

The potential  $U(\mathbf{r})$  depicts the periodic array of atoms in the crystal described by a Bravais lattice. The periodicity in the real and reciprocal space of this is determined by the vectors  $\mathbf{R}$  and  $\mathbf{G}$  respectively. Therefore  $U(\mathbf{r})$  is modelled so as to follow the relation  $U(\mathbf{r}) = U(\mathbf{r} + \mathbf{R}) = \sum_{\mathbf{G}} U_{\mathbf{G}} e^{i\mathbf{G}\cdot\mathbf{r}}$ .

In this notation  $u_{\mathbf{k}}(\mathbf{r}) = u_{\mathbf{k}}(\mathbf{r} + \mathbf{R})$  gives the w.f. a periodicity related to the one of the lattice. Consequently it is possible to rewrite Eq. 1.2 in a more compact way as  $\mathcal{H}\psi_{\mathbf{k}} = \epsilon_{\mathbf{k}}\psi_{\mathbf{k}}$ . What is relevant here is the number of unit cells ( $N$ ). Where  $N$  is large enough, as happens in a solid, the index  $\mathbf{k}$  becomes basically continuous, and so do the solutions,  $\epsilon(\mathbf{k})$ . Furthermore, as we will possibly have more than one solution for the same  $\mathbf{k}$ , we can introduce a new index that will be called the *band index*  $n$  and the Bloch w.f. can be written as  $\psi_{n,\mathbf{k}}(\mathbf{r}) = u_{n,\mathbf{k}} \exp(i\mathbf{k} \cdot \mathbf{r})$ .

The number of allowed bands ( $n = 1, 2, 3, \dots$ ) in a solid can be in principle infinite, but most of them lie at such high energies that an electron in those states would be virtually free. It is also useful to remember the definition of the Fermi energy ( $E_F$ ) as the energy of the highest occupied level (FL) at zero temperature.

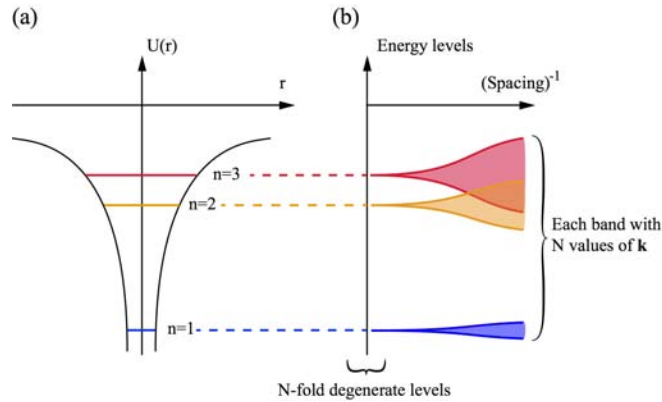


Figure 1.1: (a) Schematic representation of non-degenerate levels in the atomic potential  $U(r)$  and (b) how the band can be generated, in the case of  $N$  unit cells depicted as a function of the inverse interatomic distance [11].

An intuitive and popular method to calculate the  $\epsilon_n(\mathbf{k})$ , i.e. the relation between energy distribution and momentum  $\mathbf{k}$  of the electrons in the solid, is the *tight-binding* (TB) model [11]. The name already describes the basic approximation it relies on, considering the electrons tightly bound to the atoms rather than as a free electron gas. This is expressed in the assumption that  $\mathcal{H} \approx \mathcal{H}_{\text{at}} + \Delta U$  where  $\mathcal{H}_{\text{at}}$  is the single atomic orbital Hamiltonian and  $\Delta U$  accounts for the correction due to the complete periodic potential of the lattice. If periodic boundary conditions are introduced, it is possible to build the electronic state of the solid  $\psi_n$  through a linear combination of the (known) atomic solutions. The larger the interatomic distance ( $a$ ) the better the approximation will be. However a fundamental correction term has to be considered representing the overlap ( $S$ ) between adjacent orbitals. Therefore the method can be summarised in the following steps:

1. Nearby the atoms in the lattice the Hamiltonian of the crystal is  $\mathcal{H} \approx \mathcal{H}_{\text{at}}$ ;
2. Assume that the bound levels of  $\mathcal{H}_{\text{at}}$  are  $\mathcal{H}_{\text{at}}\psi_n = E_n\psi_n$ ;
3. Assume that the bound levels are well localised  $|\psi_n(\mathbf{r})|^2 \xrightarrow{r \rightarrow \infty} 0$ .

How the bands derive from the atomic orbitals is presented in Fig. 1.1, reproduced from Ref. [11] where a more exhaustive treatment can be found.

Now that the idea of bulk bands has been briefly discussed, it is possible to consider what happens if the surface is introduced, i.e. a more or less abrupt termination of the crystal periodicity in a certain direction described by the Miller indices<sup>1</sup>.

A first approximation to model the presence of the surface is the so-called *jellium model* [11, 15]. In this model each atom donates  $q$  electrons to the valence band, remaining charged with  $e(Z - q)$ ,  $Z$  being the atomic valence number. The ions in the lattice are then described by a uniform positive background charge. The average charge density can be calculated as  $\bar{n} = e(Z - q)/V = e/\frac{4}{3}\pi r_s^3$ , where  $V$  is the volume of the Wigner-Seitz cell while  $r_s$  is the radius of the sphere whose volume is occupied by the valence electrons.

In this context the surface can be modelled as a step-like change in this positive background, leading to two effects. The first is the spilling out into vacuum of the electron charge density. The electron charge density also exhibits a fluctuation as a function of distance from the step, called a Friedel oscillation. These oscillations arise due to the inability of the electrons to screen perturbations with Fourier components larger than twice the Fermi momentum ( $2k_F$ ).

The second effect consists of the possible relaxation, i.e. a compression or expansion, of the interlayer distance near the surface. This can be related to the fact that the density of charge is actually smoother than the one expected considering only the Wigner-Seitz cell, an effect that is commonly referred to as the Smoluchowski effect.

Once the surface is created a preferential axis orientation can be defined. Through all the following work the axis  $z$  or  $k_z$  will always be referred to as the one orthogonal to the surface unless stated otherwise. Similarly it will be  $\mathbf{k} = (k_x, k_y, k_z) = (k_{||}, k_z) = (\vec{k}, k_z)$ , where  $x$  and  $y$  live in the plane parallel to the surface. With  $k_{||}$  will indicate either  $k_x$  or  $k_y$  meaning that the particular orientation in the surface plane is not relevant.

### 1.1.1 Surface-confined states

Looking at the surface from the wavefunction point of view, the Hamiltonian can be considered basically unchanged in the direction parallel to the surface, while the symmetry is broken in the orthogonal one. This symmetry breaking can lead to new solutions of the Schrödinger equation, giving rise to states residing only at the surface. Given the presence of the surface, all the states have to be matched with an exponential decay into the vacuum (see Fig. 1.2). Regarding the crystal side, qualitatively, we can consider a Bloch w.f. as in Eq. 1.1. If we let  $\mathbf{k} \in \mathbb{C}$ , and more precisely  $k_z = \kappa \in \mathbb{C}$ , leaving  $\vec{k}_{||}$  unchanged, it is possible to find a solution that can match the exponential decay in vacuum and an exponential decay of the oscillation inside the solid (a solution with an exponential growth of the w.f. oscillation inside the solid is unphysical). Such a state can be written as

$$\psi_{\mathbf{k}} = u_{\vec{k}_{||}}(\vec{r}_{||})e^{i\vec{k}_{||}\vec{r}_{||}}e^{-\kappa r_{\perp}} \quad . \quad (1.3)$$

---

<sup>1</sup>A definition can be found on pg. 91 of Ref. [11].

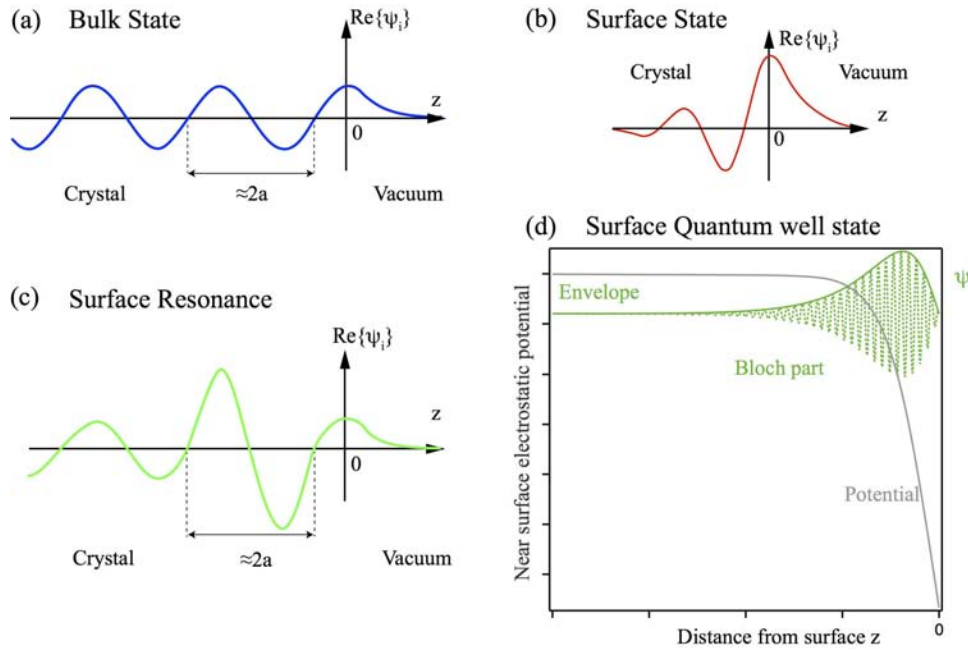


Figure 1.2: Real part of the wavefunction for a bulk state (a), surface state (b) and surface resonance (c) respectively. In all cases the wavefunction has to match an exponential decay into the vacuum. (d) Quantum well state originating on a semiconductor surface due to the downward bending of the conduction band (CB). This is caused by an electric field, and can lead to the quantisation of the CB states near the surface. The envelope wavefunction of the lowest state (solid line) has no node and the microscopic state still has Bloch-wave character (dashed line). Please note that the  $z$  scale in this figure is much larger than those in (a-c).

In order for such a state to exist it has to lie in an energy gap between bands; otherwise it will be degenerate with the bulk Bloch waves. At this point it is useful to clarify that such a state is referred to as a *surface state* (SS), and in this context can be considered an *incidental* solution to the Schrödinger equation. By this it is meant that small changes in the Hamiltonian may destroy the SS.

Nevertheless this discussion does not imply that surface localised states can not exist in the bulk projection into the surface. On the contrary such hybrid states, with an anomalous amplitude at the surface, exist and in this case they are referred to as *surface resonances*. The latter differs from a true SS as it can propagate deeper into the bulk, as a bulk Bloch wave, but the envelope of the w.f.'s real part has a maximum near the surface (see for example Ref. [16]).

Another personage that can be found at a surface is a quantum well state (QWS). These states have a totally different origin than the aforementioned ones, and appear on semiconductors when a potential at the surface is strong enough to quantise states in the conduction band (CB), see for example Refs. [17, 18, 19]. Such a state still has a two-dimensional character and is confined at the surface, but with a penetration depth into the bulk much larger than a SS. Furthermore the near-surface Bloch wave of the QWS looks similar to that of the parent bulk state it derives from, similar to a surface resonance. Additionally the quantisation reduces the permitted  $k_z$ -values in the band, thus the QWS loses its three-dimensional dispersion and becomes two-dimensional.

### 1.1.2 Spin-orbit coupling: From atoms to the crystal

In a simplified model reminiscent of A. Einstein's teaching, one can treat the spin-orbit interaction (SOI) using the tools of classical electrodynamics, but bearing in mind that the magnetic field depends on the reference system. In a system moving with velocity  $\vec{v}$ , a static electric field  $\mathbf{E}$  is seen as a magnetic one  $\mathbf{B}$  (via the Lorentz transformation<sup>2</sup>). This means that a moving electron in  $\mathbf{E}$  experiences a magnetic field that will couple to the electron's magnetic moment  $\vec{\mu}_S = g\frac{q}{2m_0}\vec{s}$  (being  $g$  the g-factor and  $\vec{s}$  the spin angular momentum). Remembering that an electron that sits on a band is a charge with a magnetic moment moving in a (periodic) electric potential (the crystal), the spin-orbit coupling will be proportional to  $\vec{\mu}_S \cdot (\vec{v} \times \vec{E})$  (Chap. 9 of Ref. [11]).

The SOI is therefore a genuinely relativistic interaction whose mathematical form comes directly from the quadratic expansion of the Dirac equation [20] and in its more common representation is:

$$\widehat{\mathcal{H}}_{\text{SO}} = \frac{\hbar}{4m_0^2c^2}\vec{\sigma} \cdot [\vec{\nabla}V \times \widehat{\mathbf{p}}]. \quad (1.4)$$

In this notation  $\vec{\sigma}$  are the Pauli matrices ( $\sigma_x, \sigma_y, \sigma_z$ ) (the basis is chosen as usual such that the quantisation axis is z),  $m_0$  and  $V$  are the free electron rest mass and the *external* potential respectively, while  $\widehat{\mathbf{p}}$  is the canonical momentum operator. In atomic and molecular physics this term<sup>3</sup> is well known to be responsible for shifting and splitting spin-degenerate energy levels into states with parallel and antiparallel spin with respect to the orbit (see for example

<sup>2</sup>Simplified here means neglecting terms in  $(v/c)^2$  or higher. Then  $\mathbf{B} = -\frac{1}{c}\vec{v} \times \mathbf{E}$  can be obtained.

<sup>3</sup>Usually in the form  $\mathbf{L} \cdot \mathbf{S}$  where these refer to the orbital and spin angular momenta, respectively. Additional approximations are involved in this treatment, see Ref. [14].

[14]). The heavier the element is, i.e. the higher the valence number  $Z$  is, the stronger this effect can be.

When studying the electronic properties of crystals, the SOI is relevant in two ways: it determines how the energy levels split before merging to form the conduction and valence bands in the crystal (influencing in this way possible gaps), but it can also affect localised states, lifting the spin degeneracy. Considering the latter case, referred to also as spin-orbit coupling (SOC), a fundamental theorem in quantum mechanics states that time-reversal symmetry always preserves the Kramer's degeneracy between each w.f. and its complex conjugate. As in crystals  $\psi^*$  is related to  $\psi$  through the inversion of the wave vector and spin, we can state that in the Brillouin zone

$$E(\mathbf{k}, \uparrow) = E(-\mathbf{k}, \downarrow) \quad \text{called time-reversal symmetry.}$$

Furthermore, most of the crystals (fcc, hcp) possess inversion symmetry (i.e. the transformation  $\mathbf{r} \rightarrow -\mathbf{r}$  leaves the crystal unchanged), that leads us to the following identity:

$$E(\mathbf{k}, \uparrow) = E(-\mathbf{k}, \uparrow) \quad \text{called inversion symmetry.}$$

This means that in the bulk the two symmetries require spin degeneracy. This is not true anymore when we introduce the surface, which breaks inversion symmetry in the direction orthogonal to it. For this reason at the surface of a solid it is possible to observe a lifted degeneracy in spin. This will be discussed in the following section.

Nevertheless what must be recognised is that the SOI causes fundamental changes to the band location and size of band-gaps where an eventual surface state can lie. It therefore plays an important role in the bulk band structure of semimetals and semiconductors, even in the presence of lattices with inversion symmetry. Furthermore, as will be clarified by an instructive example shown in Fig. 1.3, it can be responsible for a drastic inversion of the symmetry and parity that characterises the valence and conduction bands [21]. This figure presents the result obtained by Zhang *et al.*, where they have calculated the atomic orbitals' behaviour for the alloy  $\text{Bi}_2\text{Se}_3$  once the chemical bonding and then the SOI are considered.

Providing a quantitative prediction of the SOI's effect on the band calculation is difficult, nevertheless an instructive exercise on its qualitative role is presented in Ref. [22], where a TB method is applied starting from p-states. A deeper discussion on the inclusion of the SOC in TB calculations can be found in Ref. [23].

## Spin-orbit coupling and surface states: *the Rashba effect*

It has been mentioned that one of the effects of creating a surface is a potential gradient, that is equivalent to an electric field, in the surface orthogonal direction. If we assume the presence of a surface-localised 2D electron-gas (i.e. a toy model for a surface state described by the parabolic dispersion relation:  $\epsilon(\vec{k}) = \hbar^2/2m^*|\vec{k}|^2$ ) what can be observed is essentially a splitting of the state in a manner reminiscent of the Zeeman effect, leading to a difference between states with spin right and spin left [24]. This is depicted in Fig. 1.4(a). This effect is normally referred to as the *Rashba effect* (or splitting) and is thoroughly discussed by Rashba–Bychkov in the original papers [25, 26, 27] and in clarified form in more modern literature [24, 28, 29].

In the context of this dissertation it is enough to mention that this effect can be described

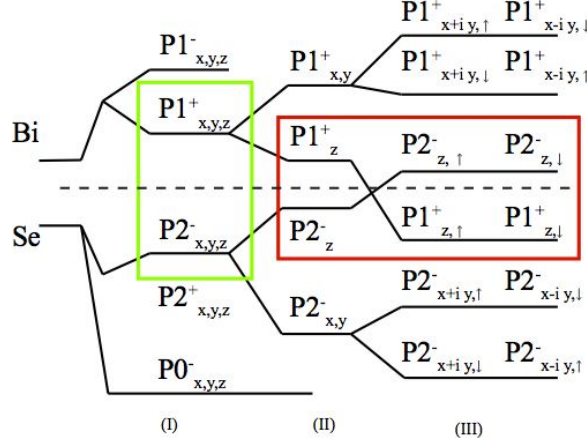


Figure 1.3: From Ref. [21]. Diagram of the calculated evolution from the atomic  $p_{x,y,z}$  orbitals of atomic Bi and Se into the conduction and valence bands of  $\text{Bi}_2\text{Se}_3$  at the  $\Gamma$  point. The three different stages (I), (II) and (III) represent the effect of turning on chemical bonding, crystal-field splitting and SOC, respectively. With  $+$  and  $-$  are indicated the parity eigenvalues of the considered state.

formally by the following Hamiltonians:

$$\mathcal{H} = \mathcal{H}_0 + \mathcal{H}_{RB} \quad \text{where} \quad \mathcal{H}_0 = \mathbb{I} \left( \epsilon_0 - \frac{\hbar^2}{2m^*} \nabla^2 \right) \quad (1.5)$$

$$\text{and} \quad \mathcal{H}_{RM} = -\alpha_{RB} \left( i\sigma_y \frac{\partial}{\partial x} - i\sigma_x \frac{\partial}{\partial y} \right)$$

With this notation the coupling constant  $\alpha_{RB}$  describes the strength of the Rashba effect and can be related to the atomic number together with a structural term describing the potential gradient at the surface (in the direction  $\hat{z}$  for positive  $\alpha_{RB}$  and vice versa). Two Rashba states are provided by the eigenvalues of  $\mathcal{H}$  and can be written as

$$E_{\pm}(\vec{k}) = E_{\bar{\Gamma}} + \frac{\hbar^2}{2m^*} |\vec{k}|^2 \pm \alpha_{RB} |\vec{k}| \quad (1.6)$$

where  $E_{\bar{\Gamma}}$  is the energy offset depicting the the state at  $\vec{k} = (0, 0)$  i.e.  $\bar{\Gamma}$ . This model is also able to predict the chirality of the spin (ultimately the direction of rotation of the spin in the  $\vec{k}$  plane) if one looks at the expectation values of the eigenspinors corresponding to Eq. 1.5:

$$|\mathbf{k}, \pm\rangle = \frac{1}{\sqrt{2}} (e^{i(\varphi \pm \pi/2)}, 1) \quad \text{where} \quad \varphi = \arctan\left(\frac{k_y}{k_x}\right)$$

which are

$$\mathbf{S}_{\pm}(\mathbf{k}) = \frac{\hbar}{2} \begin{pmatrix} \mp \sin\varphi \\ \pm \cos\varphi \\ 0 \end{pmatrix}$$

What turns out from these is that for a simple 2DEG the spin is always perpendicular to the momentum without components in  $z$ . Furthermore for  $\alpha_{RB} > 0$  and above the crossing

point of the two parabolic states, the spin of the inner branch will rotate clockwise while the spin of the outer one rotates counter-clockwise, when observed from the higher energy direction (see Fig. 1.4(a)). This effect basically leads to the phase difference needed in the spin field effect transistor proposed by Datta and Das [30].

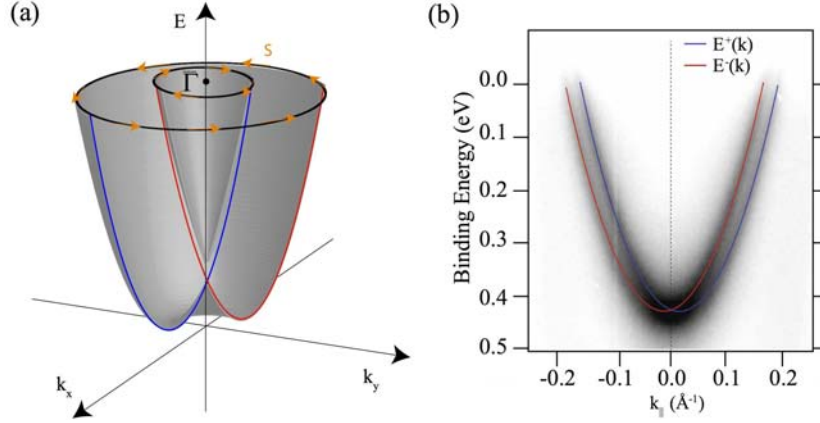


Figure 1.4: (a) Rashba-split two-dimensional electron gas from Ref. [24] with spin direction indicated. (b) ARPES measurement of the prototypical system Au(111) showing the energy dispersion  $E_{\pm}(k_x, 0)$  relation of the corresponding surface state. The spectra have been measured with  $h\nu=20$  eV at room temperature. Dark areas represent high photoemission intensity. Red and blue lines are guides to the eye highlighting the two Rashba-split parabolic states.

The canonical example of a system where such an effect is observed is the surface state of Au(111) shown in Fig. 1.4(b), where a quasi-free electron state shows a lifted degeneracy due to the presence of the potential gradient at the surface that resembles the described model [31, 32]. A similar effect in a different system can also be found in [33].

## 1.2 A special family of semiconductors: *Topological insulators*

A topological insulator (TI) is a material with an insulating (or more generally semiconducting) bulk, characterised by an electronic excitation gap generated by the spin-orbit interaction, while, due to time-reversal symmetries, the presence of gapless electronic states makes the edges conductive [4, 5, 6, 7, 8, 9]. The electronic state making the surface conductive is therefore referred to as a topological state (TS).

Even though similarities can be drawn between a surface state (as defined in Chap. 1.1.1) and a TS, they are different in origin. While the existence of a surface state is somehow coincidental (see Chap. 1.1.1) the origin of a TS lies in the properties of the bulk and it is mathematically predicted by topological considerations. Furthermore, for a surface state the presence of a spin-polarised Fermi surface is not necessarily required, while a TS is strongly spin-polarised. The complexity in understanding thoroughly such a peculiar edge effect is neatly hidden in the adjective *topological*. Although this field has seen an explosion of interest

in recent years, the original idea can be traced back to the 70s and to Sir. Pendry and Gurman in their seminal paper [34] that already contains the basic concepts and ingredients.

Topology is a branch of mathematics studying the properties which are conserved under continuous and smooth deformations of the system. In the case of our interest the smooth deformation is a change of the Hamiltonian describing the system that might change smoothly the shape and size of the energy gap characterising the insulating state of the system, without closing it. This means that such changes will also affect the electronic w.f., and being smooth means that quantities expressed by integrals containing the w.f., called topological invariants, do not change during the transformation. Such changes consist for example of adding potentials, or varying the crystal lattice or the strength of the relevant couplings that are considered in the model.

Therefore an advanced and thorough modelling of these systems evokes a severe mathematical formalism that is outside the scope of this work. However an introduction with guidelines can be found in these three illuminating papers [4], [35] and [36].

Given the experimental cut of this thesis, the emergence of such peculiar surface phenomena will be discussed only with symmetry and parity arguments and, to do so, two instructive figures are given: Fig. 1.3 and Fig. 1.5. In the first one the origin of what is called an *inverted* band gap is described for the prototypical topological insulator  $\text{Bi}_2\text{Se}_3$ , where the SOI leads indeed to an unexpected parity inversion between the valence and conduction bands. By this it is meant that the parity eigenvalue (indicated by + or -) of such bands is now inverted. The parity operator and its eigenvalues are defined as:

$$\hat{P}f(x) = \xi f(-x) \quad \text{and its eigenvalues can be} \quad \begin{cases} \xi = +1 & \text{called } \textit{even} \\ \xi = -1 & \text{called } \textit{odd} \end{cases} \quad (1.7)$$

So let us think about merging two different insulators, one where this inversion is present and a common one (see Fig. 1.5).

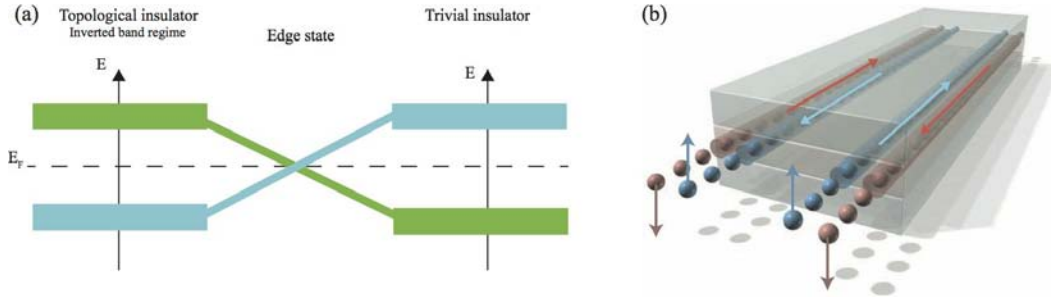


Figure 1.5: (a) Merging an insulator (or semi-conductor) with an inverted band gap (left) to a trivial one (right) can lead to edge states filling the energy gap which are the direct consequence of bulk properties such as symmetry and parity. In this figure the different colours depict the different parity of the bands considered. (b) Illustration of the spin-polarised edge currents in the HgTe quantum well, the first realisation of a quantum spin Hall insulator (from Ref. [37]) representing the realisation of a 2D topological insulator.

Roughly speaking, delocalised electron's w.f.s belonging to bands with analogous symmetry would like to merge together and to bridge the band gap, turning the junction metallic (see Fig. 1.5). This is actually how the first 2D topological insulator was discovered: the CdTe/HgTe/CdTe quantum well structure [37], also called Quantum Spin Hall Insulator.

### 1.2.1 Towards the quantum spin Hall insulator

The Hall effect (1879) appears in a conductive plate when it is placed in a magnetic field and a current ( $I$ ) flows in the longitudinal direction. The effect consists of an accumulation of charge at the edges across the plate, creating a voltage ( $V_H$ ) transverse to the current applied — this is a consequence of the Lorentz force.

The Quantum Hall effect (theory 1975 [38], experiment 1980 [39]) is a quantum-mechanical analog of the Hall effect. It is observed in a similar experiment but at low temperature and in two-dimensional conductors (or semiconductors like gallium arsenide heterostructures) under the conditions of high magnetic field and high mobility. Here it is possible to observe that the Hall resistivity  $R_H$ , defined as the ratio  $V_H/I$ , has a step-like behaviour as a function of the applied magnetic field intensity ( $B$ ). Each step appears together with a peak in the resistivity in the direction of the current flow. This phenomena is a consequence of the filling and moving of Landau levels in what can be modelled as a free 2D electron-gas where the circular cyclotron orbits are quantised. How this effect can be related to topology is described by Thouless, Kohmoto, Nightingale and den Nijs (TKNN) [40, 41]. In these papers it is shown how the Hall conductance can be written in terms of a topological invariant (specifically the Chern number) which is naturally an integer.

An analogy to the latter effect gives the name Quantum Spin Hall Insulator to peculiar 2D systems where spin-filtered electronic currents are detectable at the boundary with a normal insulator and arise from parity considerations of the bulk electronic structure. In these states opposite spins travel in opposite directions (see Fig. 1.5 (b)). The first experimental realisation of a Quantum Spin Hall Insulator was realised by the Molenkamp's group in Würzburg sandwiching a thin HgTe layer in a CdTe structure [37]. It was observed that changing the thickness of such a layer leads a non-inverted band regime to turn into an inverted one<sup>4</sup>, which is the origin of the aforementioned edge states.

The name recalls the spin Hall effect as here the role of the strong magnetic field is somehow played by the SOI itself. This means that, despite the name, the two effects have a fundamental difference: in the Quantum Hall effect the presence of the magnetic field, and hence the emergence of the Hall conductivity, breaks the time-reversal symmetry, while in the Quantum Spin Hall Insulator this is conserved. Aside from marking a deep topological difference between the two cases, the preservation of time-reversal symmetry allows the application of Kramer's theorem at  $\mathbf{k} = (0, 0, 0)$ . Furthermore the combination of time-reversal and crystal symmetry still requires the state filling the energy gap at the edge of the topological insulator to be twofold degenerate at the *time-reversal-invariant momenta* (TRIM). There are eight in three dimensions and four in two dimensions [4] and they are defined so as to satisfy the relation:

$$-\mathbf{\Lambda}_i = \mathbf{\Lambda}_i + \mathbf{G} \quad \text{where } \mathbf{G} \text{ is a reciprocal lattice vector.} \quad (1.8)$$

On the surface and away from the TRIMs, the SOI will split the degeneracy [42, 35] and here is where topology plays another fundamental role. We can summarise in fact two possible ways how two TRIMs can be connected. It is shown in Fig. 1.6 that these are topologically inequivalent. Only one (case (b) in Fig. 1.6 ) guarantees the presence of edge states even when changing the size of the gap or the position of the Fermi energy inside the bulk gap [4]. This is what happens in a topological insulator.

---

<sup>4</sup>In a manner analogous to the way bound levels in a potential well shift as a function of the size of the well.

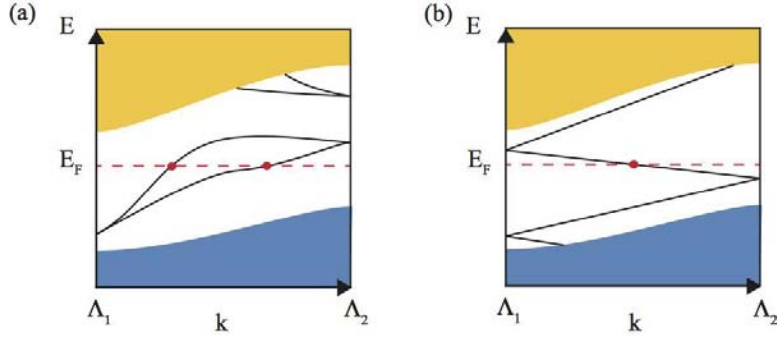


Figure 1.6: Diagrams depicting the two topologically inequivalent ways in which Kramers degenerate edge states may be connected between two TRIMs, in two or three dimensions. Coloured areas depict bulk continuum states, while lines show discrete states localised at the edge of the crystal. Case (b) occurs in topological insulators and is the only one guaranteeing that the states cross any possible Fermi energy ( $E_F$ ) inside the bulk gap. Adapted from Ref. [4].

### 1.2.2 Counting Fermi surface crossings and topology

According to the topological description [35], which of these alternatives occurs depends on the topological class of the bulk band structure. This can be classified by indices that are  $\mathbb{Z}_2$  topological invariants. In Refs. [4, 5] it is clarified how one of these, called  $\nu_0$ , determines the topological character of the gapped system between being a strong ( $\nu_0 = 1$ ) or a trivial ( $\nu_0 = 0$ ) topological insulator. This can be computed easily if the system possesses inversion symmetry as follows:

$$(-1)^{\nu_0} = \prod_{n=1}^M \delta_i \quad (1.9)$$

where the  $\delta_i$  are the parity invariants of the TRIMs  $\Lambda_i$  and can be calculated by:

$$\delta(\Lambda_i) = \prod_l \xi_{2l}(\Lambda_i) \quad (1.10)$$

where the  $\xi_{2l}(\Lambda_i) = \pm 1$  are the parity eigenvalues of the  $2l$ th occupied band at  $\Lambda_i$ , obtained from a bulk band structure calculation and  $M$  is the number of TRIMs. The factor of 2 is inherited from the Kramers degeneracy that leads the distinct bands  $2l$  and  $2l + 1$  to share the same parity eigenvalue [4] (i.e.  $\xi_{2l} = \xi_{2l+1}$ ), this allows us to consider each eigenvalue only once in the product.

The bulk parity invariants can now be used to describe fundamental properties of the surface electronic structure. To do this the indications given in Ref. [36] can be followed as here summarised. Defining the surface TRIMs  $\bar{\Lambda}_i$  such that  $\bar{\Lambda}_i = -\bar{\Lambda}_a + \vec{g}$  ( $\vec{g}$  now being a surface reciprocal lattice vector), the surface fermion parity  $\pi_i$  can be determined by projecting out the bulk parity invariants onto the corresponding surface TRIMs using the relation

$$\pi(\bar{\Lambda}_a) = (-1)^{n_b} \delta(\Lambda_i) \delta(\Lambda_j). \quad (1.11)$$

where  $n_b$  is the number of occupied bands considered in the product Eq. 1.10 (for example, 5 for the case of Bi and Sb). Examples are presented in the following sections that also will be

useful for the discussion of this work. The surface fermion parity is an interesting quantity as it can be used to predict the number of closed Fermi contours around a surface TRIM or the number of Fermi level crossings between two surface TRIMs, and this is “easy” to verify experimentally. The number of crossings has to be zero or even if the two surface TRIMs have the same parity and odd otherwise. Based on these rules, Teo, Fu and Kane [36] were able to predict the qualitative surface electronic structure of many surfaces.

### 1.2.3 Strong 3D topological insulators: Bismuth chalcogenide alloys

Theoretical [4] and experimental works agree that 3D topological insulators can be found in the BiSb and bismuth chalcogenide alloys [43], i.e. the family containing  $\text{Bi}_2\text{Te}_3$ ,  $\text{Bi}_2\text{Se}_3$  etc. Soon it will become clear why the latter can be considered the prototypical topological insulator due to the simplicity of its Fermi surface. Here in fact the topological state can be modelled, to a first approximation, with a linear dispersion, therefore giving rise to a Dirac cone shaped state around the  $\bar{\Gamma}$  point (see Fig. 1.7 and Ref. [44] for a thorough discussion). Let us take as our example the  $\text{Bi}_2\text{Se}_3$  case, whose bulk Brillouin zone (BZ), similar to a

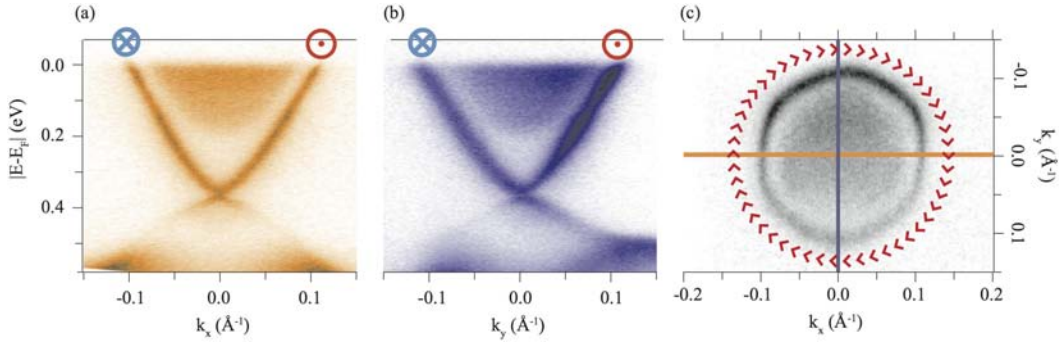


Figure 1.7: ARPES measurements on the (111) surface electronic structure of  $\text{Bi}_2\text{Se}_3$  reveal a Dirac cone shape ( $\hbar\nu=16$  eV). Dark areas indicate high photoemission intensity. Both (a) and (b) show the dispersion relations along the directions indicated by the orange (a) and blue (b) lines on the Fermi surface map around  $\bar{\Gamma}$ . (c) Red arrows indicate the chiral left handed spin texture theoretically predicted. The predicted direction of the spin is indicated also by circles in (a) and (b), each branch of the Dirac cone is predicted and measured to be occupied by a single spin [45, 46, 47].

squeezed fcc, is presented in Fig. 1.8 together with the hexagonal (111) surface Brillouin zone (SBZ) and the rhombohedral unit cell (something similar happens for  $\text{Bi}_2\text{Te}_3$ ). The topological phase appears when the alloy crystallises in this peculiar layered structure made of quintuple layers interacting with each other via weak bonding (van der Waals) [48, 49]. In the quintuple layer covalent bondings are present that stack the inner layers in the following order: Se-Bi-Se-Bi-Se. A careful observation of the unit cell will reveal that the crystal possesses inversion symmetry and it is therefore possible to apply the calculations presented above, as done in the following.

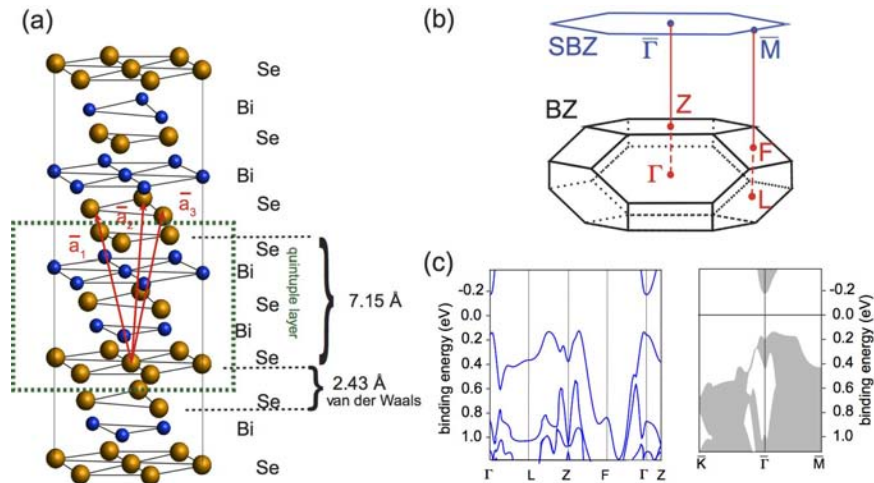


Figure 1.8: (a) Crystal structure of  $\text{Bi}_2\text{Se}_3$  and interlayer distances as determined by x-ray diffraction at room temperature (courtesy of Jianli Mi). Three primitive lattice vectors are indicated in red, while in green the quintuple layer is highlighted. (b) Scheme of the bulk and surface Brillouin zones (BZ and SBZ, respectively) with bulk TRIMs and their projection to surface TRIMs (adapted from Ref. [50]). In (c) the bulk band structure along selected high symmetry points and projection on the (111) surface are shown after [51].

### 1.2.4 A topological *resumé*

In order to summarise, here follows a list describing the hallmarks of a topological insulator.

$\nu_0$  : The case  $\nu_0 = 0$  ( $\nu_0 = 1$ ) indicates a trivial (topological) insulator that has an even (odd) number of closed Fermi contours around TRIMs in the surface Brillouin zone (SBZ).  $\nu_0$  can be inferred from the bulk band parity eigenvalues at TRIMs. Indications on how this can be done are found in Refs. [4, 5, 36] and [50]. For both the cases presented in this work,  $\text{Bi}_2\text{Se}_3$  and  $\text{Sb}$ ,  $\nu_0 = 1$ .

**Lifted Spin Degeneracy and spin-momentum locking:** Unlike a common 2D metal, where each point of the Fermi surface is occupied by two opposite spins, the surface state of a topological insulator is not spin degenerate (similar to the  $\text{Au}(111)$  surface state, each band has its own spin direction and is not doubly degenerate). This can be understood if one thinks of the 2D case, where a topological insulator is also called a *2D quantum spin Hall insulator*. Due to the SOI one-dimensional and spin-filtered electronic currents are detectable at the edges of the quantum well: opposite spins travel in opposite directions. A complete summary of the origins of these properties can be found in Ref. [35]. The measurements presented in this work have been performed in a system where it is not possible to infer the spin polarisation of the probed states. For this reason when the spin polarisation will be presented, this information is taken from the theoretical prediction or other spin-resolved ARPES data.

**Time-reversal symmetry and stability:**  $E(\mathbf{k}, \uparrow) = E(-\mathbf{k}, \downarrow)$ , i.e. the time-reversal sym-

metry, protects the topological state from backscattering<sup>5</sup>. In the presence of a defect, a helical surface Dirac fermion can backscatter, i.e. invert its momentum, only if the defect induces a spin flip. It follows that, in the absence of magnetic impurities, the topological state is in theory protected (i.e. robust) from direct backscattering from disorder impurities. Another related point is the TS's very existence, which is protected by bulk properties as explained in the previous section.

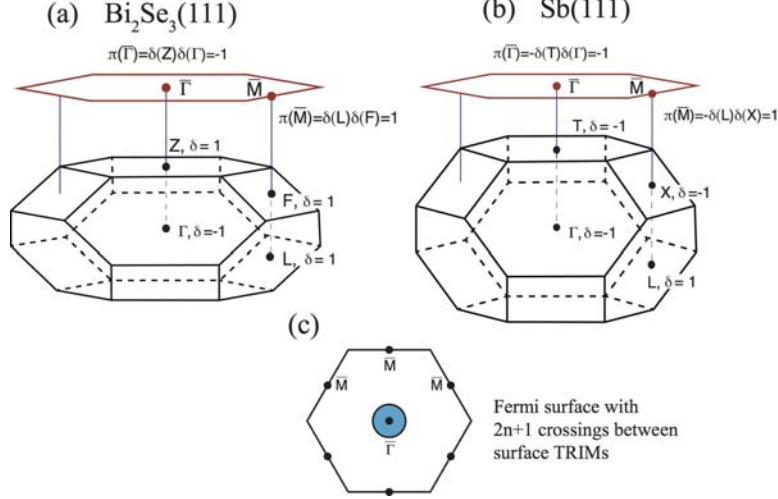


Figure 1.9: Bulk Brillouin zone of (a)  $\text{Bi}_2\text{Se}_3$  and (b)  $\text{Sb}$  with projections onto the (111) surface Brillouin zone (not to scale). The surface fermion parity at the surface is denoted and has been obtained from the parity invariants at the bulk TRIMs using Eq. 1.11. (c) The qualitative prediction of the Fermi surface according to the theory of Teo, Fu and Kane [4, 36] is the same for both the systems.

After this brief introduction highlighting the hallmarks and the theory, it is useful to apply it to both the studied cases of  $\text{Sb}(110)$  and  $\text{Bi}_2\text{Se}_3(111)$  but also to  $\text{Sb}(111)$  and  $\text{Bi}_2\text{Se}_3(110)$ , in order to qualitatively predict their Fermi surfaces and compare them.

Fig. 1.9(a) depicts the (111) case for both  $\text{Bi}_2\text{Se}_3$  and  $\text{Sb}$ . If we consider the former,  $\text{Bi}$  possesses 5 valence electrons while  $\text{Se}$  has 6, that brings us to 28 electrons per unit cell in the  $\text{Bi}_2\text{Se}_3$  crystal, so 14 spin-degenerate bands are present in this case. The parity eigenvalue  $\delta$  at  $\Gamma$  will then be the product of the 14 parity eigenvalues related to each band, and similarly for the other inequivalent bulk TRIMs:  $Z$ ,  $L$  and  $F$  (for a total of 8 bulk TRIMs, see Fig. 1.8). What calculations show is that due to the SOI  $\delta(\Gamma) = -1$  while for the other bulk TRIMs  $\delta = +1$  [50]. This inversion is inherited by the (111) surface and leads to an inversion of the parity eigenvalues between  $\bar{\Gamma}$  and  $\bar{M}$  (two surface TRIMs). These eigenvalues theoretically predict the presence of an odd number of non-degenerate Fermi contours around  $\bar{\Gamma}$  and this is what actually can be observed in ARPES measurements (see Fig. 1.7). Furthermore the

<sup>5</sup>Actually the two hallmark properties of a TI are the spin-momentum locking and  $\pi$  Berry's phase [35]. The property here described is one of the direct consequences of the latter.

dispersion relation is approximately linear around  $\bar{\Gamma}$ , allowing the 2D band structure to be idealised as a Dirac cone.

For the case of Sb(111) (Fig. 1.9(b)) the same qualitative prediction, shown in Fig. 1.9(c) can be obtained:  $\pi$  for  $\bar{\Gamma}$  has to be calculated from the parity invariants of the bulk  $\Gamma$  and T points, which are both -1 and hence  $\pi(\bar{\Gamma}) = -1$  [53, 54]. In this case the number of filled bands to be considered ( $n_b$ ) is 5, as for Bi, giving a negative sign before the product of the parity eigenvalues in Eq. 1.11. The only difference in bulk parity invariants between pure Bi and Sb, two apparently similar systems, is at the  $L$  point where  $\delta(L) = -1$  and 1 for Bi and Sb, respectively. The case of Sb(111) is also experimentally consistent with the prediction of Fig. 1.9(c) and this is discussed in Refs. [4, 45], but the Fermi surface is more complex than in the  $\text{Bi}_2\text{Se}_3$  case. The presence of projected bulk bands and a hole pocket between  $\bar{\Gamma}$  and  $\bar{M}$  on Sb(111) provides a verification of the method in a less trivial environment.

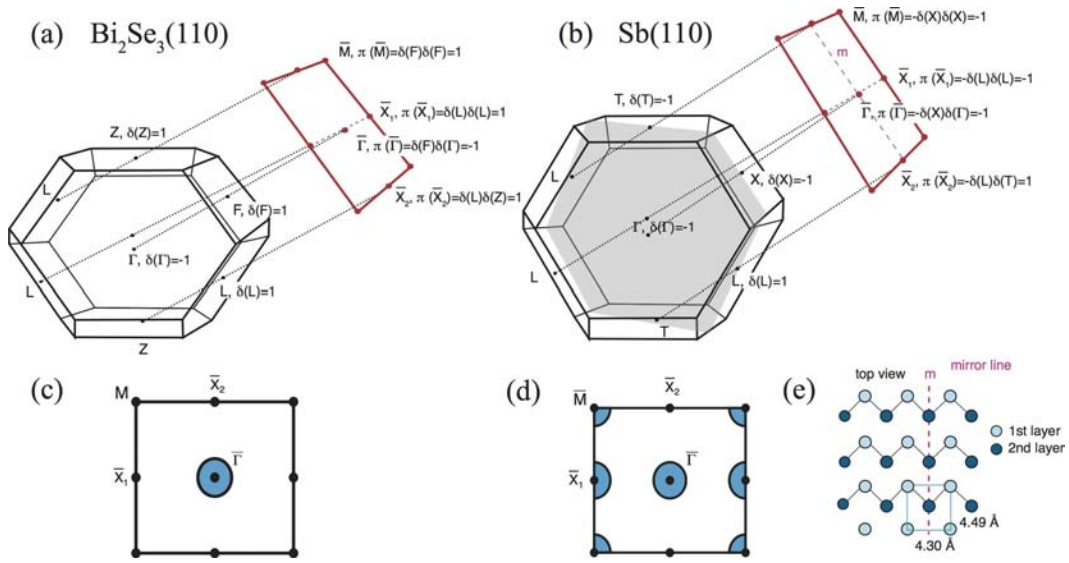


Figure 1.10: Bulk Brillouin zone of (a)  $\text{Bi}_2\text{Se}_3$  and (b) Sb with projections onto the (110) surface Brillouin zone (not to scale). For the 8 bulk time-reversal-invariant momenta (TRIMs)  $\Lambda_i$ , the parity invariants  $\delta(\Lambda_i)$  are given. These are projected onto the 4 surface TRIMs  $\bar{\Lambda}_a$ , resulting in the surface fermion parity  $\pi(\bar{\Lambda}_a) = (-1)^{n_b} \delta(\Lambda_i) \delta(\Lambda_j)$ . The resulting values of  $\pi(\bar{\Lambda}_a)$  are denoted at the surface TRIMs. The grey plane is a bulk mirror plane which projects onto a surface mirror line shown also in (e) where the truncated-bulk geometric structure of Sb(110) is presented. (c) and (d) are the qualitative predictions [4, 36] of the Fermi surface for  $\text{Bi}_2\text{Se}_3(110)$  and  $\text{Sb}(110)$  respectively.

The difference between these two systems becomes more evident if one investigates open surfaces like the (110), here described in Fig. 1.10. From pure Bi to Sb the topology changes the (110) surface fermion parity at  $\bar{X}_2$  from -1 to 1, respectively, as shown in Fig. 1.10(b) [36, 4]. In the case of  $\text{Bi}_2\text{Se}_3(110)$  the prediction is still to have a single (or odd) contour around  $\bar{\Gamma}$  while in Sb the situation is again more convoluted. In  $\text{Sb}(110)$  one should expect an even number of crossings between  $\bar{\Gamma}$  and  $\bar{X}_1$  or  $\bar{M}$  while odd between  $\bar{\Gamma}$  and  $\bar{X}_2$ . Neither of the two (110) surfaces had been experimentally investigated at the beginning of this work.

### 1.3 Introduction to photoemission

The fundamental concept necessary to understand photoemission is the photoelectric effect. Its quantum formulation was described by A. Einstein in 1905 [55] and is sketched here in Fig. 1.11. Here a photon of energy  $h\nu$  impinges on the sample; the energy  $h\nu$  is sufficient to free an electron from the level where it is bound and extract it out of the surface to the vacuum, where a spectrometer will measure its kinetic energy ( $E_{kin}$ ) and eventually the direction along which it has been emitted (represented by two angles with respect to normal emission,  $\theta$  and  $\phi$ , which map the hemisphere contained in the semi-space over the surface of the sample). The kinetic energy will be given by the energetic balance  $E_{kin} = h\nu - E_b - W_f$ , where  $E_b$  is the binding energy of the electron and  $W_f$  the work function.

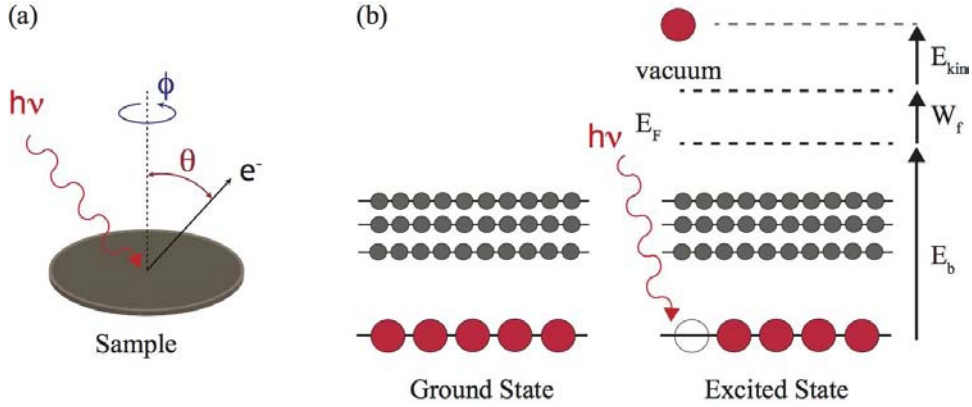


Figure 1.11: From left to right: (a) Angle-resolved photoemission spectroscopy scheme. (b) Scheme of the photoelectric process from a core level.

To understand what is actually measured in terms of intensity, line-shape etc., and what can be obtained via photoemission it is necessary to introduce a model for the photoemission process that goes beyond the simple 3-step model introduced at the beginning of the history of photoemission spectroscopy<sup>6</sup>. This can be seen using only first-order perturbation theory by writing the transition probability from the initial to the final state of the electron, using *Fermi's golden rule*:

$$P_{i,f} = \hbar^{-1} \langle M_{i,f} \rangle \delta(E_f - E_i - \hbar\nu). \quad (1.12)$$

This immediately clarifies the reason why a more advanced model is needed as we can see that most of the physics has been “hidden” in the interaction matrix element  $M_{i,f}$ . Still using this approximation and writing the single particle w.f. for the final state as  $\psi_f = \sum_n c_f(t) \phi_n e^{-i \frac{E_n}{\hbar} t}$  (where  $\mathcal{H}_0 \phi_n = E_n \phi_n$  are the non-interacting solutions) it is already possible to obtain an expression for the measured line-shape. This is related to the modulus squared of the projection of the final state onto the initial one ( $\psi_i$ ) and its time

<sup>6</sup>The 3-step model is defined as follows: an electron in its initial state is promoted to an excited state by the incident photon, then the excited electron travels towards the sample surface and finally the electron penetrates the surface's potential barrier and reaches its final free-electron state in vacuum.

dependence can be written without loss of generality as  $c_f(t) \sim e^{-\frac{t}{2\tau}}$ . Following the guidelines of Eq. 1.13 the well known Lorentzian line shape can be obtained<sup>7</sup>. With  $\tau$  we introduce a concept that will become important later that is the *life-time* of the excited state, that expresses how much time elapses before the photo-hole is refilled.

$$\begin{aligned} \dot{c}_f(t) &= -\frac{e}{m}A_0(\nu) \langle \tilde{M}_{i,f} \rangle e^{-i(\nu_{f,i}-\nu)t} c_f(t) \\ c_f(t) &= -\frac{e}{m}A_0(\nu) \langle \tilde{M}_{i,f} \rangle \int_0^t e^{-i(\nu_{f,i}-\nu)t' - \frac{t'}{2\tau}} dt' \\ |c_f(t)|^2 &\sim \frac{\left(\frac{\Gamma}{2\hbar}\right)^2}{(\nu - \nu_{f,i})^2 + \left(\frac{\Gamma}{2\hbar}\right)^2} \quad \text{where} \quad \Gamma := \frac{\hbar}{\tau} \end{aligned} \quad (1.13)$$

The two main photoemission techniques that have been used in this project are X-ray Photoemission Spectroscopy (XPS) and Angle Resolved Photoemission Spectroscopy (ARPES). Even though in principle the two techniques are similar, when referring to XPS it is meant that  $100 \lesssim h\nu \lesssim 2000$  eV. In ARPES the photon energy used can be between 4 and 130 eV.

### 1.3.1 ARPES: The spectral function $\mathcal{A}(\omega, \mathbf{k})$

One should have clear in mind that the entire system takes part in the photoemission process, not only the photoelectron, but all the other particles have to relax due to the photo-excitation. This brings us directly to the more advanced 1-step model, where the initial (final) state can be easily represented as  $\psi_i = \phi_{i,s}\varepsilon_{i,r}$  ( $\psi_f = \phi_{f,s}\varepsilon_{f,r}$ ). Here  $\phi_{i,s}$  is the original single particle w.f. while  $\varepsilon_{i,r}$  represents all the remaining particles that constitute the system. The fact that the electrons in the system interact with each other and with a plethora of other particle-like objects (such as lattice vibrations, that can be considered as particles called phonons, or plasmons etc...) makes the picture extremely complicated and needs a new treatment that exploits the *many body* theory, here very briefly introduced. This method, instead of considering the system to be composed of  $N$  interacting particles, depicts it as  $M$  non-interacting *quasiparticles*. These in our case are namely the electrons somehow “dressed” with all their interactions [56]. Using the notation already introduced for the 1-step model it becomes clear that the transition matrix  $M_{i,f}$  depends on two components, one related to the single particle and its interaction with the field<sup>8</sup>  $\langle \phi_{f,s} | \vec{A} \cdot \nabla | \phi_{i,s} \rangle$ , and one that describes the relaxation of the other particles:  $\langle \varepsilon_{f,r} | \varepsilon_{i,r} \rangle$ .

This brings us directly to the core of the problem and to the definition of the spectral function  $\mathcal{A}(\omega, \mathbf{k})$ .

In an ARPES measurement we are typically interested in the conduction properties of the surface. For this reason the energy range that is probed is the one near the Fermi edge

<sup>7</sup> $\nu$  indicates the photon frequency while  $h\nu_{f,i}$  the energy difference between the final and initial state.  $A_0(\nu)$  is the amplitude of the vector potential related to the exciting electromagnetic field at the frequency  $\nu$ .  $\langle \tilde{M}_{i,f} \rangle$  has the same meaning as the previous matrix element, where the intensity of the field has been factorized out.

<sup>8</sup>Where the interaction Hamiltonian, after other simplifications like the dipole approximation, can be represented by:  $\mathcal{H}_{int}(t) = \frac{1}{2m}(\vec{p} - q\vec{A}(t))^2 + q\varphi(t)$ , where  $\vec{A}$  is the vector potential. Choosing the Coulomb gauge the Hamiltonian can be written as  $\mathcal{H} = -(-e)\vec{A} \cdot \vec{p}$ .

and the intensity at the detector can be written<sup>9</sup> as:

$$I(\omega, \mathbf{k}, h\nu) \approx \sum_{f,i} |\langle \phi_f | \mathcal{H}_{\text{int}} | \phi_i \rangle|^2 \mathcal{A}(\omega, \mathbf{k}, T) \quad (1.14)$$

$$\mathcal{A}(\omega, \mathbf{k}) = \sum_f |\langle \varepsilon_{f,r} | \varepsilon_{i,r} \rangle|^2 \delta(\epsilon_{\text{kin}} + E(M+1) - E(M) - \hbar\omega) \quad (1.15)$$

where  $\mathcal{A}$  is the spectral function of the photo-hole and  $E(M+1)$  and  $E(M)$  indicate the energy of the system after and before the creation of the photo-hole<sup>10</sup>, respectively.

At this stage two main ingredients are needed in order to obtain an experimentally useful equation for  $\mathcal{A}$ : the quantization of the electromagnetic (e.m.) field and the definition of the *self energy*  $\Sigma$ . The first one can be easily introduced if one considers the field as a system of particles (photons) where during the process a photon is created or annihilated.

The second concept can be introduced in an intuitive way if one considers that, roughly speaking, all the many-body interactions will not leave the non-interacting state unperturbed for very long, they will change not only its energy, but they will affect its life-time too. A simple way to introduce this change in life-time is to include it into the energy term, allowing the energy to be complex. In this way its imaginary term will naturally take care of the life-time change

$$\Sigma = \Sigma' + i\Sigma''.$$

Mixing these two ingredients with care and patience using the mathematical tool of Green's functions allows us to obtain the spectral function in its commonly used form

$$\mathcal{A} = \frac{\pi^{-1} |\Sigma''(\mathbf{k}, E; T)|}{(E - \epsilon(\mathbf{k}) + \Sigma'(\mathbf{k}, E; T))^2 - \Sigma''(\mathbf{k}, E; T)^2}. \quad (1.16)$$

With this notation  $\epsilon(\mathbf{k})$  is the dispersion relation for the probed state that is called the *bare-band* dispersion, and in general  $\Sigma$ , which depends on momentum, energy and temperature ( $T$ ), contains all the many-body interactions.

In an ARPES experiment what is measured is not only the intensity as a function of kinetic energy, but also as a function of the photoemission angle. This exploits another very general physical phenomenon concerning the momentum of the photoelectron and this clarifies the reason why ARPES is such a powerful technique for probing surface states.

Due to the symmetry breaking of the surface, not only is  $k_{\perp}$  not conserved<sup>11</sup> in the photoemission process, but it is not even a good quantum number any more. In the case of our measurements, where the momentum of the photon is negligible, the quantity that is

---

<sup>9</sup>Here we are not considering the transmission function of the analyser which describes the sensitivity at the detector as a function of the measurement parameters. This will influence the intensity at the detector but not the line-shape. The finite resolution in energy of the spectrometer and the non-monochromaticity of the photon source are also neglected. These can easily be considered later, leading to a Gaussian broadening to be convolved with the spectral function.

<sup>10</sup>One should be careful as the w.f.s  $\varepsilon$  are not necessarily eigenfunctions of the system.

<sup>11</sup>This stems from the electron's energy change due to the transition from the lattice potential to the image potential, i.e. the potential generated by the escape of the charge from the solid. Or, in other words, it relates to the presence of an inner potential in the solid that sets the energy zero differently.

conserved is  $k_{\parallel}$  and the following conservation law can be written:

$$\mathbf{k}_{\parallel,i} = \mathbf{k}_{\parallel,f} = \sin(\theta) \sqrt{\frac{2mE_{kin}}{\hbar^2}} \quad (1.17)$$

Here  $\mathbf{k}_{\parallel,i}$  and  $\mathbf{k}_{\parallel,f}$  are the components of the electron's momentum parallel to the surface before and after the photoemission process. This equation is the basis of the ARPES technique as the measured quantities are  $E_{kin}$  and the angles  $\theta$  and  $\Phi$  of the photo-emitted electron (see Fig. 1.11), which is a free electron in vacuum (so  $E_{kin} = \frac{\hbar \mathbf{k}^2}{2m}$ ).

In addition, what should be remembered is that to a first approximation the measured electron is a Bloch electron, so the momentum conservation law is correct plus or minus a surface reciprocal lattice vector (i.e.  $\mathbf{k}_{\parallel,f} = \mathbf{G} + \mathbf{k}_{\parallel,i}$ ).

### Electron-phonon coupling

A complete treatment of this coupling is available in the following text books [56, 57] and the part relevant in this work is also presented in Ref. [58]. This section will recall the equations useful to extract from the photoemission data the strength of the electron-phonon coupling, namely  $\lambda$ : the mass enhancement parameter.

It has been mentioned that the self-energy contains all the contributions from the many-body interactions, but being able to measure the full-width-half-maximum (FWHM) of  $\mathcal{A}(\omega, \mathbf{k})$  (see Eq. 1.16) is not enough if one would like to know the strength of a particular interaction. What is needed is a model for the behaviour of that interaction. For these, many approximations can be considered as each contribution has its particular signature and behaviour: e.g. the electron scattering due to defects can be considered as a constant contribution to  $\Sigma$ , while the electron-electron interaction goes as  $\propto E^2$  [59]. What is done in this work consists of considering only the dominant contribution and using the lowest order of the possible Feynman<sup>12</sup> diagrams in order to find a useful expression for it. Concerning the electron-phonon coupling (EPC) the lowest order Feynman diagrams are shown in Fig. 1.12. What turns out

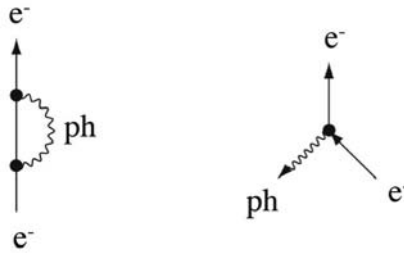


Figure 1.12: Lowest order of the Feynman diagrams for the EPC. On the left an excited electron decays emitting a phonon that is immediately re-absorbed. On the right the fundamental electron-phonon interaction is shown where an electron decays emitting a phonon. From Ref. [56].

<sup>12</sup>The power of Feynman diagrams is to represent in a pictorial way integrals that describe the interaction, and so the probability: namely the propagator of a single particle (or quasi-particle).

from these is that  $\Sigma''$  can be written as

$$|\Sigma''(\omega, T)| = \pi \hbar \int_0^{\omega_{max}} d\omega' \alpha^2 F(\omega') [1 - f_F(\omega - \omega') + 2f_B(\omega') + f_F(\omega + \omega')] . \quad (1.18)$$

This presents  $\Sigma''$  in terms of the Fermi-Dirac (for electrons) and Bose-Einstein (for phonons) distributions ( $f_F$  and  $f_B$  respectively), the maximum phonon frequency  $\omega_{max}$ , and the so-called Eliashberg function<sup>13</sup>  $\alpha^2 F(\omega)$ .

The Eliashberg function can be seen as the product of a matrix element  $\alpha^2$  (that can be naively interpreted as a coupling force between electron and vibrational modes) with the phonon density of states  $F(\omega)$ , where  $\omega$  is the energy variable [57]. Therefore this integral depicts the phonon-induced scattering between the initial electronic state at the Fermi surface into all the available final states, in a range of energy  $\hbar\omega$  reasonably near to the Fermi level. Due to the experimental focus of this work it is just necessary to know that a few approximations, including the use of the Einstein model for the phonon dispersion relation<sup>14</sup>, lead us to:  $\alpha^2 F_E(\omega) = \frac{\lambda\omega_E}{2} \cdot \delta(\omega - \omega_E)$ . The quantity we are interested in is  $\lambda$ , as it represents the EPC strength. This can also be expressed in terms of the measurable quantities  $\Sigma''$  or  $\Sigma'$  as follows:

$$\lambda = \frac{2\Delta\Sigma''}{\hbar\omega_E\pi} \quad \lambda = - \left. \frac{\partial\Sigma'(E)}{\partial E} \right|_{E_F} \quad (1.19)$$

Where the term  $\Delta\Sigma''$  is the step height of the imaginary part of the self energy at an energy  $E = \hbar\omega_E$ . This means that in order to obtain  $\lambda$  from a spectra, one should be able either to resolve deviations of the peak position of the spectral function from the bare-band dispersion, generally causing an increase of the effective mass near the Fermi level, or the width of the photoemission peak.

A measurement that gives straightforward access to  $\lambda$  is a temperature-dependent ARPES measurement. This consists of acquiring different spectra in the same energy/momentum range but at different sample temperatures  $T$ . Quantitative analysis of the spectra can be performed in order to obtain the Lorentzian FWHM of Eq. 1.16 and the group velocity ( $v$ ) in the region of interest for each  $T$  (this approach is used for example in Ref. [33]). If instead of using an Einstein model for the phonon modes we apply a full Debye model, it is possible to obtain

$$\alpha^2 F = \begin{cases} \lambda \left(\frac{\omega}{\omega_D}\right)^2 & , \omega < \omega_D \\ 0 & , \omega > \omega_D \end{cases} \quad \text{where } \omega_D \text{ is the Debye frequency.} \quad (1.20)$$

Here the Eliashberg function of the system is used directly rather than the increase of the effective mass at the Fermi energy or the step height of the FWHM occurring at a specific energy near  $E_F$  [58].

What happens is that at temperatures higher than the Debye temperature, irrespective of the details of the phonon spectrum,  $\lambda$  can be extracted from the temperature-dependent  $\Sigma''(T)$  using the following relations, also depicted in Fig. 1.13:

$$\Sigma''(T) = \frac{\text{FWHM}(T)}{v} \quad \text{and} \quad \lambda = \frac{1}{\pi k_B} \frac{d\Sigma''}{dT} \quad (1.21)$$

<sup>13</sup>The origin of this fundamental function lies in the transition matrix element that considers the initial and final state of both the electronic and phononic spectrum.

<sup>14</sup>This consists of considering all the phonons to have the same frequency  $\omega_E$ .

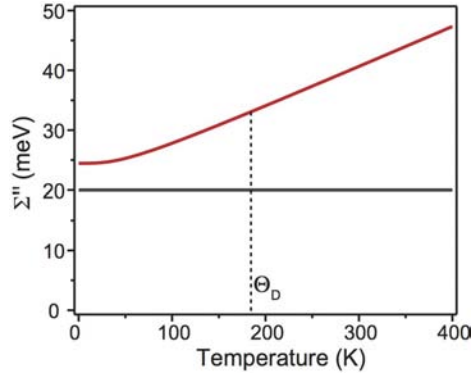


Figure 1.13: EPC-related self-energy in a full Debye model for  $\text{Bi}_2\text{Se}_3$  using  $\lambda = 0.25$  and  $\hbar\omega_D = 17$  meV corresponding to a Debye temperature  $\Theta_D = 182$  K (according to Ref. [60]). A temperature-independent contribution (black line) is added as a constant offset to account for other possible sources of scattering, e.g. defect scattering. Even somewhat under the Debye temperature,  $\Sigma''$  behaves linearly and from its slope  $\lambda$  can be determined.

### 1.3.2 X-ray spectroscopy: Core levels and line-shape

Another important photoemission technique that has been used in this work is X-ray photoemission spectroscopy (XPS). From the name it is explicit that the photon energy range used (100 eV to 10 keV) allows even deep core levels to be reached. This not only makes it an element-sensitive technique, but a great deal of information about the chemical environment of the surface (or in general of the emitter atom) and many-body effects can also be inferred. The initial state will be that of the emitting atom while the final state can be considered as a resonant state of the last occupied state [61]. Intuitively, a complete description of the line-shape and peak position must consider all the interactions that the electron will suffer during its travel to the surface and then in vacuum, plus all the final state effects. The leading contributions to be considered together with the simple Lorentzian described above can be grouped as follows:

- **Intrinsic losses:** these are two-electron processes that cause emission at lower kinetic energies than the main peak. These secondary phenomena are more evident in metals, where the electron density near the Fermi level is higher and leads to asymmetry of the peak with a characteristic tail at higher binding energy;
- **Extrinsic Losses:** these are losses caused by excitations due to the field of the photoelectron moving towards the surface, and occurring even after the photoelectron has left the surface. They can be observed either as a Gaussian broadening of the peak, or as aliasing of the highest binding energy peak, depending on experimental resolution and coupling strength;
- **Exchange-Correlation:** these are genuinely quantum effects and even though they are related to the Pauli exclusion principle and to the electrostatic interaction between

electrons, they are much more difficult to model. They lead to a change in the expectation value of the energy between two identical particles states whose w.f.s are not orthogonal, and also in the life-time of these states. This means that both the peak position and the width will be affected;

- **Experimental Resolution:** this can be considered as the convolution of the photon source's resolution together with that of the analyser, and again it leads to a Gaussian broadening.

It is evident how a semiclassical model can not reproduce all of these, but a complete treatment based on more advanced theory has been introduced by Doniach and Sünjić [62] who give their names to the most commonly adopted function to fit XPS spectra, Eq. 1.22.

$$I(E_{kin}, \alpha, \gamma, \mathbf{E}) = \frac{\Gamma(1 - \alpha) \cdot \cos\left(\frac{\pi\alpha}{2} + (1 - \alpha) \cdot \tan^{-1}\left(\frac{E - E_{kin}}{\gamma}\right)\right)}{((E - E_{kin}) + \gamma^2)^{\frac{1-\alpha}{2}}}. \quad (1.22)$$

In the following the meaning of each parameter is listed, together with the relevant contribution:

- **Lorentzian Contribution  $\gamma$ :** the full width half maximum (FWHM) of the photoemission Lorentzian peak and is related to  $\tau_f$  of Eq. 1.13.
- **Asymmetry  $\alpha$ :** also called *Anderson's asymmetry parameter*, this is related to intrinsic losses. As a rule of thumb,  $\alpha = 0$  corresponds to a perfect insulator and as the system becomes more metallic,  $\alpha \rightarrow 1$ . This parameter controls the characteristic tail of XPS spectra towards higher binding energies.
- **$\Gamma$**  is the Euler's Gamma function and reproduces the energy balance.

In order to fully reproduce the observed spectra one should then convolute Eq. 1.22 with a Gaussian whose width is made up of the experimental resolution, the phonon (vibrational) contribution [63] and the disorder (inhomogeneity) contribution.

# Chapter 2

## Experimental Set-up: ARPES at ASTRID

The results presented in this work come from photoemission experiments performed at the synchrotron radiation facility ASTRID in Aarhus. Therefore this chapter will briefly describe the photon source (i.e. synchrotron, insertion device and beamline) and the ARPES end-station where the samples have been prepared and the spectra collected. A detailed description can be found in the following paper [64] or on the web<sup>1</sup>.

### 2.1 ASTRID

The synchrotron radiation facility ASTRID in Aarhus is a second-generation light source which has been in operation since 1990 and is designed to work in two modes: electron-mode and ion-mode [65]. In the last handful of years ASTRID has primarily been dedicated to electron-mode operation and its parameters can be found in Table 2.1. A schematic of the

| Parameter                          | Value         |
|------------------------------------|---------------|
| Maximum Energy                     | 580 MeV       |
| Typical Stored Current (2009-2012) | 160-180 mA    |
| Life-time (at 150 mA)              | 100-120 hours |
| Horizontal emittance               | 0.16 mm mrad  |
| RF Frequency                       | 104.9 MHz     |
| No. of bunches                     | 14            |
| No. of bending magnets             | 4             |
| No. of insertion devices           | 1             |
| Beam size in insertion device      | 1.45-0.23 mm  |

Table 2.1: ASTRID's parameters in electron-mode.

<sup>1</sup><http://www.isa.au.dk/facilities/astrid/beamlines/sgm3/sgm3.asp>

ring is shown in Fig. 2.1 with its distinctive squared shape. It is clear from the parameters in Table 2.1 that the design maximises the brilliance at the bending magnets, where photon energies from UV to soft X-rays are available.

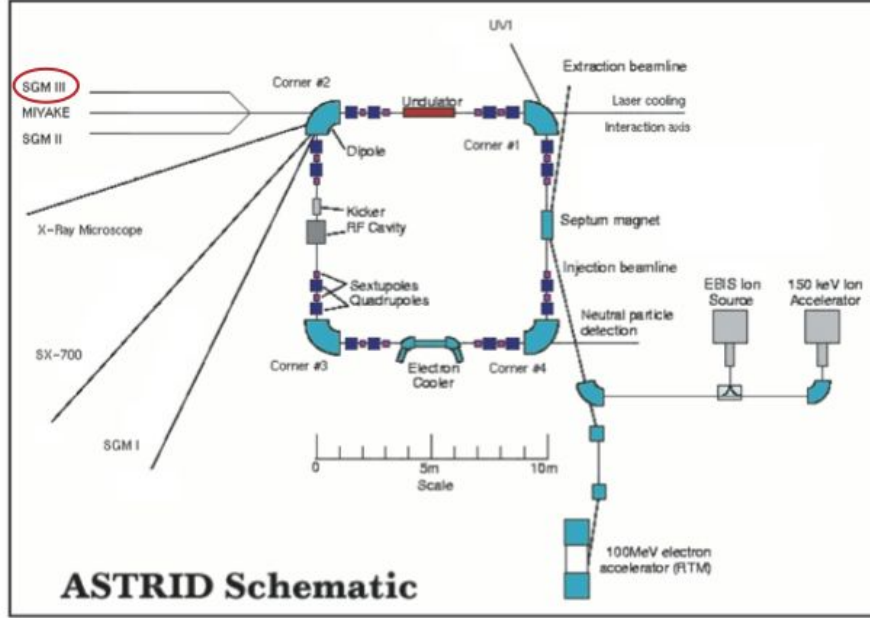


Figure 2.1: Schematic of the ASTRID ring. The red circle highlights the SGM3 beamline used for these experiments.

The light used in this project, however, comes from an undulator placed in one of the straight sections that extracts light in a position where the bunch is wider, although this still provides a high resolving power<sup>2</sup> and flux. As will become clear in the following, this is an important factor that affects angular resolution in an ARPES measurement, since it has an impact on the size of the light spot on the sample. This will be improved in the new design of the SGM3 beamline on the new third-generation low-emittance synchrotron light source ASTRID2 mentioned at the end of this thesis.

The fundamental idea of a storage ring facility for synchrotron light is that a beam made of electron bunches is injected into the storage ring where they are kept at a constant kinetic energy, by use of a radio-frequency cavity. Each time the electrons are accelerated, e.g. at each corner of the ring, light will be emitted. In an undulator the bunches are accelerated so as to follow an undulating trajectory and to a first approximation can be considered as ultra-relativistic dipoles (as  $E_{\text{kin}} = 580 \text{ MeV}$ , the Lorentz factor will be  $\gamma = 1135 \gg 1$  so  $\beta \approx 1$ ). For this reason most of the radiation will be emitted in the forward direction (i.e. towards the beamline). An undulator consists of two periodic arrays of fixed permanent magnets that are

<sup>2</sup>For resolving power is meant the ratio  $\frac{h\nu}{\Delta h\nu}$  where  $\Delta h\nu$  is the smallest difference in energy that can be distinguished at an energy  $h\nu$ .

mounted on a movable frame allowing the magnetic field intensity at the beam position to be varied. The high photon flux is achieved thanks to the careful calibration of the periodicity of the array of magnets (the undulator period), which is chosen so as to exploit coherence effects<sup>3</sup> [66, 67, 68]. In the case of SGM 3 the magnetic field is oriented vertically, giving a mostly linearly polarised light in the horizontal plane.

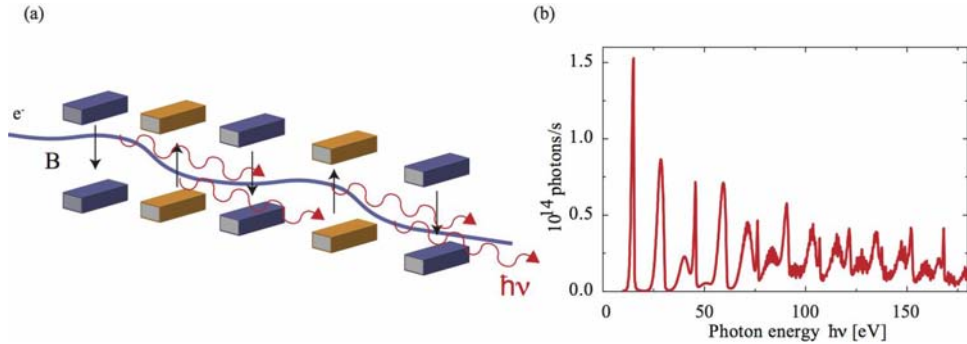


Figure 2.2: (a) Scheme of an undulator. (b) A (calculated) typical spectrum emitted by the undulator on SGM3. By changing the gap between the two arrays of magnets is possible to tune the position of the high intensity peaks towards higher or lower energy.

The resulting spectrum is an array of sharp monochromatic peaks with a continuous background (see Fig. 2.2 (b)). The power of such a machine is that the peaks' position in the photon spectrum, corresponding to certain harmonics, can be varied by changing the relative distance of the two arrays of magnets, resulting in a tuneable high flux light source. However, in order to achieve the higher degree of monochromaticity and resolving power needed for our ARPES measurements, a monochromator and a set of focusing optics are needed on the beamline.

## 2.2 The SGM3 beamline

A scheme of the beamline can be found in Fig. 2.3. Light is focused into the monochromator by two spherical mirrors: one (HFM) allows the light from the undulator to be shared with the other two beamlines, while the second (VFM) focuses it into an entrance slit (ENS) and then into the monochromator grating (G). The monochromator consists of three interchangeable spherical gratings and it allows us to reach an energy range between 14 and 130 eV, using either the first or third harmonics of the undulator light spectrum. The diffracted light is focused onto a movable exit slit (EXS), whose size defines the energy resolution. Finally a toroidal mirror (TPM) refocuses the light onto the sample in the measurement position. In order to obtain a smaller light spot on the sample's surface, and therefore higher angular resolution, a pinhole is placed in front of the sample. The one used in most of the experiments is a circular pinhole with a diameter of 300  $\mu\text{m}$ .

<sup>3</sup>The amplitude of the bunches' oscillations is small and the radiation displays interference patterns which lead to narrow energy peaks in the emission spectrum.

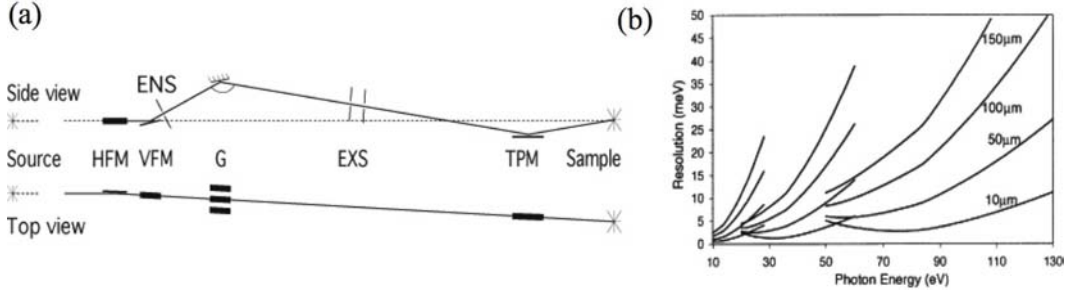


Figure 2.3: (a) Scheme of the SGM 3 beamline on ASTRID. (b) Total resolution of the beamline for four different slit settings. From Ref. [64].

## 2.3 The ARPES end-station

Fig. 2.4 summarises the layout of the ARPES end-station. It consists of 3 chambers whose names are self-explanatory: a measurement chamber (MC), a preparation chamber (PC) and a load-lock (LL). The sample, i.e. the crystal, is mounted on a rectangular sample-holder (Aarhus type) that consists of a Ta or Mo plate. A thermocouple mounted in direct contact with the back of the crystal allows the temperature to be monitored.

The purpose of the LL is to quickly load and transfer samples into vacuum without venting the entire system. The LL is also used as a spare pumping system for the rotational feedthrough of the MC manipulator or the gas-lines. The normal operating base pressure in the LL is  $2 \times 10^{-8}$  mbar, reaching eventually the low  $10^{-9}$  mbar.

The PC is equipped with a sputter-gun and a gas line for sample cleaning and preparation, and the base pressure is normally  $3 \times 10^{-10}$  mbar. Here the sample is cleaned and prepared on the cooled head of an Omniax translator MX800. The sample socket can be water- or nitrogen-cooled and allows the sample to be heated up to  $1300^\circ\text{C}$  with electron bombardment, using a tungsten filament mounted on the socket<sup>4</sup>. This chamber is also equipped with a SPECS EBE-4 electron beam evaporator allowing thin film co-deposition of up to 4 different elements. A garage is also present that allows the storage in vacuum of up to 10 samples at once.

The long stroke of the PC manipulator is exploited to transfer the sample into the MC where a second manipulator, cooled by a closed-cycle He cryostat, holds it at a temperature between 60 and 70K during the measurement. A filament is mounted that can be used to anneal the sample in order to perform temperature-dependent ARPES. The MC manipulator is able to rotate around its longitudinal (almost vertical) axis while the sample can be tilted by turning a screw visible on the side of the socket in Fig. 2.4(d). This screw can be turned manually using a wobblestick mounted on the MC that is also exploited to transfer the sample from the PC manipulator to the MC manipulator. No azimuthal rotation of the sample is available on the MC manipulator. This chamber is equipped with two hemispherical spectrometers for ARPES: a VG ARUPS 10 and a SPECS Phoibos 150. The former is mounted in vacuum on a goniometer and is therefore movable, allowing a measurement scheme where the sample is fixed and it is the analyser that moves around the sample to map the full 2D k-space. For this reason this can be used to perform polarisation-dependent Fermi surface mapping. The SPECS Phoibos 150 is a modern hemispherical spectrometer that will be

<sup>4</sup>Without electron bombardment temperatures up to  $850^\circ\text{C}$  can be reached.

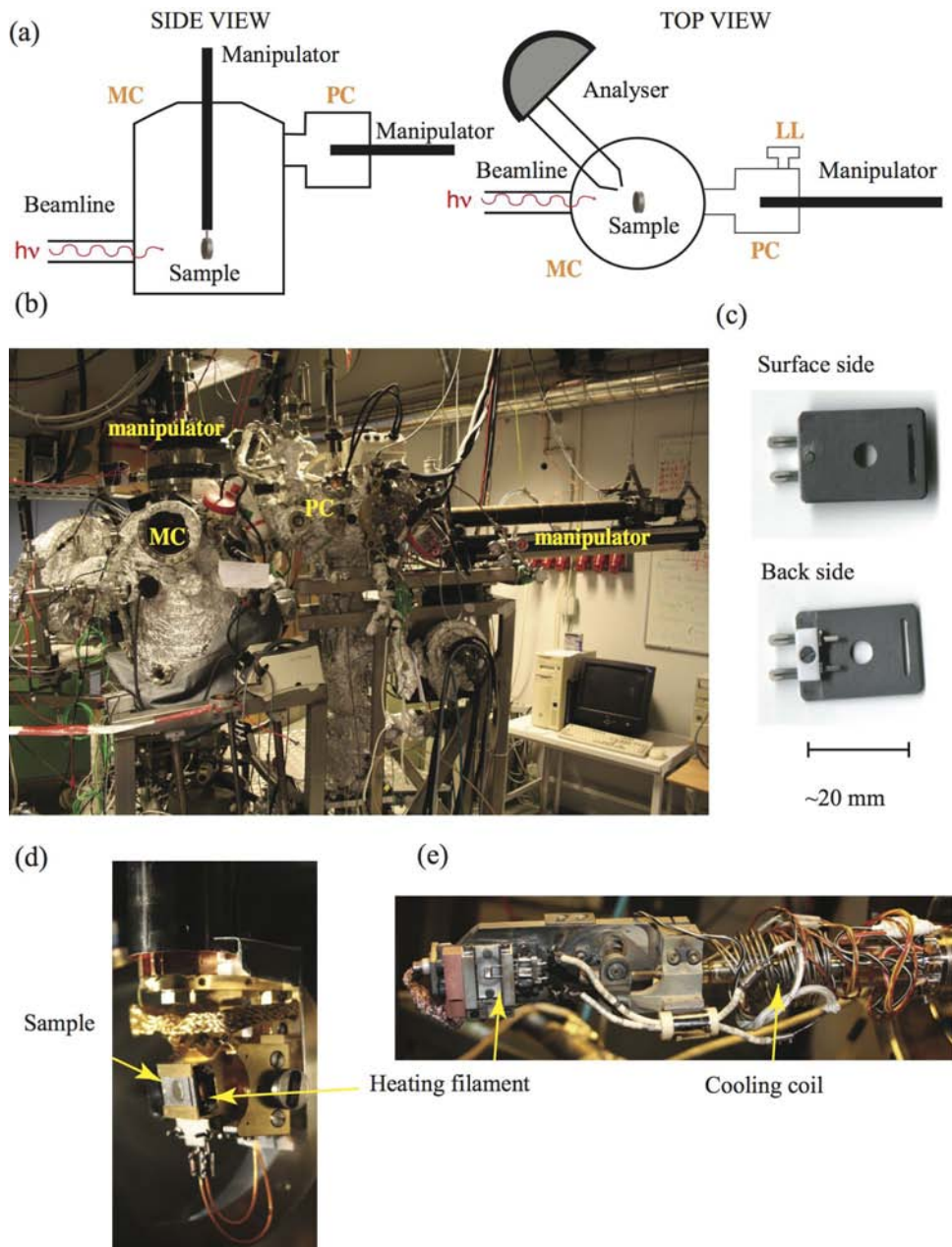


Figure 2.4: (a) Scheme of the ARPES end-station. (b) Photo from the side of the ARPES end-station where the main chamber (MC), preparation chamber (PC) are visible together with the two manipulators. (c) Picture showing the front (surface) side and the rear side of an empty sample-holder. The sample sockets of the MC (d) and PC (e) are also shown.

described in the following. This is the spectrometer that has been used for the measurements presented in this work and its lenses form an angle of  $50^\circ$  with the beamline. In the MC a low energy electron diffraction (LEED) apparatus is also mounted and is commonly used to check surface quality and orientation (see Ref. [69]).

### 2.3.1 Mapping the 2D and 3D $k$ -space with the SPECS Phoibos 150 analyser

The particular properties of the analyser not only influence the width of the measured states<sup>5</sup>, but can also induce a deformation of the spectra acquired due to the properties of the lenses that focus the photoelectron beam onto the detector. These aberrations depend on the particular spectrometer in use and on the geometry of the measurements, and can be corrected online by the hardware or offline by software. In order to describe these aberrations a short description of the instrument used in this context is necessary.

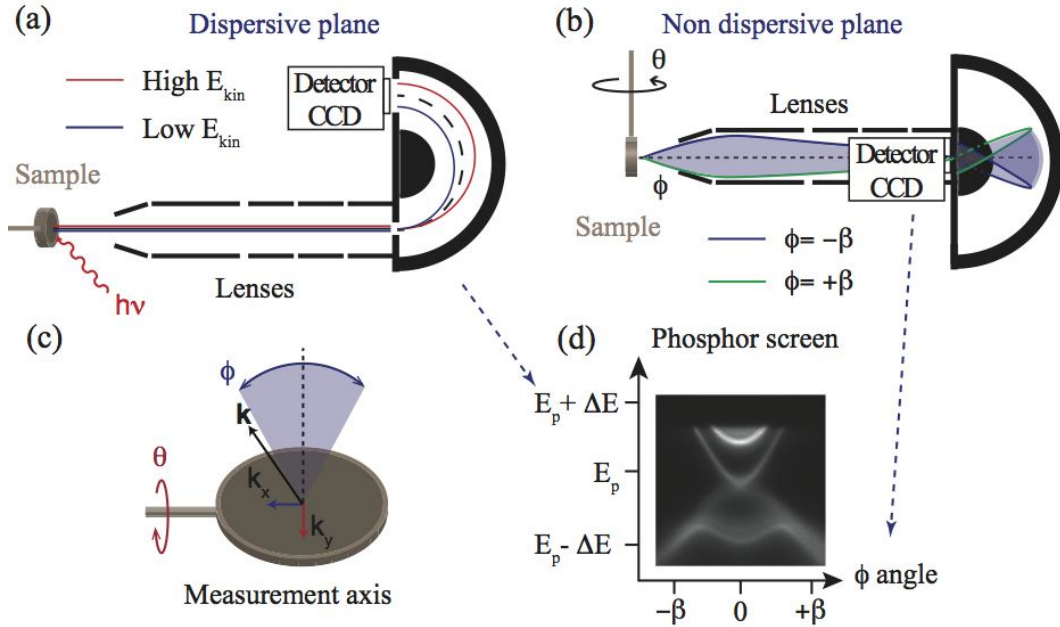


Figure 2.5: Scheme depicting the hemispherical analyser and the geometry of the ARPES experiment. (a) Cross section and definition of the dispersive plane of the analyser with the orbits of the higher (lower) kinetic energy electrons in red (blue). (b) Cross section of the non-dispersive planes of the analyser with the orbits of the electrons emitted at an angle  $+\beta$  ( $-\beta$ ) in green (blue). (c) Scheme presenting the  $\theta$  and  $\phi$  angles used to map the photoemission intensity in the experiments performed. (d) CCD picture of the acquired spectra on the detector.

<sup>5</sup>The finite energy and angular resolution can be taken into account with a two-dimensional Gaussian convolved with the original spectral function.

The SPECS Phoibos 150 spectrometer consists of three main parts (see Fig. 2.5): a system of lenses, a set of two concentric hemispheres and a detector.

The cylindrical electrostatic lenses focus the photoelectron beam into an entrance slit that separates the lenses from the hemispherical part. The latter consists of two concentric hemispheres where two different negative potentials are applied so as to form a bandpass filter. The potentials are tuned such that only electrons that have an energy between  $E_p - \Delta$  and  $E_p + \Delta$  can reach a two-dimensional detector as shown in figure Fig. 2.5.  $E_p$  is called the pass energy and it defines the energy resolution of the analyser, while  $\Delta$  defines the size of the energy window.

In the plane that contains the lenses and the detector (dispersive plane) the energy is discriminated. The advanced system of lenses allows the angular information to be carried to the detector.

Only electrons emitted in the range of angles between  $+\beta$  and  $-\beta$  (where  $\beta$  is defined by the voltages on the lenses) with respect to the longitudinal axis of the lenses are able to reach the detector. The lenses are the core of the system as they not only set a small acceptance angle in the direction parallel to the dispersive plane, but also conserve the orientation of the photoelectron momentum in a plane that contains the axis of the lenses and is orthogonal to the dispersive plane. Furthermore the lenses reduce by a constant amount the kinetic energy of the incoming electrons in such a way that the electrons with the desired kinetic energy reach the entrance slit with an energy of  $E_p$ . The advantage of such an analyser is that it produces, in a single shot, a set of intensity profiles versus kinetic energy (EDC — energy distribution curve) over a range of  $\phi$  angles for a given  $\theta$ . Please note that here the angles  $\phi$  and  $\theta$  are both polar angles along orthogonal directions. This property defines the scheme and the geometry of the experiment that is depicted in Fig. 2.5.

A complete map of the Fermi surface can then be obtained by simply rotating the sample in front of the analyser around an axis orthogonal to the dispersive plane and acquiring a spectrum for each  $\theta$ . This is typically referred to as a “polar scan”. In this configuration, the relationship between the angles and  $\mathbf{k}_{\parallel}$  is

$$\mathbf{k}_{\parallel} = (\sin(\phi)\hat{\mathbf{x}} + \cos(\phi)\sin(\theta)\hat{\mathbf{y}}) \cdot \sqrt{\frac{2m_e E_{\text{kin}}}{\hbar^2}}, \quad (2.1)$$

where  $E_{\text{kin}}$  is the kinetic energy of the photoemitted electron. The two-dimensional detector consists of an amplifier, made by two microchannel plates (MCP), that increases the intensity of the electron beam, which is subsequently accelerated towards a phosphor screen. Each spectrum will then be acquired by a low noise and high resolution CCD camera in the form of an image that gives in contrast scale the photoemission intensity versus kinetic energy for every  $\phi$  angle between  $+\beta$  and  $-\beta$  at a certain  $\theta$ . This three dimensional dataset  $I(E_{\text{kin}}, \theta, \phi)$  obtained by stacking the images will then allow us to map the spectral function along different directions in the surface Brillouin zone.

In this context two main types of aberrations have to be considered: one concerning energy, known as astigmatism, and one in the angular dimension  $\phi$ . The first one is unavoidable for hemispherical analysers and leads to electrons with the same kinetic energy appearing to have different kinetic energies as a function of the emission angle. This means, for example, that a constant Fermi edge as a function of the photoemission angle appears to be dispersing with angle, mimicing the curvature of the hemispheres. This can easily be corrected using a curved entrance slit in front of the hemispheres.

The second aberration is angular in nature and leads electrons with different kinetic energies, but photoemitted in the same direction, to be detected at different emission angles. This aberration comes from the spherical geometry of the analyser and can either be corrected

by detuning the lenses or via software warping post-measurement. In the case of this work the latter is the method used and the deformation (i.e. the warping parameters) is known both from the specifications of the instrument and from testing with model systems (e.g. the Au(111) or Cu(111) surface states). Thus the original angular dispersion can be recovered.

### 3D mapping

Roughly speaking, in order to map the  $k_z$  dispersion of the observed states, or to verify if the spectra observed have a 2D or 3D character, the power of the beamline needs to be completely exploited. In order to do so, what is performed is a  $h\nu$  scan where spectra are acquired as function of angle and photon energy. The rule of thumb of such a measurement is the following: what disperses with  $h\nu$  has a 3D character; what appears at the same binding energy regardless of  $h\nu$  is 2D. Let us discuss briefly such an effect in the very same way as it is done in Ref. [52].

In the brief theoretical introduction it has been mentioned that  $k_z$  is not a good quantum number near the surface because of the broken translational symmetry. Even ignoring this, it would not be possible to recover the  $k_z$  inside the sample from the value measured outside, due to the potential gradient at the surface barrier that leads to a refraction effect [70]. Provided that the dispersion of the final states is known, it can still be possible to recover the  $k_z$  of the initial state from the photoemission spectra, as shown in Fig. 2.6(a). As the photon energy is changed, it is evident that different initial state energies and  $k_z$  values can be probed leading the bulk state in question to appear as a peak at different binding energies depending on the  $h\nu$  used. The state's binding energies at high symmetry points ( $k_z = n\pi/a$  where  $n = 0, 1, 2, \dots$  and  $a$  is the one-dimensional lattice constant perpendicular to the surface) can easily be read from the spectra (e.g. in Ref. [16]), but the detailed dispersion of the state can only be recovered if the final state dispersion is known. If this is not the case, it is often possible to obtain a good approximation of the entire dispersion by assuming final states of a simple free electron form. It is then possible to calculate  $k_z$  plus or minus a reciprocal lattice vector as a function of the emission angle  $\theta$  and the inner potential  $V_0$  using

$$k_z = \sqrt{\frac{2m_e}{\hbar^2}(V_0 + E_{\text{kin}} \cos^2(\theta))}. \quad (2.2)$$

The inner potential  $V_0$  can be determined iteratively by requiring the resulting  $k_z$  to be consistent with the binding energy extrema at symmetry points.

The fact that  $k_z$  is not well-defined cannot be neglected. In particular, the finite escape depth of the photoelectron leads to a  $k_z$  broadening  $\delta k_z$ . As the state disperses in the  $k_z$  direction, this also leads to an energy broadening  $\delta E$ , as illustrated in Fig. 2.6(a).

This problem is absent for photoemission from surface states and quantum-confined states, shown in Fig. 2.6(b) and (c), respectively (the quantum confinement has only been introduced for the lowest band). Strictly speaking, neither the surface state nor the quantum confined state have a well-defined  $k_z$  because they are localized in the  $z$  direction. This is usually a much more severe restriction for the more strongly confined surface states than for the deeply penetrating QWS. In neither case does the wave function lose its periodicity perpendicular to the surface completely and the Bloch wave character in the  $z$  direction is partly retained. Thus, the markers in the figure symbolise the  $k_z$  value the state is derived from and the horizontal lines symbolise that  $k_z$  is not defined anymore. In any case, the absence of a dispersion with  $k_z$  implies directly that a  $k_z$  broadening does not result in an energy broadening in the photoemission spectra, unlike the case for the bulk states. This implies that it is often easier to determine a bulk band structure in the presence of quantum confinement than in its

absence [71]. The fact that  $k_z$  is ill-defined also implies that surface states and QWS can not only be observed for one photon energy but for a broad range of photon energies.

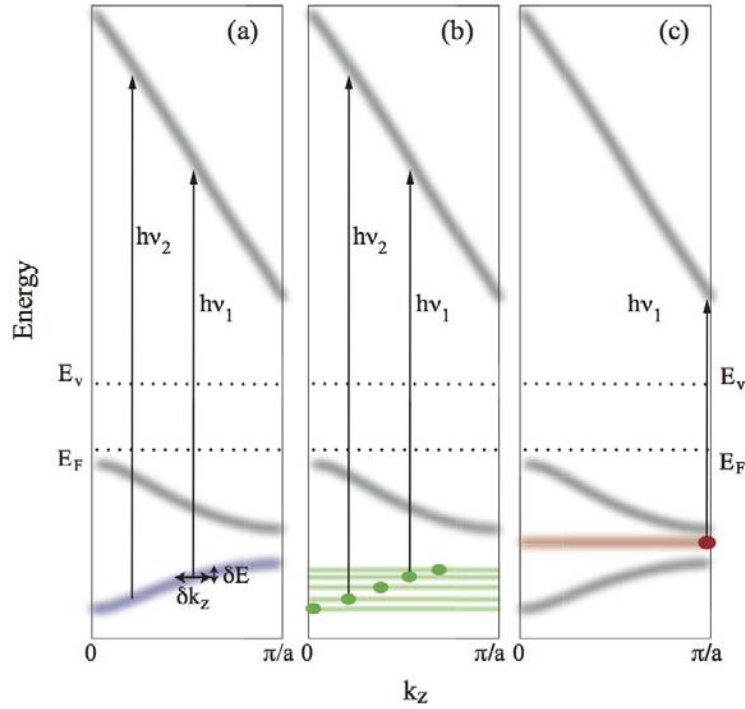


Figure 2.6: Schematic picture of the photoemission process from different types of electronic states.  $E_F$  and  $E_V$  are the Fermi and vacuum level, respectively. (a) Bulk states measured with different photon energies appear at different binding energies in the spectrum, i.e. they show dispersion. The fact that  $k_z$  is not well-defined leads to a broadening  $\delta k_z$  that is then reflected in an energy broadening  $\delta E$  of the observed peaks. (b) Quantum well states are derived from restricting the possible  $k_z$  values in a structure (green markers, only shown for the lowest band) but the  $k_z$  broadening (green lines) implies that they can be observed for a range of photon energies. As they do not show dispersion, this will not lead to an energy broadening. Similar arguments hold for surface states (c).



# Chapter 3

## Projects and Results

It is important to mention the scientists involved in each of these projects and without whom it would not have been possible to obtain these results. For this reason at the beginning of each section will be mentioned the people involved in the project.

### 3.1 Sb(110): Fermi surface mapping and topology

Marco Bianchi<sup>1</sup>, Dandan Guan<sup>1,2</sup>, Anna Stróżecka<sup>3</sup>, Celia H. Voetmann<sup>1</sup>, Shining Bao<sup>2</sup>, Jose Ignacio Pascual<sup>3</sup>, Asier Eiguren<sup>4,5</sup> and Philip Hofmann<sup>1</sup>

Contribution: sample preparation, experiment and acquisition, analysis.

Reference Paper: *Surface states on a topologically non-trivial semimetal: The case of Sb(110)*, M. Bianchi, *et al.*, Phys. Rev. B **85**, 155431 (2012).

The bulk band structure of Sb has the characteristics of a strong topological insulator with a  $\mathbb{Z}_2$  invariant  $\nu_0 = 1$  (see Figs. 1.9, 1.10 and Refs. [45, 72]). As we have discussed in Chap. 1.2.2, this requires the existence of metallic states at the surface and puts constraints on the expected topology of the surface Fermi contour. However, Sb is a semimetal, not an insulator, and these constraints are therefore partially relaxed. An interesting question is what these considerations imply for the semimetal surfaces. Strictly speaking, there is no fundamental reason to expect metallic surface states on Bi or Sb, but such states have so far always been found and appear to be quite robust.

Experimental results on the electronic structure of Sb surfaces have so far been reported only for Sb(111) [72], while the topology has been discussed in Refs. [4, 45]. The (110) surface

---

<sup>1</sup>Department of Physics and Astronomy, Interdisciplinary Nanoscience Center, Aarhus University, 8000 Aarhus C, Denmark

<sup>2</sup>Department of Physics, Zhejiang University, Hangzhou, 310027 China.

<sup>3</sup>Institut für Experimentalphysik, Freie Universität Berlin, 14195 Berlin, Germany.

<sup>4</sup>Departamento de Física de la Materia Condensada, EHU/UPV, Barrio Sarriena sn 48940 Leioa, Spain.

<sup>5</sup>Donostia International Physics Center (DIPC), Paseo Manuel de Lardizabal.

is nevertheless interesting for two reasons: the nontrivial bulk topology of Sb and, compared to the (111) surface, the (110) has more distinct TRIMs (four instead of two, see Fig. 1.10 and 1.9) and this provides the opportunity to study the surface-state topology in more detail.

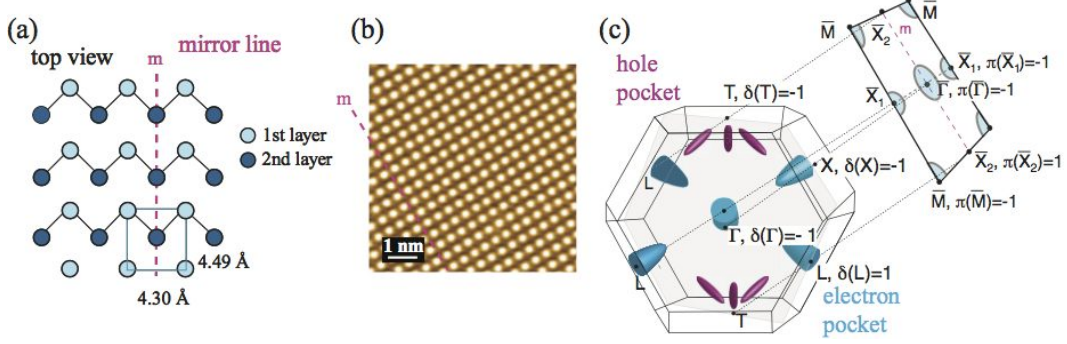


Figure 3.1: (a) Truncated-bulk geometric structure of Sb(110). (b) STM topography of the surface. (c) Bulk Brillouin zone of Sb with a sketch of the Fermi-surface elements (qualitatively and not to scale), together with a projection onto the Sb(110) surface Brillouin zone. The grey plane is a bulk mirror plane which projects onto a surface mirror line. For the eight bulk time-reversal-invariant momenta (TRIMs) the parity invariants  $\delta(\Lambda_j)$  are given and projected into the surface resulting in the denoted surface fermion parities  $\pi(\bar{\lambda}_i)$  [36]. The qualitative prediction of the Fermi surface is depicted by blue circles.

The theoretical conclusion concerning the shape of the Fermi surface is simple: there must be an odd number of Fermi level crossings between  $\bar{X}_2$  and any other surface TRIM, and an even number between two surface TRIMs not involving  $\bar{X}_2$ . This has been explained in Chap. 1.2.4 and is here summarised in Fig. 3.1, together with a STM topography of the Sb(110) surface.

What will be argued here is that, while the semi-metallic character of the substrate prohibits a statement about the global existence of surface states, the dispersion of states in certain high-symmetry directions of k-space (directions without bulk projected states) can still be rigorously compared to topological predictions.

The Sb(110) surface was cleaned *in situ* by cycles of sputtering and annealing to 520 K. During the surface preparation it is necessary that the cooling rate is kept  $\lesssim 1^\circ\text{C}/\text{s}$  in order to obtain good quality. A clear  $(1 \times 1)$  low energy electron diffraction pattern was observed for the clean surface. The pattern showed the only symmetry to be the mirror line that defines the  $\bar{\Gamma}\bar{X}_2$  direction of the surface Brillouin zone. The ARPES results shown here were acquired with a combined energy and angular resolution better than 10 meV and  $0.13^\circ$ , respectively, and  $h\nu = 20$  eV. The Fermi surface map was obtained by merging three consecutive angular scans acquired with different tilts as described in Fig. 3.2.

Fig. 3.3 shows the photoemission intensity at the Fermi level while Fig. 3.5 shows it as a function of binding energy along some high-symmetry directions. For clarity, both figures show the measured intensity and the same intensity superimposed with coloured lines to guide the eye. This will become useful for the identification of the surface states and the projected bulk band structure. These lines are only drawn where the data show clearly identifiable structures; they are not representations of the actual Fermi contour or dispersion, which is expected to continue after the coloured lines end. The light yellow areas represent

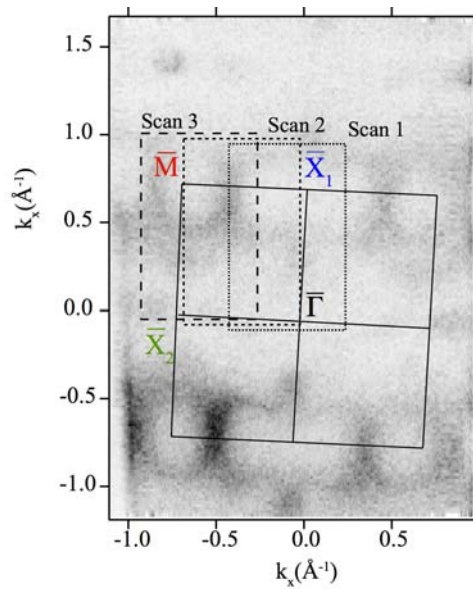


Figure 3.2: Photoemission intensity at the Fermi level acquired with  $h\nu=70$  eV. The dashed lines depicts the areas measured during each scan used to obtain the Fermi surface maps at  $h\nu=20$  eV. The continuous line indicates the SBZ.

the projection of the bulk band structure onto the (110) surface as obtained by using the tight-binding scheme described by Liu and Allen in Ref. [53]. This is expected to give reliable results very close to the Fermi energy, since the tight-binding parameters have been optimised to reproduce the bulk Fermi surface.

The Fermi contour in Fig. 3.3 shows several surface-related features, identified by their location outside the projected band continuum and the fact that their position is insensitive to the photon energy used. The most pronounced are a circular contour around  $\bar{M}$  (outlined in red) and a “butterfly-like” feature that encloses the  $\bar{X}_1$  point (blue). Two smaller pockets are also seen along the  $\bar{M}\bar{X}_2$  line (light blue) and the  $\bar{X}_2\bar{\Gamma}$  (green). The latter falls partly into the bulk continuum and thus has the character of a surface resonance there.

Finally, a faint trace is visible, splitting off from the “butterfly wing” towards  $\bar{X}_2$  (magenta) and some faint intensity crossing the  $\bar{X}_2\bar{\Gamma}$  line (also magenta). Results of DFT calculations shown in Fig. 3.4 suggest that these probably join to form a large hole pocket around  $\bar{\Gamma}$ , but this is not clearly seen in the data. An open Fermi contour would also be unphysical.

A detailed description of the DFT calculations can be found in the reference paper, where the system has been modelled using a repeated slab system consisting of 54 layers. This has been implemented by our collaborators. The bulk band projection is consistent with the tight-binding result, though small errors in such a calculation or merely the limited slab size can qualitatively change the projected Fermi surface in a semimetal, where the electron and hole pockets of the Fermi surface are less than 100 meV deep. Overall, a very good agreement with the experimental findings is obtained: the deviation between measured and calculated surface-state is usually below 100 meV. This can be considered satisfactory given the intrinsic accuracy limits of the calculation. The main features of the measured Fermi contour are immediately recognised, especially the butterfly close to  $\bar{X}_1$  and the hole pocket around  $\bar{M}$ .

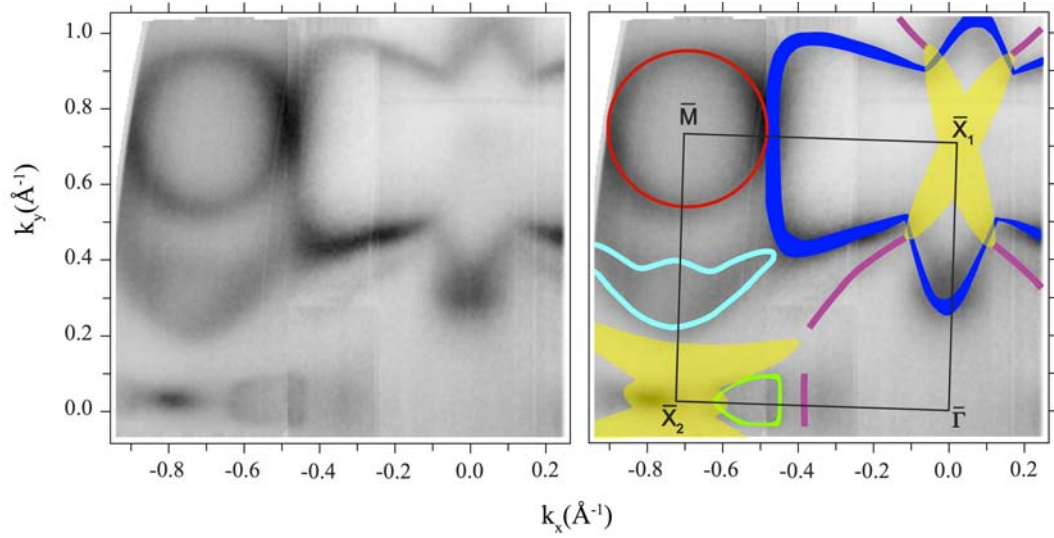


Figure 3.3: Photoemission intensity at the Fermi level. Dark corresponds to high intensity and the dark features outside the projected bulk band continuum are interpreted as the surface Fermi contour. The left part of the figure shows the raw data, whereas the different structures are indicated by coloured lines as a guide to the eye on the right part. Different colours are used for different surface-state features. The light yellow areas correspond to the projected bulk Fermi surface (states within  $\pm 5$  meV of the Fermi energy), calculated using the tight-binding parameters from Liu and Allen [53].

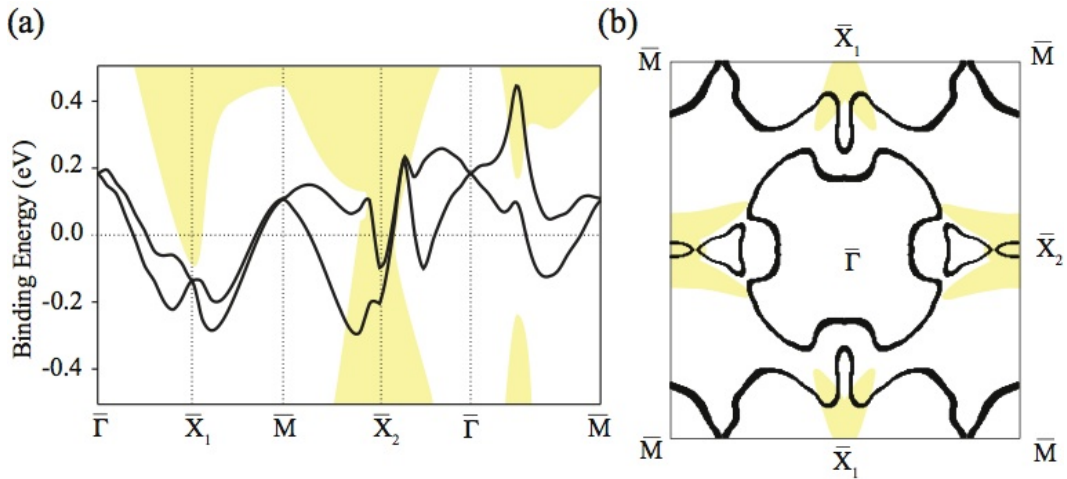


Figure 3.4: (a) Surface-state dispersion and (b) calculated Fermi contour. The lines represent the surface states from the DFT slab calculation. The yellow continuum is the projected bulk band structure calculated using the tight-binding parameters from Liu and Allen [53].

The detailed character of the features can be identified from the dispersion shown in Fig. 3.5. The circular contour around  $\bar{M}$  (red) is a hole pocket, whereas the feature along  $\bar{M}\bar{X}_2$  (light blue) is a shallow electron pocket. These two can be interpreted as spin-orbit split

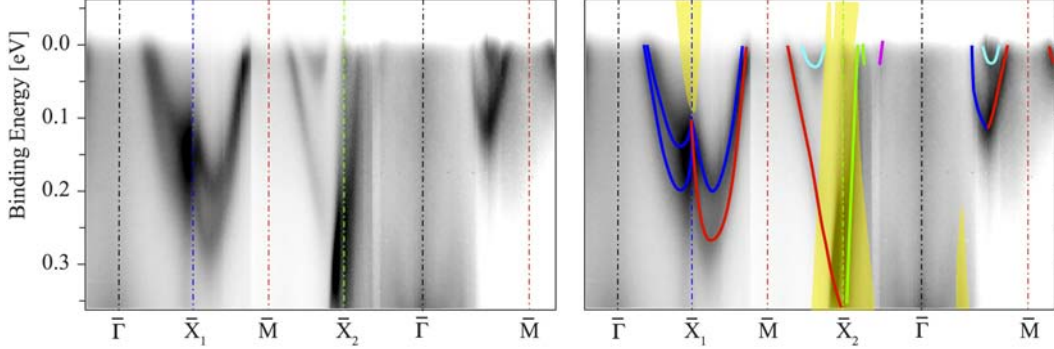


Figure 3.5: Photoemission intensity as a function of binding energy along different directions of the surface Brillouin zone. The left part shows the raw data. In the right part, the observed bands are emphasised by coloured lines. The colours correspond to those used in Fig. 3.3. The light yellow areas represent the projected bulk band structure.

partners stemming from the same state, and this is confirmed by DFT calculations shown in Fig. 3.4. Unfortunately our experimental setup does not allow spin identification, though this interpretation is consistent with the findings on other Bi, Sb, and  $\text{Bi}_{1-x}\text{Sb}_x$  surfaces. On these surfaces the states are also degenerate at points where this degeneracy is enforced by symmetry (the TRIMs). The spectra shows that the state is unoccupied and it can be assumed to be spin degenerate at  $\bar{M}$ , but split away from this high-symmetry point on the SBZ boundary. The spin degeneracy is indeed required not only at the  $\bar{\Gamma}$  point, as explained in Chap. 1.1.2, but the combination of time-reversal symmetry with translational symmetry dictates that the splitting must also be zero for any TRIM. One of the split bands forms the hole pocket and disperses steeply downward. The other one forms the electron pocket along  $\bar{M}\bar{X}_2$ . This does not effect the topological character of the surface. Also at  $\bar{X}_1$  the state is twofold degenerate but it is occupied and can thus be observed by ARPES. Away from  $\bar{X}_1$ , the state clearly splits into two bands both along  $\bar{X}_1\bar{M}$  and  $\bar{X}_1\bar{\Gamma}$ , then merges again and the splitting is too small to be distinguished at  $E_F$  along these high-symmetry directions. Consequently, the Fermi level crossings along  $\bar{X}_1\bar{\Gamma}$  and  $\bar{X}_1\bar{M}$  are double crossings. Close to the  $\bar{X}_1\bar{M}$  direction, the two bands forming the double crossing separate into the circle and the butterfly. The weakest feature in the data is the band which splits off from the butterfly structure and disperses towards  $\bar{X}_2$  (magenta). Its presence is clearly required by the overall Fermi contour topology: the two spin-split surface-state branches are occupied at  $\bar{X}_1$  and empty at  $\bar{M}$  and  $\bar{\Gamma}$ . Consequently, two Fermi level crossings have to be found along the corresponding high-symmetry lines. Along the  $\bar{X}_1\bar{M}$  direction, the two crossings are formed by the circular contour around  $\bar{M}$  and the “wing” of the butterfly, which is non-degenerate. Along  $\bar{X}_1\bar{\Gamma}$ , the blue feature is two-fold degenerate. The weak magenta feature corresponds to the second Fermi level crossing. As it disperses away from the butterfly, its intensity diminishes so much that it can not be established whether it continues to the  $\bar{X}_2\bar{\Gamma}$  line and merges with the other magenta feature observed there, or if it merges into the projected bulk bands close to  $\bar{X}_2$ .

The identification of the electronic structure near the  $\bar{X}_2\bar{\Gamma}$  line is more difficult due to the presence of bulk states. As pointed out above, the feature outlined in green appears to be a closed pocket around this line, but it falls partly into the bulk continuum. Also, only the band giving rise to the crossing nearest to  $\bar{X}_2$  is clearly identifiable in the dispersion, the crossing further away from  $\bar{X}_2$  is very weak, and the dispersion can not be followed to higher binding energies. Nevertheless, the dispersion of the first band suggests that the pocket is a hole pocket. The magenta feature is well separated from the bulk continuum at the Fermi level, but it is very broad and its dispersion is only clearly observed near  $E_F$ . The sign of its group velocity would be consistent with the feature being part of a hole pocket around  $\bar{\Gamma}$ .

Concerning the DFT results, some smaller details are not entirely captured by the calculations. First, the very shallow electron pocket along  $\bar{M}\bar{X}_2$  appears in the calculations as a dip in the dispersion of the band not crossing  $E_F$ . This can be accounted for by small uncertainties in the calculations, and as said before, the presence of this electron pocket does not affect the topological character of the surface states. The second difference between the measurements and the calculation is the large hole pocket encircling the  $\bar{\Gamma}$  point in the latter. One should consider, however, that a slightly different dispersion in the theory would cause this pocket to merge with the butterfly structure, giving rise to the experimentally observed double crossing on the  $\bar{\Gamma}\bar{X}_1$  line and to the weak structure split off the butterfly when going from this line toward  $\bar{M}$ . As said before this merging (magenta lines in Fig. 3.3) would give rise to a large electron pocket around  $\bar{\Gamma}$ , that is a more physical situation than an open Fermi contour. It should be noted that many-body effects such as correlations or the electron-phonon coupling are not included in the calculations. As described in Chap. 1.3.1, this can affect the dispersion close to  $E_F$  via the real part of the self-energy. The absolute magnitude of such effects is not expected to be large for Sb, but effects of the order of several tens of meV are certainly possible and would be noticeable.

We can thus already draw the following conclusions: the electronic structure of Sb(110) shows several electronic surface states crossing the Fermi level. The surface therefore has the character of a good metal in contrast to the semi-metallic bulk. This appears to be a general feature of the Bi and Sb surfaces and it has been explained as a result of the combination of symmetry breaking and a strong spin-orbit interaction [72, 73, 74, 75, 76].

In order to discuss topology, we can start with a close inspection of Fig. 3.5. This shows that the theoretical conclusion concerning the shape of the Fermi surface predicted by Teo, Fu and Kane, described in Chap. 1.2.4 and summarised in Fig. 3.1(c), is correct, despite the presence of bulk Fermi-surface projections. This is clearest for the  $\bar{X}_1$  point where we find the two states to be degenerate, as predicted, and in both the  $\bar{X}_1\bar{\Gamma}$  and  $\bar{X}_1\bar{M}$  directions we find two Fermi level crossings, also in agreement with the prediction.

The situation is difficult to determine for  $\bar{X}_2$  solely on the basis of our experiments as the intensity of the surface bands is very weak here, due to the presence of the bulk band continuum. At first glance, the number of Fermi level crossings seems to be as predicted from the topological arguments: along both directions,  $\bar{M}\bar{X}_2$  and  $\bar{X}_2\bar{\Gamma}$ , we can identify one closed contour plus an extra crossing, and thus an odd number of crossings. Comparing to the topological predictions based on the surface fermion parity, we expect an odd number of contours around  $\bar{\Gamma}$ ,  $\bar{M}$ , and  $\bar{X}_1$  and an even number around  $\bar{X}_2$ . For  $\bar{M}$  this is fulfilled, as the point is encircled by one hole pocket and  $\bar{X}_1$  is also encircled by only one contour. Concerning  $\bar{\Gamma}$  the situation is unclear, as it depends on the weak feature which splits off from the butterfly. As mentioned before, it is likely that this feature connects to the observed crossing along the  $\bar{X}_1\bar{\Gamma}$  line, giving rise to a circular contour around  $\bar{\Gamma}$ , as also suggested by the DFT calculations shown in Fig. 3.4(b) [77]. For  $\bar{X}_2$  the situation is obscured by the projected bands and it is difficult to determine whether this state is encircled by any closed

Fermi contour. However the metallic bulk states projection onto the surface undermines the assumption that the bulk is insulating, which is a prerequisite of the topological theory that predicts the surface fermion parity rules.

This raises concerns over the use of topological arguments to make firm predictions about semimetal surface states. Naively, it can be expected that the topological predictions will not hold in these systems, because of their derivation under the condition of an insulating bulk. Fortunately, this is not quite the case. In fact, we have found that the topological predictions are mostly followed here, as for the other semimetal surfaces studied so far [36], and there are reasons why one should expect this.

The need for an odd number of Fermi level crossings between surface TRIMs arises because of their different surface fermion parity. In an insulator, due to the existence of a global energy gap around  $E_F$ , the necessary parity change between surface TRIMs can only be achieved by surface states. However a bulk state can also be used for this purpose in the case of a semimetal, if a projected bulk Fermi surface can be found between the two surface TRIMs. This argument implies that the number of FL crossings between TRIMs, without any projected Fermi surface in between them, should also be protected. For Sb(110), such a connection is only present between  $\bar{\Gamma}$  and  $\bar{M}$ , and this cut does indeed show the predicted number of crossings.

We can try to make similar arguments for the  $\bar{X}_1\bar{\Gamma}$  and  $\bar{X}_1\bar{M}$  directions. These do not in principle hold because a bulk Fermi-surface projection falls here. However the surface-state dispersion lies completely outside that, apparently following the topological predictions. In all these situations, we only observe an even number of Fermi level crossings between two TRIMs and thus a topologically trivial situation. Similar considerations can also be found in [45] for the case of Sb(111).

Concluding, experimental results and DFT calculations on the electronic structure of Sb(110), a non-(111) surface of a topologically non-trivial material have been presented. Along directions connecting TRIMs without any bulk Fermi-surface contribution, the observed band dispersion is in excellent agreement with the predictions of the surface bands topology. The topological arguments become invalid if the projected bulk Fermi surface is present and the surface bands are allowed to mix with the bulk states.

## 3.2 Bi<sub>2</sub>Se<sub>3</sub>, Rashba and quantum well states

In Chap. 1.2.4 we have seen how Bi<sub>2</sub>Se<sub>3</sub> represents the prototypical topological insulator due to the simplicity of its Fermi surface. For this reason, it has recently become one of the most common systems used to study topological effects in surface electronic structure. Furthermore, the lifted spin degeneracy, that is intrinsic for a topological state (TS), can be used for advanced studies in spin dynamics to be exploited in future electronics. Apart from this, it is impressive how the exotic bulk electronic structure turns this system into a fruitful playground for many of the more traditional effects in electronic surface science shown in this chapter: from band-bending near the surface, through quantum well states to the Rashba effect. This immediately clarifies the reason why so much attention has been focussed onto Bi<sub>2</sub>Se<sub>3</sub> during this project and why it has been chosen as the main subject of this work.

At the beginning of this study, the bismuth chalcogenide alloys had already been investigated via photoemission, either in the form of bulk crystals [78], or epitaxially grown on different substrates (e.g. Si(111) in Ref. [49]), and the field was quickly growing. Most of the attention was focussed on the topological state, though an unexpected and disturbing ageing effect in Bi<sub>2</sub>Se<sub>3</sub> (and less evidently in Bi<sub>2</sub>Te<sub>3</sub>) was observed. This consists of a shift towards higher binding energies of the topological state's spectroscopic features and was already suggested to be an indication of a band bending in Refs. [46, 79]. Furthermore, depending on crystal quality and measurement conditions, this has been observed to be frequently followed by the appearance of additional states in the conduction band (CB) and valence band (VB) regions. This effect and the additional states were not investigated thoroughly at that time.

Amongst the important unresolved issues linked to the basic electronic structure of these materials, this is what had attracted our attention, having the intuition that simple and more traditional physics was involved in this more than the theory of topology. Furthermore, in order to study the topological state in detail, an investigation of such spectroscopic changes was evidently necessary.

### 3.2.1 Sample growth and preparation

Bi<sub>2</sub>Se<sub>3</sub> has been studied historically for its thermoelectric properties and therefore different ways of growing the crystals have been developed. Unfortunately, most of them are not able to reproduce the level of quality needed for our type of measurement. Both Bi<sub>2</sub>Se<sub>3</sub> and Bi<sub>2</sub>Te<sub>3</sub> crystals obtained from stoichiometric mixtures are known to be highly n-doped [78, 80] due to the presence of defects in the bulk, which are mainly charged Se/Te vacancies [81]. This electron doping is evident from the position of the Fermi edge that is situated over the bottom of the CB. Phase segregation is also a serious effect that causes considerable issues concerning the crystals' homogeneity. However, thanks to the efforts of our chemist collaborators in Aarhus, it has been possible to reach the level of quality needed for our study. The crystals were grown by J.L. Mi<sup>6</sup> in the group of B.B. Iversen<sup>6</sup> in the Centre for Materials Crystallography at Aarhus University.

Many different crystals were grown with different recipes and they differ in quality and intrinsic doping. The crystals were named in numerical order, generation I being first. In this work only results from three different Bi<sub>2</sub>Se<sub>3</sub> crystals are shown, unless otherwise stated.

The first two batches of crystals, which will be referred to as intrinsic (generations II and V), were obtained from stoichiometric mixtures of 5N purity Bi and Se that were melted at 860°C for 24 hours in an evacuated quartz ampoule. These were then cooled down to 650°C at a rate of 2.5°C/h, and then annealed at 650°C for another 2 days (gen. II) or 7 days (gen. V). The crystal structure and quality were determined using X-ray diffraction at room

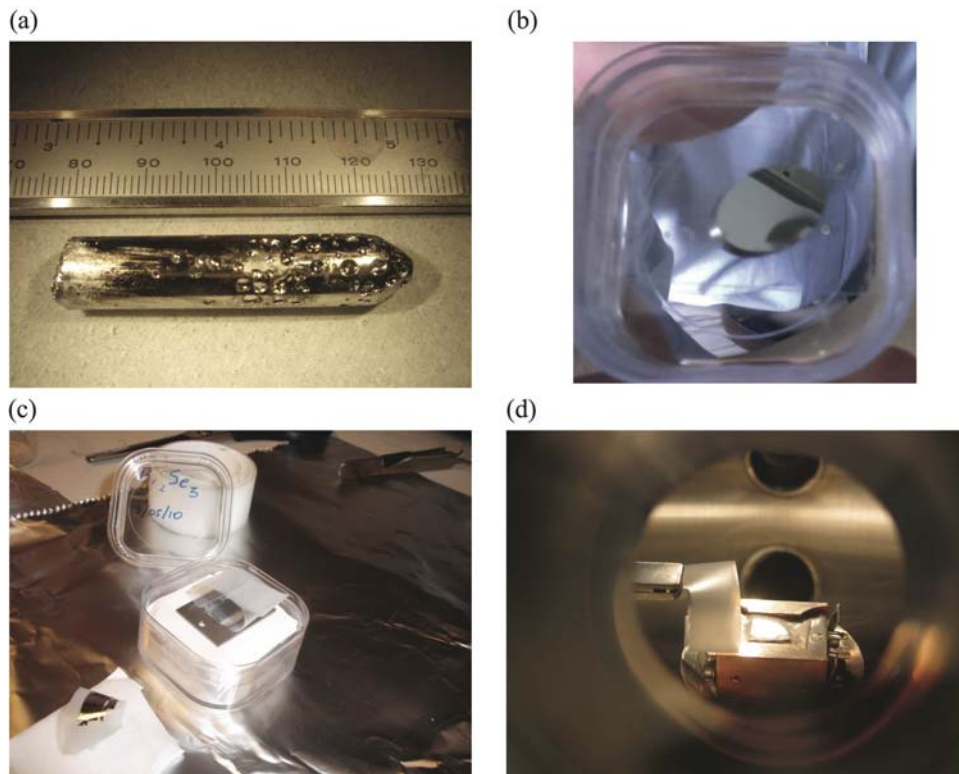


Figure 3.6: (a) The crystal as obtained from the growth procedure, this is the gen. V crystal. (b) A sample extracted from (a). (c) Sample glued on the Ta sample holder (gen. II) and a piece of Scotch tape after the cleave with removed layers on it. (d) Image of the sample just before cleaving it in vacuum in the LL.

temperature and the structure obtained is shown in Fig. 1.8.

The first batch (gen. II) differs in growth technique from the second (gen. V) because of another treatment meant to increase the quality of the crystal (particularly the size of the cleavable flakes). After the last annealing, the crystal was put into another evacuated quartz ampoule with a conical bottom and was zone melted using an induction coil with a rate of 1.2 mm/h. The crystal quality obtained from this technique was disappointing and its use was therefore discontinued in future generations.

The difference in growing procedure between these two generations leads gen. V to have bigger cleavable surfaces and sharper surface states, without any significant difference in the doping (as can be seen comparing Fig. 3.7(a) with 3.9(a)). This is an indication of a better surface quality and homogeneity.

A third batch, which will be referred to as Ca-doped (also gen. VII), was obtained from a mixture of Bi (5N purity), Se (5N purity) and Ca (99.5% purity) in the ratios Bi : Se : Ca = 1.996 : 3 : 0.004 melted at 860°C for 24 h in an evacuated quartz ampoule. Once cooled down from 860 to 750 °C at a rate of 50°C/h and then from 750 to 600°C at a rate of 2°C/h, it was annealed at 600 °C for 7 days. The Ca is able to counter-dope the charged Se vacancies, restoring the Dirac point to  $E_F$ . With this, the insulating state is recovered, while the long cooling time produces large crystals.

The particular layered structure of these compounds and the weak van der Waals interaction between the quintuple layers allow us to obtain a clean Se-terminated (111) surface using a simple cleaving technique.

What must be pointed out is that although the cleaving procedure is extremely simple, the quality of the surface obtained is somewhat unpredictable, despite the improvements made in sample quality. For this reason many different samples and cleaves have been measured and characterised that qualitatively show the same behaviour.

Fig. 3.6(a) shows one of the crystals from which samples of a 1–2 mm thickness have been extracted. Each sample was then mounted with conductive epoxy on a Ta sample holder. A thermocouple (type K) was mounted in close contact with the back of the sample in order to monitor the temperature during the measurements. The cleave was performed at room temperature and in vacuum (pressure lower than  $5 \times 10^{-8}$  mbar) with ordinary Scotch tape as shown in Fig. 3.6(d), then immediately transferred to the measurement position (on the He-cooled manipulator). During the transfer the pressure was lower than  $2 \times 10^{-9}$  mbar. The time elapsed between the cleave and the start of a measurement varied between 3 min and 20 min. All the data have been acquired at a pressure lower than  $4 \times 10^{-10}$  mbar and, when not specified, at a temperature of 60 K.

### 3.2.2 Basic spectral features

Figure 3.7(a) shows the topological state's spectroscopic signature, with its distinct V-shaped feature, forming a conical dispersion with the Dirac point (DP) at a binding energy of 365 meV. At the Fermi level, i.e. far away from the DP, the dispersion deviates from a simple cone and the constant energy surfaces are hexagonal according to Ref. [82], and this is shown in Fig. 3.7(b) and 3.9(a). The anisotropy of the Fermi velocity is known and explained for the analogous  $\text{Bi}_2\text{Te}_3$  case where the deviation from a perfect Dirac cone is more evident [78, 83]. The features at the highest binding energies and the region of high intensity inside the Dirac cone are due to emission from the bulk valence band (VB) and conduction band (CB), respectively. This demonstrates that despite the Se-enriched mixture used in the growth, these samples are still degenerately n-doped. We also see that the spectral features linked to the topological state are considerably sharper than those of the other states. This is

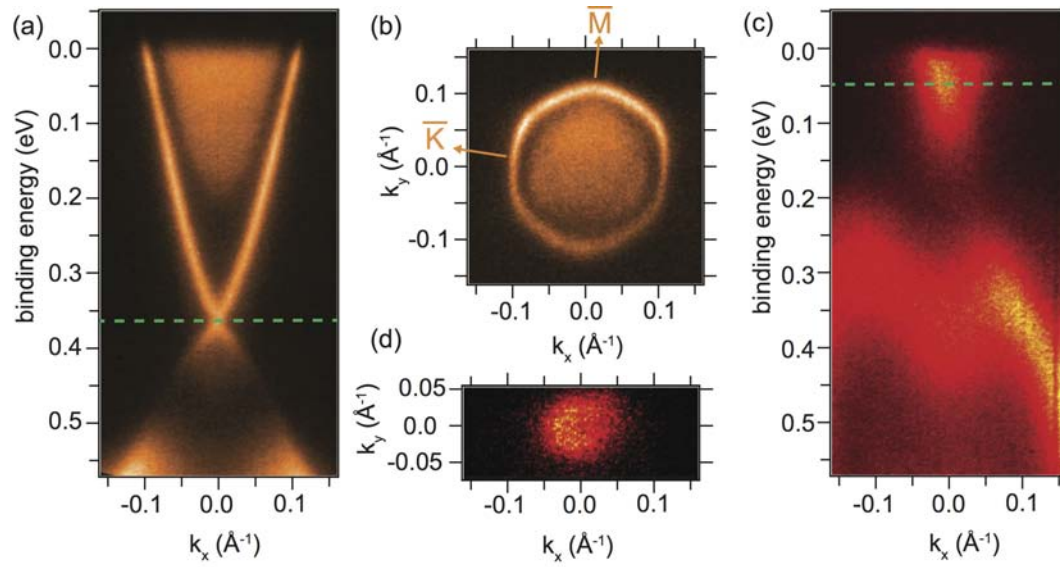


Figure 3.7: ARPES spectra for the pristine surface of  $\text{Bi}_2\text{Se}_3$ . Light colour indicates high photoemission intensity. (a) Energy dispersion in the  $\bar{K}\bar{\Gamma}\bar{K}$  direction of the SBZ and (b) Fermi surface for the stoichiometric  $\text{Bi}_2\text{Se}_3$  sample (generation V) with high symmetry directions indicated in yellow. (c) and (d) Energy dispersion and Fermi surface for the Ca-doped sample, respectively. The Dirac point is at a binding energy of  $\approx 50$  meV.

due to the  $k_z$ -smearing mentioned in connection with Fig. 2.6 and more extensively explained in Ref. [52].

The Ca doping allows us to shift the Dirac point from a binding energy of 365 meV to 47 meV as shown in Figs. 3.7(c) and (d), counteracting the natural doping. Unfortunately, the price for this is a broadening of the state, consistent with the higher degree of disorder due to the random distribution of dopants in substitutional Bi sites [84]. Such disorder is relevant even for surface states, as it induces an additional smearing in  $k_{\parallel}$ .

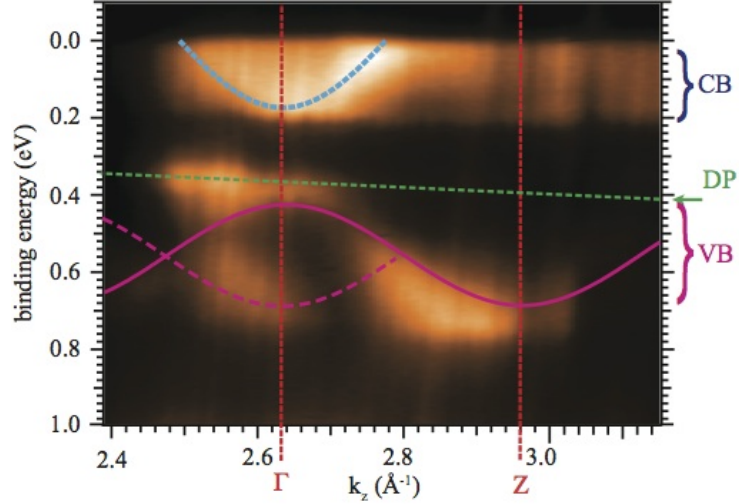


Figure 3.8: Bulk and surface components identification via  $h\nu$  scan on the pristine surface of intrinsic  $\text{Bi}_2\text{Se}_3$  (generation V), illustrating the dispersion of the states at normal emission as a function of  $k_z$ . The data shown are a subset of a larger photon energy scan between  $h\nu = 14$  eV and  $h\nu = 32$  eV. The drift of the Dirac point with photon energy is due to the ageing effect that occurs during the scan. The CB and VB (highlighted with blue and magenta lines as a guide to the eye) disperse, revealing the bulk  $\Gamma$  and  $Z$  points. The dashed magenta line is a shifted replica of the VB dispersion caused by a surface umklapp process.

Data shown in Fig. 3.8 have been acquired with an energy scan that, apart from facilitating the distinction between 2D and 3D features, shows the dispersion of the bulk states in the direction perpendicular to the surface. Here the photoemission intensity at normal emission acquired for the intrinsic sample is presented, extracted from a larger data set also containing off-normal spectra (similar to the one shown in Fig. 3.10).

Data were taken as a function of photon energy and here the horizontal axis has already been transformed into  $k_z$  values instead of  $h\nu$ , using Eq. 2.2. For this transformation, an inner potential of  $V_0 = 11.8$  eV was assumed according to Refs.[46, 85].

The dispersing features stem from the CB (blue) and VB (magenta), whose bottom and top, respectively, appear together at the bulk  $\Gamma$  point for  $k_z \approx 2.63 \text{ \AA}^{-1}$  corresponding to  $h\nu \approx 19.2$  eV. The bottom of the VB appears instead at  $k_z \approx 2.96 \text{ \AA}^{-1}$ , giving a  $\Gamma Z$  distance (see Fig. 1.9(a)) of  $0.329 \text{ \AA}^{-1}$ , consistent with the literature [86]. A third dispersing feature is visible identical to the VB related one, but this is weaker (dashed magenta line) and shifted in  $k_z$  by half a reciprocal lattice vector (i.e. its highest binding energy is at  $\Gamma$  instead of  $Z$ ). This can be attributed to an umklapp process involving a surface reciprocal lattice vector.

Such processes are well known for similar BZ shapes, where the  $k_z$  value of the  $\Gamma$  point in the first BZ is the same as that for the zone boundary in the neighbouring zone [16].

The position of the Dirac point, here highlighted by the dashed green line is not easily visible from this scan, but can be inferred looking at the entire dataset made of many images like Fig. 3.7(a) taken at different  $h\nu$ , where all the topological state is visible. The Dirac point shows a clear drift with  $k_z$ , which is unexpected as it is related to a 2D feature. This drift is not related to the change in  $h\nu$ , but is caused by the aforementioned ageing effect that occurs during the scan, that takes approximately 30 min in this case, and on which we will concentrate most of our attention (see Fig. 3.9).

### 3.2.3 Confinement of conduction band states

Marco Bianchi<sup>1</sup>, Dandan Guan<sup>1,2</sup>, Richard C. Hatch<sup>1</sup>, Shining Bao<sup>2</sup>, Jianli Mi<sup>6</sup>, Bo Brummerstedt Iversen<sup>6</sup>, Philip D.C. King<sup>7</sup>, and Philip Hofmann<sup>1</sup>

Contribution: experimental design, strategy and execution, sample preparation, acquisition, analysis.

Reference Paper: *Coexistence of the topological state and a two-dimensional electron gas on the surface of  $Bi_2Se_3$* , M. Bianchi, *et al.* **Nature Communications** **1**, 8, 128 (2010).

The ageing effect typically takes place between 30 min and several hours after cleaving the crystals. The ageing manifests itself clearly at 60 K and in a less pronounced manner at room temperature (room temperature measurements not shown). It consists of an increasing downward bending (n-doping) of the bands and eventually quantised two-dimensional states in the CB (2DEG) and VB (M-state) will also appear.

The 2DEG appears as a distinct parabolic rim around the bottom of the CB which then develops into a well separated state. Due to its parabolic shape and demonstrated 2D character, it will be referred to as a 2D electron gas (2DEG), a basic concept in solid state physics. This choice will appear justified after the following discussion. As time elapses the 2DEG eventually shows a splitting that is strongly reminiscent of a Rashba-type spin-orbit splitting of 2D states, similar to the surface states described above and involving heavy elements such as Au or Bi [31, 73, 75, 87]. Furthermore, these 2DEGs are indeed non-degenerate in spin away from  $\bar{\Gamma}$  as seen in spin-sensitive measurements [47]. A second 2D state appears as an M-shaped state at the bottom of the VB that develops by moving further away from the VB, see Fig. 3.12. We will come back to these two effects, the splitting of the 2DEG and the additional M-shaped states, in the following chapters. The effect has a tendency to saturate over a time scale that may change slightly from cleave to cleave and between different samples. For this reason the time information that will be given further on has to be considered indicative. However, as a general trend, after 30 min it is possible to observe the emergence of these additional states and these become split after approximately 20 hours.

Figs. 3.9 and 3.11 summarise the ageing effect for gen. II and gen.V, respectively. At the Fermi level, i.e. far away from the Dirac point, the dispersion deviates from a simple cone and the constant energy surfaces are hexagonal (similar to Fig. 3.7(b)). This becomes more

---

<sup>6</sup>Center for Materials Crystallography, Department of Chemistry, Interdisciplinary Nanoscience Center, Aarhus University, Aarhus C 8000, Denmark.

<sup>7</sup>School of Physics and Astronomy, University of St Andrews, St Andrews KY16 9SS, UK.

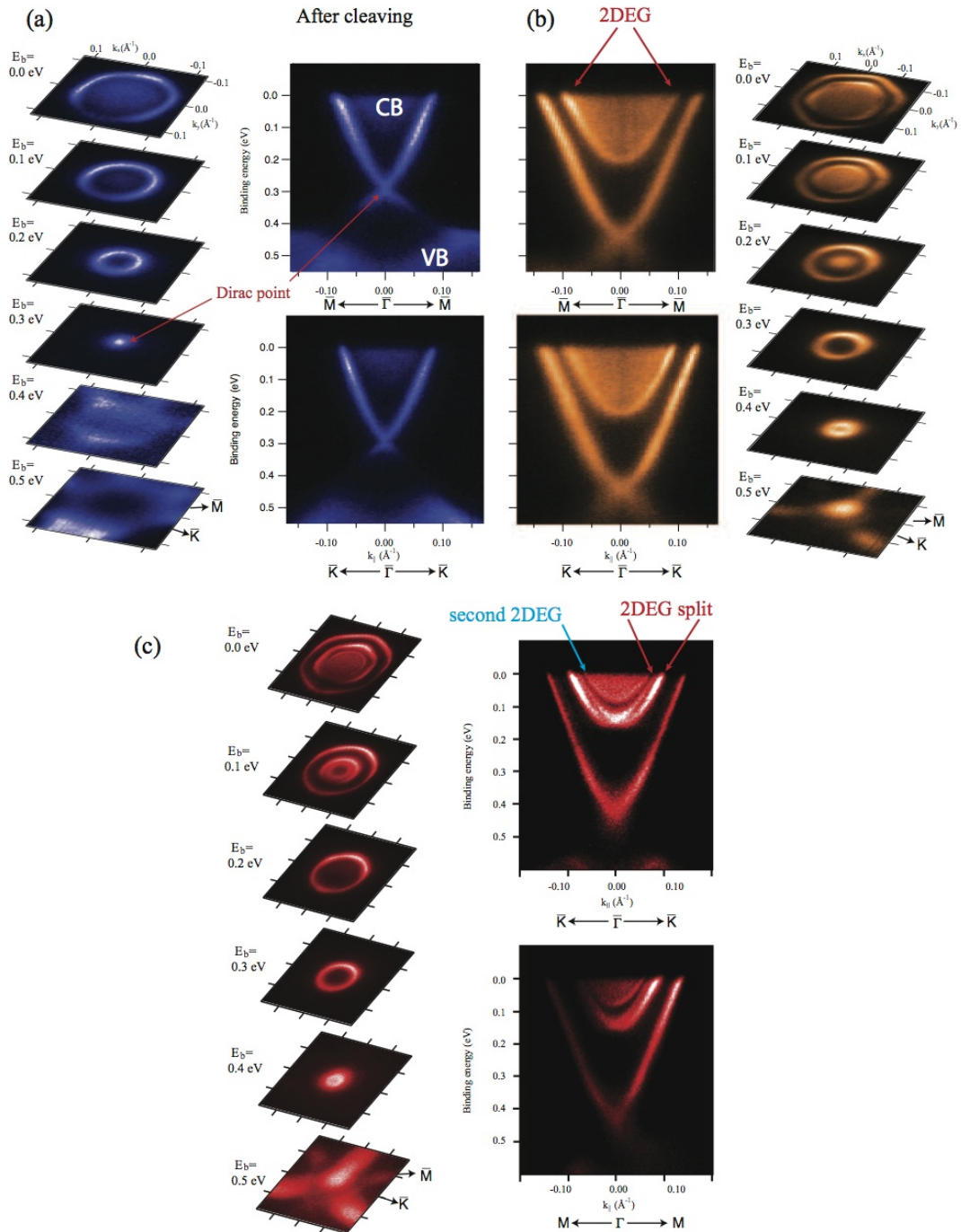


Figure 3.9: Time development of the surface states on  $\text{Bi}_2\text{Se}_3$  (generation II). (a) Electronic structure 20 min after cleaving and (b) 3 h after cleaving. (c) After  $\approx 20$  h the splitting of the 2DEG and a second 2DEG appear (gen V). Spectra have been taken with  $h\nu = 16$  eV.

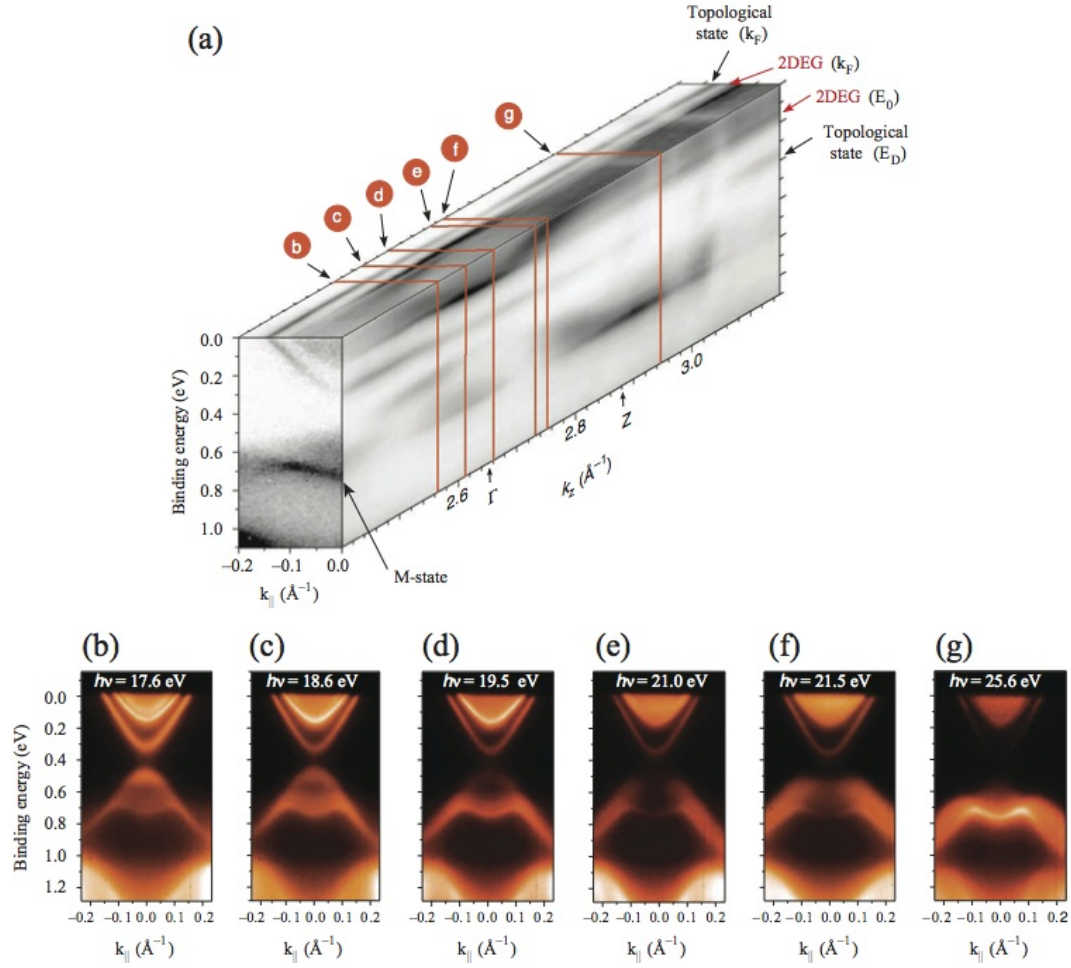


Figure 3.10: (a) Three-dimensional representation of the evolution of the electronic structure with  $k_z$ , determined from  $h\nu$  dependent ARPES measurements from 14 to 32 eV with steps of 0.1 eV, between 7 and 11 hours after cleaving (gen. II). The scan has been acquired after the one of Fig. 3.11 (b). Bulk  $\Gamma$  and  $Z$  high symmetry points are indicated. Selected cuts (marked b–g) are shown at the bottom, measured at  $h\nu =$  (b) 17.6, (c) 18.6, (d) 19.5, (e) 21.0, (f) 21.5, and (g) 25.6 eV.

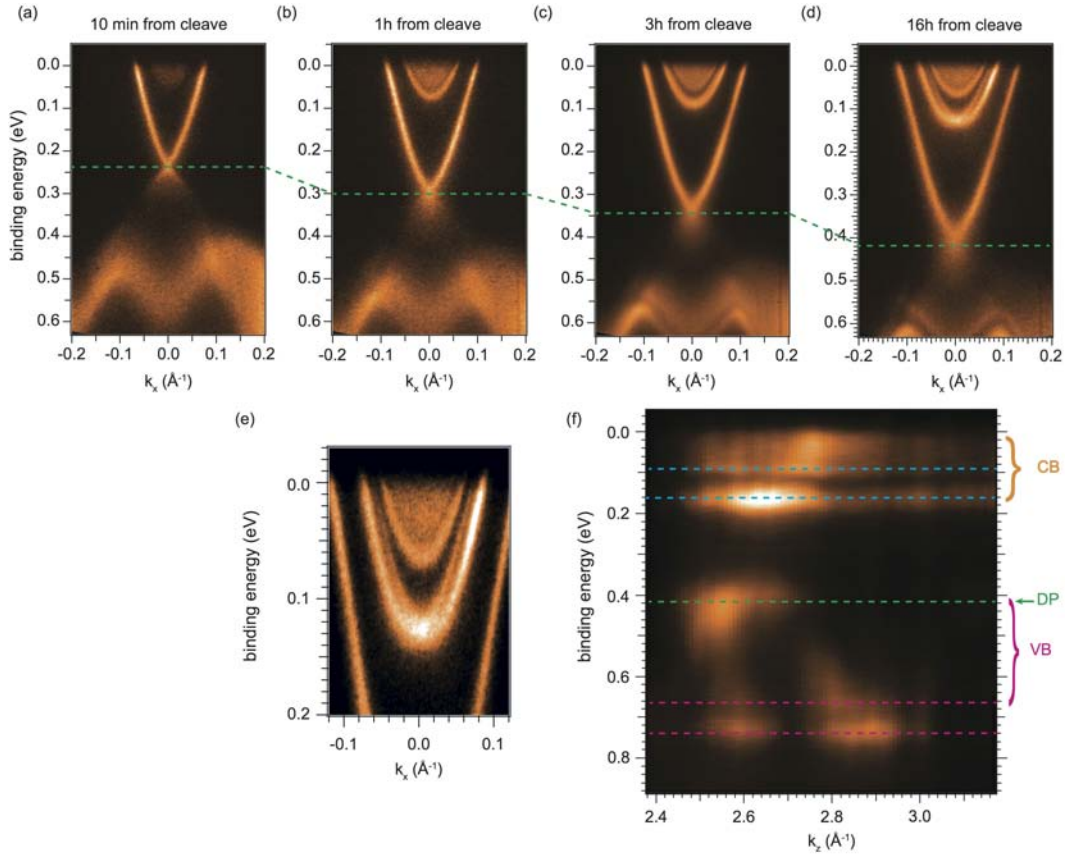


Figure 3.11: ARPES spectra acquired at (a) 10 min, (b) 1 h, (c) 3 h and (d) 16 h after cleave showing photoemission intensity as a function of binding energy and  $k_{\parallel}$  ( $h\nu = 16$  eV) for intrinsic  $\text{Bi}_2\text{Se}_3$  (generation V). Additional states in the CB are clearly visible. The band bending is indicated by the shift of the Dirac points towards higher binding energy. (e) Magnification of the Rashba-split QWS shown in (d). (f) Photoemission intensity at normal emission as a function of binding energy and  $k_z$  acquired with a photon energy scan. The data shown in (f) are a subset of a larger energy scan between  $h\nu = 14$  eV and  $h\nu = 32$  eV.

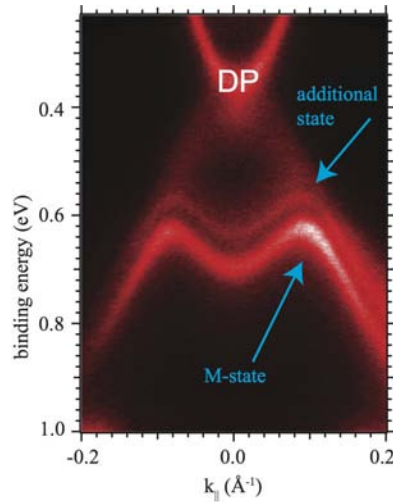


Figure 3.12: Detail of the scan acquired after the one from which Fig. 3.9(c) was obtained. The M-state and another m-shaped state appear simultaneously with the Rashba splitting of the 2DEG and the second 2DEG, 20 h after the cleave (gen. V). Spectra have been taken with  $h\nu = 19.2$  eV.

evident for higher band bending when the Fermi momentum ( $k_F$ ) of the TS becomes larger according to Ref. [82].

In Chap. 1.1.1 we have introduced the presence of a potential gradient at the surface, which can also be viewed as an electric field, and this has been shown to lead to the quantisation of the CB in various semiconductors (e.g. CdO [19]). Let us consider this for a moment, as the band bending (clearly indicated by the shift of the DP) shows the presence of such an electric field. This electric field could act as a quantum well, leading to the quantisation of states in the CB. Furthermore, increasing the depth (in our case the gradient) of the potential increases the number of bound states, roughly speaking. If we now remember that the Rashba term depends on the electric field at the surface, it is straightforward to conclude why the 2DEG does not appear split at the beginning, but that the Rashba-like splitting increases as soon as the band bending, and therefore the electric field, increases. This point will be addressed in more detail in the following section.

This model has been implemented thoroughly by solving a coupled Poisson-Schrödinger equation in Refs. [47, 85, 88], and here with a simpler Schottky model summarised in Fig. 3.13. This model consists of assuming a constant charge density  $\rho$  between the surface and a depth  $\Delta$  and then calculating the electrostatic potential via the Poisson equation<sup>8</sup>. The second step is to numerically solve the Schrödinger equation in this potential in order to obtain the allowed eigenstates and their energies. Therefore the model has two parameters:  $\rho$  and the width of the charge layer  $\Delta$  and they can be determined by two conditions. First the potential must reproduce the experimentally observed band bending, which can be inferred from the position of any sharp feature in the spectrum (e.g. the topological surface state

<sup>8</sup>The dielectric constant for  $\text{Bi}_2\text{Se}_3$  is not well known, but values between 100 and 70 are often quoted. Calculation using the values 110 and 70 have been performed that leads to small differences that are on the borderline of what we can resolve experimentally.

at off-normal emission where it appears clearer). Secondly, the solution of the Schrödinger equation must also reproduce the number and approximate energies of the observed occupied QWS. Note that this solution also yields the envelope wavefunctions as shown in Fig. 1.2(d). The Bloch character of the states is taken into account by using the correct effective mass of the electrons in the  $z$ -direction, here set to  $0.24m_0$  [85]. It will be shown how this model

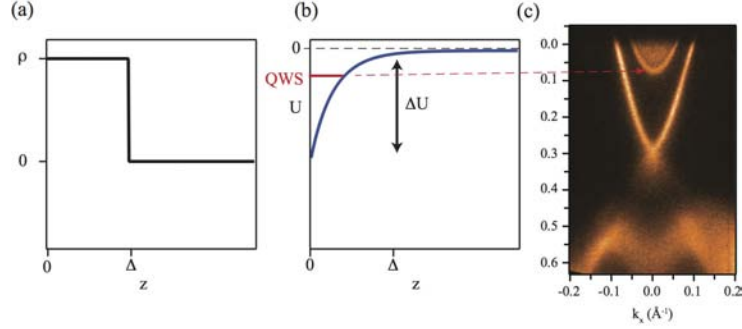


Figure 3.13: Example of how the Schottky model is applied. We start by considering a constant density of charge at the surface (a) and using the Poisson equation calculate the related electrostatic potential (b). Solving the Schrödinger equation, the allowed eigenvalues (red line) can be found. The parameters can be changed so as to reproduce the observed additional state(s) indicated by the red dashed arrow. (c) ARPES spectra acquired 1h after cleave on a clean surface showing a single 2DEG.

is able to reproduce the observed 2DEG in the following sections, but before that, we shall present some preliminary discussion about the possible mechanisms that could lead to such an ageing effect.

**Surface reconstruction:** This is known to be a possible cause of the emergence of new states (in our case the 2DEG or the M-state) or more generally of a change in the surface potential that may cause band-bending. LEED measurements (data not shown) do not show any evidence of reconstruction occurring over time (the  $1 \times 1$  pattern remains unchanged with time at different energies). A high  $h\nu$  map of the Fermi surface that encompasses the  $\bar{\Gamma}$  points in two nearest neighbour surface Brillouin zones does not show any (exotic) in-plane relaxation either (Fig. 3.14). No indication of surface reconstruction has been indicated in STM measurements to our knowledge [89].

**Surface relaxation:** In Ref. [90] (for the similar case of  $\text{Bi}_2\text{Te}_3$ ) and then in Refs. [79, 91] the band bending is attributed to a surface relaxation of the van der Waals gap. In these it is argued that this happens after cleaving and leads to an increase in the distance between the last quintuple layers. Recent theoretical calculations that simulate a relaxation of about 40% in the quintuple layer distance seem to support this hypothesis and also explain the appearance of the unexpected M-state [92]. However, such a relaxation is expected to take place spontaneously on the typical time-scale of a phonon, and not in 2–20 hours. This means that if this expansion is taking place, it has to be the consequence of another process. LEED I-V measurements<sup>9</sup> could possibly resolve whether this is the case. Interpretation of such data is however limited by the

<sup>9</sup>The LEED I-V technique exploits the modulation of the LEED spots' intensity (I) as

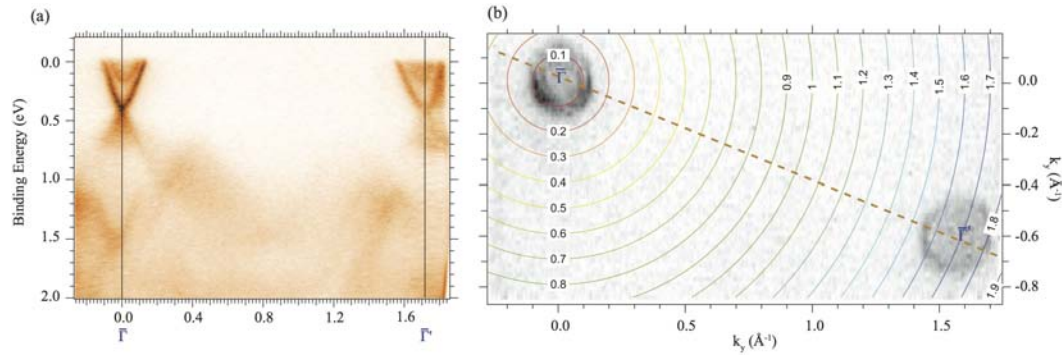


Figure 3.14: (a) Surface electronic structure between two nearest  $\bar{\Gamma}$  points in  $\text{Bi}_2\text{Se}_3$  acquired at  $h\nu = 70$  eV. The energy dispersion data is taken along the orange dashed line in (b) showing the wide  $k$ -range Fermi surface map.

complexity of the simulations needed to understand the surface structure. These are made even more difficult by the complexity of the  $\text{Bi}_2\text{Se}_3$  layered crystal, and because the relaxation is so far from the surface. Nevertheless, such a study has recently been published in Ref. [93] where a contraction of  $\approx 1\%$  is observed for the topmost quintuple layer in  $\text{Bi}_2\text{Te}_3$  once a bilayer of Bi is deposited on it. Surface sensitive X-ray diffraction (i.e. at grazing angle) may also indicate if a significant relaxation takes place.

**Migration of defects:** A common problem concerning the growth technique is segregation of Se at the edges of the as-grown crystal<sup>10</sup>. This evidence indicates the possibility of defect migration (Se or Bi or vacancies) that might gather at the surface, causing an increased density of defects or an increase in the last quintuple layers' separation, possibly causing the band bending. STM measurements presented in the following parts do not clearly show an increasing surface density of defects with time [94], and chemical identification of the defects seen in STM is open to interpretation. On the other hand, the observed broadening of the TS with time in the energy window away from the CB and the Dirac point (see Fig. 3.32 (d)) may indicate a diminished lifetime of the photo-hole, possibly caused by increased defect scattering<sup>11</sup>. Time resolved X-ray photoemission spectroscopy measurements could give indications if this is the case.

**Contaminant Adsorption:** The fact that all the measurements have been performed in UHV does not imply that the sample is totally contaminant free, especially when the sample lies at low temperature (60 K) for long periods. Even in UHV conditions

---

a function of the incident electron beam energy (V). Comparing the intensity curves with theoretically calculated ones for an assumed structure allows a quantitative determination of the real structure.

<sup>10</sup>This effect is even optically visible in the quality and size of the samples that are cleaved from the edges of the original crystal.

<sup>11</sup>Even though the topological state is protected from back scattering by its spin texture, intra-band scattering is still allowed from states that are nearby the photo-hole with similar spin direction. This is a point that will be discussed in the following chapters.

the physisorption of  $\text{H}_2\text{O}$  and other residual gases ( $\text{CO}$ ,  $\text{CO}_2$ ) takes place. An early indication of the importance of this effect in the aforementioned drift is the fact that it appears more pronounced at low temperatures and at higher background pressures. Furthermore this could be a reasonable source of band bending that occurs on such a long time scale<sup>12</sup>. Rest gas adsorption can induce a change of the chemical potential, and it can also explain the increase of the TS width with time, as each molecule can act as a scattering centre. Even though an element and surface sensitive technique was not available on the beamline at the time of the experiments, a test has been done to clarify the importance of this effect by exploiting the known desorption of some residual impurities at room temperature (see Fig. 3.15). This already shows the tuneability of the band bending and of the Rashba splitting. The latter being fundamental, for example, for the realisation of a Datta-Das transistor [95, 96].<sup>13</sup> After the appearance of the Rashba splitting of the 2DEG

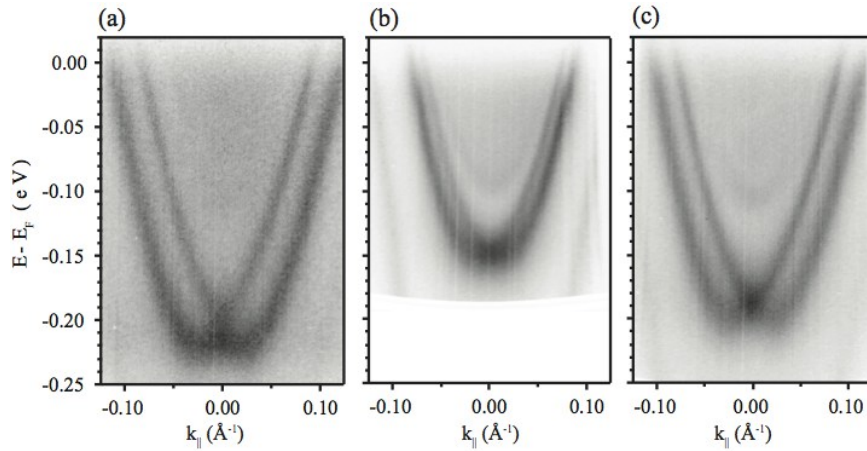


Figure 3.15: A smaller band bending with a reversible nature can be seen on top of the overall downward band bending (gen. V). Here are presented high resolution data acquired with  $h\nu=19.2$  eV showing the behaviour under annealing of the 2DEG. (a) Strong Rashba splitting ( $\Delta k_F = 0.034 \text{ \AA}^{-1}$  where  $\Delta k_F$  is the momentum difference between the bottom of the two split states). (b) Large reduction in 2DEG binding energy and Rashba splitting ( $\Delta k_F = 0.011 \text{ \AA}^{-1}$ ) caused by annealing the sample at 250 K (removal of some surface adsorbates). (c) With further time after going back to low temperature, the full band bending appears to be recovered, leading to a lower band bottom and larger Rashba splitting ( $\Delta k_F = 0.025 \text{ \AA}^{-1}$ ).

(DP at 0.28 eV from  $E_F$ ) the sample was annealed (from low temperature) to nearly room temperature (250 K) and kept there for 20 min. Just after reaching 250 K the sample seems to recover the situation where the 2DEG is evident but a reduced Rashba

<sup>12</sup>Even though this can happen, one should point out that in the most common systems, such as pure metals and semimetals, physisorption leads to a degradation of the surface related features in terms of life-time and signal to background ratio.

<sup>13</sup>A Datta-Das Spin-Field-Effect-Transistor (SFET) that is able to manipulate the electron spin without the use of external magnetic fields has been a hot topic in recent decades, in the search for future spintronic devices.

splitting is detectable (and DP at 0.11 eV from  $E_F$ ), but no further change in the spectral signature has been noticed during that period. Cooling the same sample back to low temperature, no spectral change is observed in respect to the room temperature measurement (apart from an overall decrease in the width of the states). Keeping the same sample at low temperature for further time, the situation is recovered where the 2DEG split is more evident (DP at 0.26 eV from  $E_F$ ). The latter experiment not only points out the possibility of tuning the Rashba splitting of the 2DEG, but also the importance of contaminant adsorption in the band bending process.

### 3.2.4 Confinement of valence band states

Marco Bianchi<sup>1</sup>, Dandan Guan<sup>1,2</sup>, Richard C. Hatch<sup>1</sup>, Shining Bao<sup>2</sup>, Jianli Mi<sup>6</sup>, Bo Brummerstedt Iversen<sup>6</sup>, and Philip Hofmann<sup>1</sup>

Contribution: experimental design, strategy and execution, sample preparation, acquisition, analysis.

Reference Papers: *Simultaneous quantization of bulk conduction and valence states through adsorption of nonmagnetic impurities on  $Bi_2Se_3$* , R. C. Hatch, *et al.* **Phys. Rev. Lett.** **107**, 086802 (2011).

*The electronic structure of clean and adsorbate-covered  $Bi_2Se_3$ : an angle-resolved photoemission study*, M. Bianchi, *et al.* **Semicond. Sci. Technol.** **27** 124001(2012).

A more careful test can be performed to check the importance of contaminant adsorption, and this will also verify the aforementioned Schottky model. This consists of monitoring the states while intentionally dosing a known gas species. Spectra have therefore been acquired while dosing a partial pressure of  $8 \times 10^{-9}$  mbar of CO onto a Ca-doped sample that was kept at a temperature of 65 K. Acquisition was started 1 h after the cleave and, under these conditions, the development of the band bending appears accelerated and more pronounced than before. Figs. 3.16(a-c) show the dispersion at some selected exposure times. Also in this case the spectra shown are a subset of a larger dataset where images were acquired every 2 min at normal emission. Fig. 3.16(d) shows a cut through the centre of all images (i.e. the energy and time-dependent photoemission intensity at normal emission) and allows us to follow the continuous drift of the DP until saturation. Contrary to Fig. 3.11, here the CB bulk related features are not visible due to the fact that as starting point the sample was in the insulating state thanks to the Ca-doping. As the CO coverage increases, not only does the DP shift, indicating the band bending, but also near the Fermi level a first 2DEG develops after  $\approx 20$  min (blue dashed line) and after  $\approx 100$  min a second one appears. The Rashba splitting of the first 2DEG (the one at higher binding energies) becomes considerable and also the second one appears split.

A closer look at the VB region reveals the development of additional M-shaped states, similar to the surface state observed just after cleave. These lie where the DP ends in the saturated condition and all fall in the projected VB.

The Fermi surface map acquired once saturation was reached is presented in Fig. 3.17. Here it is clear that both the 2DEGs and the TS undergo a similar hexagonal warping that decreases as the distance from  $\bar{\Gamma}$  diminishes.

The photon energy scan shown in Fig. 3.18 reveals the 2D character of all these additional states: 2DEGs, M-state and additional M-shaped states. Here (Fig. 3.18 (b-d)) it is also possible to better appreciate the energy dispersion of the aforementioned M-shaped states at selected photon energies where their intensity is resonantly enhanced.

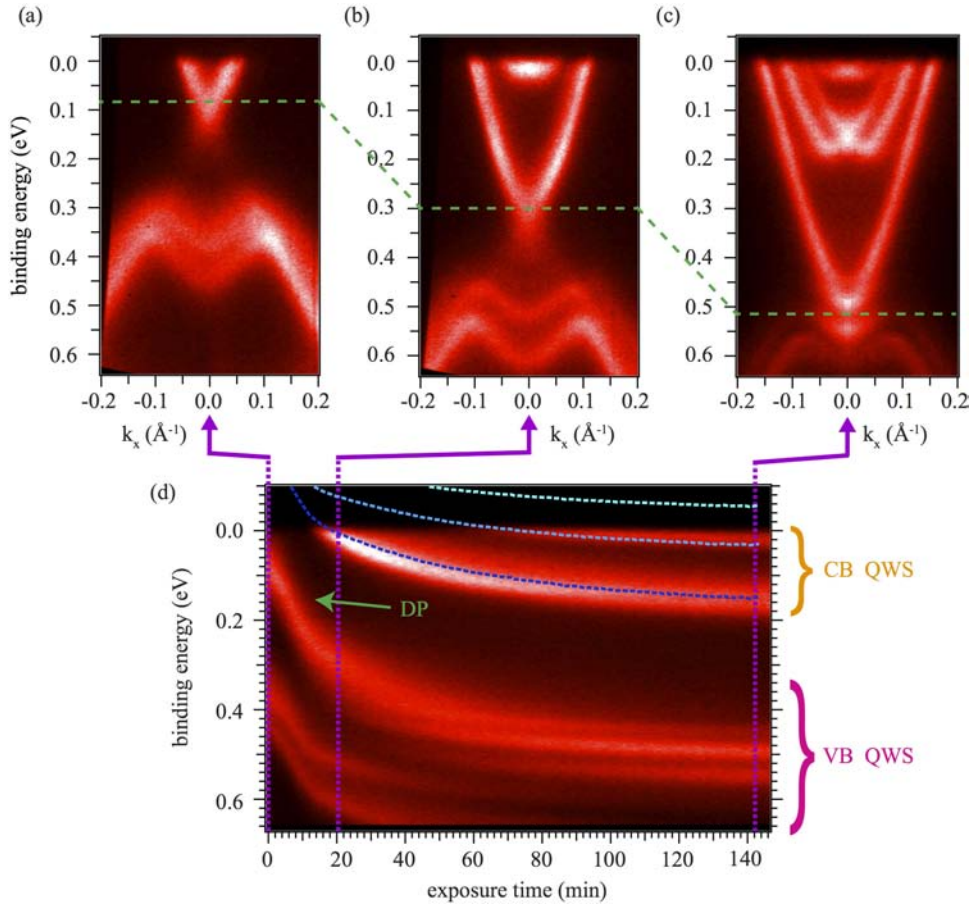


Figure 3.16: ARPES spectra acquired during the controlled dosing of CO on Ca-doped  $\text{Bi}_2\text{Se}_3$  ( $h\nu = 16$  eV). The acquisition and dosing was started about 1 h after the cleave. (a-c) Photoemission intensity as a function of binding energy and  $k_{\parallel}$  at different exposure times. (d) Photoemission intensity at normal emission as a function of binding energy and exposure time. The states in the marked regions are the quantum well states (CB QWS and VB QWS). The Dirac point is indicated by the green arrow while the blue, azure and cyan dashed lines show the energies of the calculated QWS using the Schottky model.

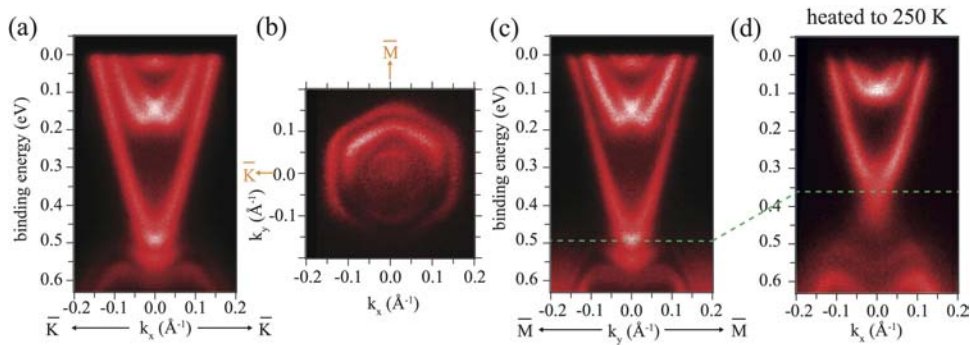


Figure 3.17: Dispersion and Fermi surface map after CO dosing ( $h\nu = 16$  eV) on Ca-doped samples. (a) and (c) Photoemission intensity as a function of binding energy and  $k_{\parallel}$  in the  $\bar{K}\bar{\Gamma}\bar{K}$  and  $\bar{M}\bar{\Gamma}\bar{M}$  directions, respectively. (b) Fermi surface map around  $\bar{\Gamma}$  showing the hexagonal warping of the QWS that diminishes as the distance from  $\bar{\Gamma}$  decreases. (d) Spectrum taken at 250 K after CO dosing showing the partial reversibility of the band bending.

We do not have an absolute quantitative measurement of the coverage but it can be expected to be of the order of one monolayer or less, as multilayers are not likely to be formed at this temperature and pressure (see for example Ref. [97]). Concerning the way the CO molecules are adsorbed, it can be fairly certainly stated that the molecules remain intact. CO is a very strongly bonded molecule (it has a triple-bond) and it is very hard to dissociate upon adsorption (a known problem in catalysis). This is only possible on reactive transition metal surfaces (see for example Ref. [98]) but seems implausible on this cleaved surface where all the bonds are saturated. Furthermore it appears, as suggested by Fig. 3.17 (d), that the CO molecules can be partially desorbed with a gentle anneal.

At the time when we were performing these measurements the group of C.R. Ast was studying the very same behaviour obtained by depositing  $H_2O$ . This work is now published in Ref. [99]. Here it is argued that a chemical reaction takes place at the surface. Such a reaction, consisting of Se abstraction from the very first layers, leaves positively charged vacancies that are the origin on the observed band bending. Also in this reference a similar interpretation for the origin of the 2DEGs is adopted but the energy locations of such states is derived using a triangular potential  $U(z)$  with a constant effective potential gradient  $\nabla U(z)$ . Even though in these two studies the origin of the 2DEGs is traced back to a band bending, such a chemical reaction is not expected to occur with CO.

In the light of these tests it is now appropriate to address again the discussion on the nature of these states. First of all it has to be noted that the appearance of the 2DEGs has nothing to do with the topology, as the number of Fermi level crossings remains odd. The 2DEGs from this point of view can be considered topologically trivial. It is also evident that the origin of the band-bending is the adsorption of impurities on the surface, but how does this happen? What is the principal mechanism? If we now apply the Schottky quantum well model described in Fig. 3.13, it will become clear that the presence not only of the 2DEGs and their Rashba splitting (discussed in the following section), but also the presence of the M-shaped states are closely related.

The resulting potential and the calculated quantum well states in the conduction band are given in Fig. 3.16(d), showing how even such a simple model already captures much of

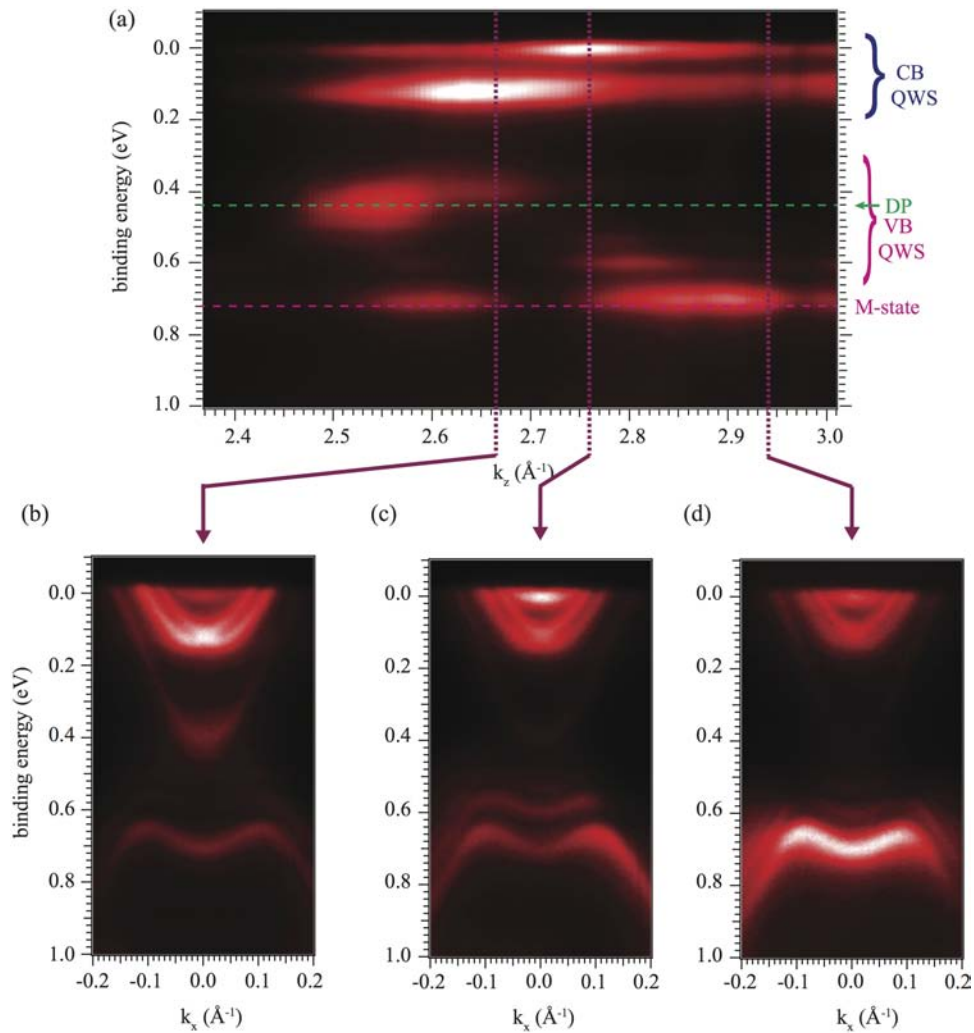


Figure 3.18: Photon energy scan after exposing the Ca-doped samples to carbon monoxide. (a) Photoemission intensity at normal emission as a function of binding energy and  $k_z$ . (b–d) Photoemission intensity at selected  $k_z$  values depicting the energy dispersion relation.

the form of the trend. The degree of band bending is again determined by requiring the model to reproduce the number and approximate binding energies of the QWS that are in fact observed. It is the right time now to discuss this a bit more.

Note that the VB is not exempt from this drift near the surface and, in order to be consistent, it should be bent towards higher binding energies too, see Fig. 3.19(a-c). What has to be borne in mind is the particular bulk electronic structure of  $\text{Bi}_2\text{Se}_3$ . This is not only peculiar for hosting the TS, but it is also characterised by having a rather narrow projection into the 111 surface at the  $\bar{\Gamma}$  point (Fig. 3.19(c)). Here the VB width is, in fact,  $\approx 200$  meV, leading to a quite unusual situation where the states can be quantised “inside” the VB, if the bending is able to overcome this width<sup>14</sup>. If this was not the case, as shown in the situation of Fig. 3.19(b), the states would simply be degenerate with the bulk states. Looking back now to Fig. 3.16, it is clear why the additional M-shaped states become more pronounced once the DP, and so the band bending, reach a value  $\gtrsim 250$  meV, though the lowest quantum well states can already be confined for a smaller band bending. This simple interpretation, that will be discussed again further on together with the Rashba-split, has also been supported by recent calculation in Ref. [102].

This discussion however raises concerns about the interpretation of the original M-state as a surface state, as so far it has been. Its origin as a quantum well state (QWS) of the VB can not be ruled out.

It is very interesting to compare these results to those obtained by the adsorption of Fe on the surface of Ca-doped  $\text{Bi}_2\text{Se}_3$  [103], a case that will be also discussed in a following chapter. The similarities are striking. In Ref. [103] very similar Rashba-split quantum well states are observed in the CB region which are interpreted as additional surface states. The VB shows a series of M-shaped features, very similar to those reported here. These M-shaped features are, however, not interpreted in the same way but rather in terms of a gap opening at the DP. In view of the present discussion, it appears that there is very little difference between nonmagnetic and magnetic impurities in these two cases, and both lead to doping and strong band bending. Note, however, that adsorbed Fe atoms are not necessarily magnetic in the first place. It would have to be confirmed that the Fe adatoms retain a significant magnetic moment after adsorption, and a band gap opening at the DP would be expected only for an ordering of the moments perpendicular to the surface [104]. It is however true that the presence of these states hides the dynamics near the Dirac point, and their intensity and shape can mislead the observer.

It has to be addressed that this discussion does not exclude *a priori* an eventual relaxation of the surface, that is, on the contrary, likely to happen, as in the majority of systems, after the adsorption or intercalation of foreign species. It is unlikely that the dominant effect is the expansion of the van der Waals gap near the surface, as suggested in Ref. [92], because this would need such a drastic change (40% of expansion) in order to reproduce the observed effect. The following experiments will also support this, but it can be mentioned that, for example, the incorporation of substantial amounts of copper<sup>15</sup> into bulk  $\text{Bi}_2\text{Se}_3$ , experimentally, leads to a change of the van der Waals gap of only 3% [105].

We have also performed similar experiments to the one presented here involving other species. However, the results are either not interesting at this time (i.e. no appreciable change to the aforementioned time dependence in UHV was observed dosing Ne, Xe,  $\text{H}_2$ ,  $\text{CO}_2$ ) or inconclusive (e.g.  $\text{F}_3\text{CCl}$ ) and need further and careful investigation.

<sup>14</sup>A similar effect was also seen in the pioneering works on 3D semiconductors [100, 101].

<sup>15</sup>The element ratio was in this case  $\text{Cu}_{0.12}\text{Bi}_2\text{Se}_3$ .

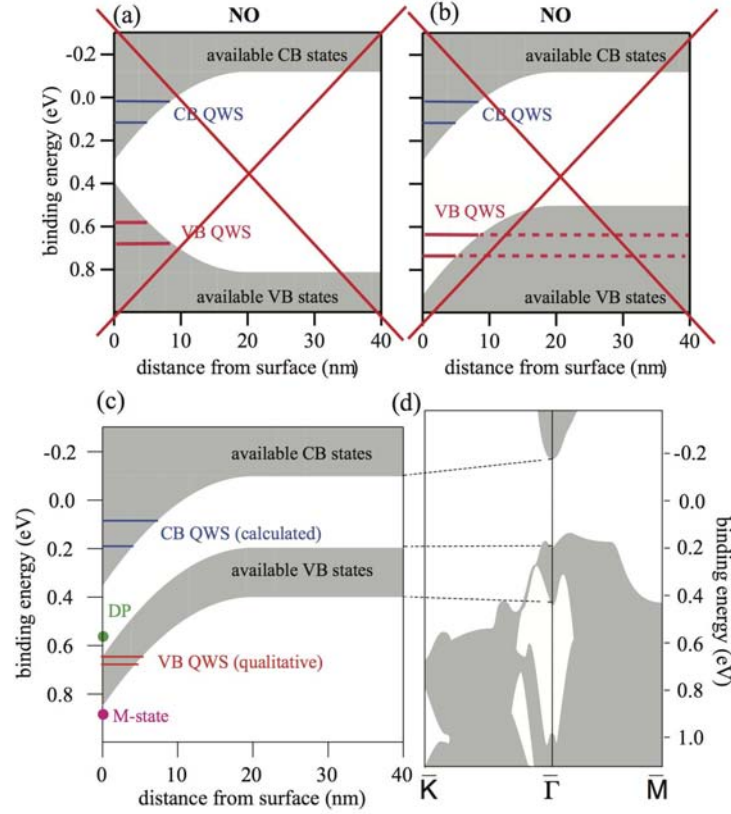


Figure 3.19: (a)-(d) Physical and unphysical models for the quantum confinement of the CB and VB states. (a) Unphysical situation where the CB and the VB experience at the same time two opposite band bendings. (b) A more physical situation where both the CB and VB are shifted consistently, that however does not permit the formation of quantised states (in the VB), as they will be degenerate with the bulk ones. (c-d) Semi-quantitative model for the quantum confinement of the CB and VB states. The band bending corresponds to the value for the full coverage in Fig. 3.16. The width  $\Delta$  of the space charge layer has been estimated by requiring the presence of two calculated and occupied quantum well states in the CB with similar binding energies as observed experimentally, used also for Fig. 3.16 (d). The position of the quantum-confined states in the VB is merely a qualitative sketch. (d) Projected band structure of Bi<sub>2</sub>Se<sub>3</sub> adapted from Ref. [51], illustrating that the upper part of the VB is quite narrow (around 200 meV), such that all the VB states can be confined for a band bending exceeding this value.

### 3.2.5 Rashba splitting of the conduction band 2DEG

P. D.C. King<sup>7</sup>, R. C. Hatch<sup>1</sup>, M. Bianchi<sup>1</sup>, R. Ovsyannikov<sup>16</sup>, C. Lupulescu<sup>17</sup>, G. Landolt<sup>18,19</sup>, B. Slomski<sup>18,19</sup>, J. H. Dil<sup>18,19</sup>, D. Guan<sup>1,2</sup>, J. Mi<sup>6</sup>, E. D. L. Rienks<sup>16</sup>, J. Fink<sup>16,20</sup>, A. Lindblad<sup>21</sup>, S. Svensson<sup>21,22</sup>, S. Bao<sup>2</sup>, G. Balakrishnan<sup>23</sup>, B. B. Iversen<sup>6</sup>, J. Osterwalder<sup>18</sup>, W. Eberhardt<sup>16,17</sup>, F. Baumberger<sup>7</sup>, and Ph. Hofmann<sup>1</sup>

Contribution: acquisition on SGM3 at ASTRID and minor part on SGM1 and analysis.  
Reference Paper: *Large tuneable Rashba spin splitting of a two-dimensional electron gas in  $Bi_2Se_3$* , P. D. C. King, *et al.* **Phys. Rev. Lett.** **107**, 096802 (2011).

Now that the interpretation of the additional 2D states has been discussed, it is worthwhile to address more thoroughly the splitting of the 2DEG in a Rashba manner, as this has been introduced up to now only as a speculation, albeit one well supported by our ARPES measurements.

Therefore, to do so, first we need to confirm the spin-split nature of the 2DEG. This is shown in Fig. 3.20 where spin-resolved ARPES data acquired using the COPHEE setup at the Swiss Light Source described in Ref. [106] are summarised. The detailed analysis of such data is beyond the scope of this work and has been performed by our collaborators at the Swiss Light Source. However, for reasons of clarity, it will be briefly described here to the extent required to make these data understandable.

The spin polarisation of the states crossing  $E_F$  along the  $\bar{M}\bar{\Gamma}\bar{M}$  direction was extracted using a well established two-step fitting procedure described in Ref. [107]. The fit of the total MDC intensity was performed using 7 components in order to describe the following, moving radially away from  $\bar{\Gamma}$ : 1 component for the CB (and eventually the unresolved second 2DEG, inner grey peak), 2 components for the inner ring coming from the split 2DEG (black lines), 2 components for the outer ring coming from the split 2DEG (black lines) and finally 2 components for the topological state (outer grey lines). This analysis shows that both the topological and the spin-split 2DEG states are spin polarised, as summarised in Fig. 3.20(b). The former has already been described in the previous sections and in the cited literature due to the topological nature of the state. The spin texture of the 2DEG instead appears to be that of a simple Rashba model. The spins lie predominantly in-plane and, averaging over the Kramers pair, are situated mostly orthogonally to the state's momentum, as shown in Chap. 1.1.2. Deviations from a perfect spin helicity are however expected due to small misalignments in the sample position. Furthermore, a detailed analysis will likely reveal the effects of the visible hexagonal warping experienced also by the topological state.

Now that the spin-polarisation of these states has been shown, it is worthwhile to discuss in more detail how the ageing in UHV affects the splitting. This has been investigated by our

<sup>16</sup>Helmholtz-Zentrum Berlin, Elektronenspeicherring BESSY II, D-12489 Berlin, Germany.

<sup>17</sup>D. Technische Universität Berlin, Strasse des 17. Juni 135, D-10623 Berlin, Germany.

<sup>18</sup>Physik-Institut, Winterthurerstr. 190, Universität Zürich-Irchel, 8057 Zürich, Switzerland.

<sup>19</sup>Swiss Light Source, Paul Scherrer Institut, CH-5232 Villigen, Switzerland.

<sup>20</sup>Leibniz-Institute for Solid State and Materials Research Dresden, P.O. Box 270116, D-01171 Dresden, Germany.

<sup>21</sup>MAX-lab, Lund University, P.O. Box 118, SE-22100 Lund, Sweden.

<sup>22</sup>Department of Physics and Astronomy, Uppsala University, P.O. Box 521, SE-75121 Uppsala, Sweden.

<sup>23</sup>Department of Physics, University of Warwick, Coventry CV4 7AL, United Kingdom.

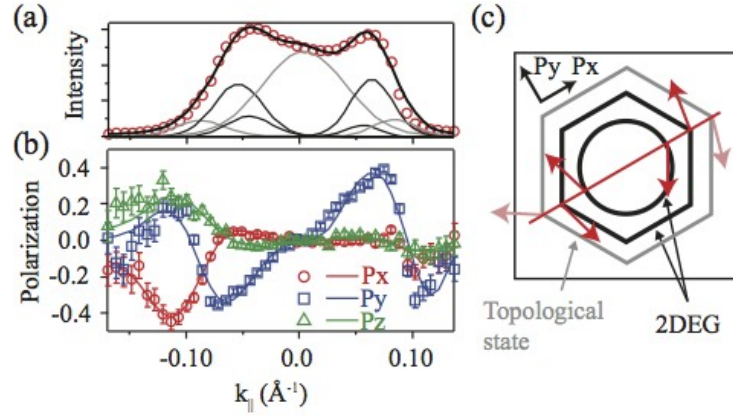


Figure 3.20: Spin resolved ARPES results at  $E_F$  (gen. V). (a) MDC at the Fermi level along the  $\bar{M}\bar{\Gamma}\bar{M}$  direction. The photon energy used is  $h\nu = 19.5$  eV and the sample temperature 60 K. Circles represent the measured intensity while solid black lines show the fit result using 7 components: 2 components for the topological state (grey lines), 4 components for the split 2DEG (black lines) and 1 for taking into account the CB (grey line at the centre). (b) Measured (points) and fitted (lines) radial ( $P_x$ ), tangential ( $P_y$ ), and out of plane ( $P_z$ ) components of the spin polarisation along this cut. (c) Schematic representation of the in plane component of the Fermi surface spin texture (red arrows).

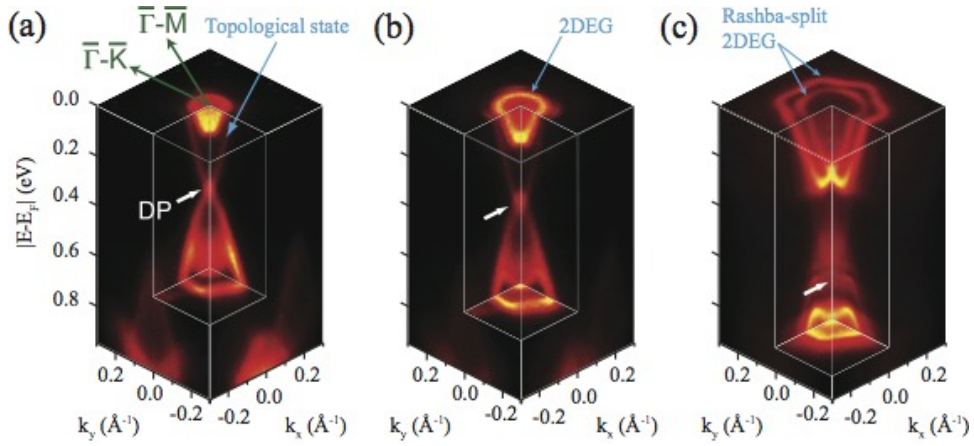


Figure 3.21: (a-c) ARPES data acquired with the VG Scienta ArTOF 10k at BESSY II using  $h\nu = 19.5$  eV with increasing time from cleaving (refer to Fig.3.22(a)). The sample was kept at 10 K (gen. V).

collaborators at BESSY II using a VG Scienta ArTOF 10k spectrometer [108]. This particular analyser is of cylindrical type and works by measuring the time of flight (TOF) of the photoemitted electrons in order to get their velocity and therefore their kinetic energy. Such a measurement needs a chopped light source to provide the time reference for the measurement; for this reason the storage ring was operating in single bunch mode (repetition rate of 1.25 MHz). The power of such an analyser is that, using a 2D delay line detector, it is able to measure a wide solid angle (a dense grid of points both in  $\theta$  and in  $\phi$ ) instead of a slice as done in the SPECS Phoibos 150 (see Chap. 2.3.1). This means that, at the same time, all the information ( $E_{\text{kin}}; \theta, \phi$ ) of a certain range of energies and angles can be obtained (see Fig. 2.5). Broadly speaking, a single shot allows us to build one of the 3D datasets shown in Fig. 3.21. Here only three points at representative times from the cleave are shown, that are selected from a bigger data set. Therefore this allowed us to follow in real time the ageing effect in all the directions of the SBZ, in particular along the  $\bar{\Gamma}\bar{M}$  and  $\bar{\Gamma}\bar{K}$  as shown in Fig. 3.22. The ageing effect occurs in a manner consistent with the previously shown results. As before, from these data it is possible to extrapolate the saturating behaviour of the band bending that causes the 2DEG, indicated by  $\Delta U$  (green points) in Fig. 3.22(b). The evolution of the Fermi momentum ( $k_F$ ), i.e. the momentum where the 2DEG crosses  $E_F$ , can also be obtained.

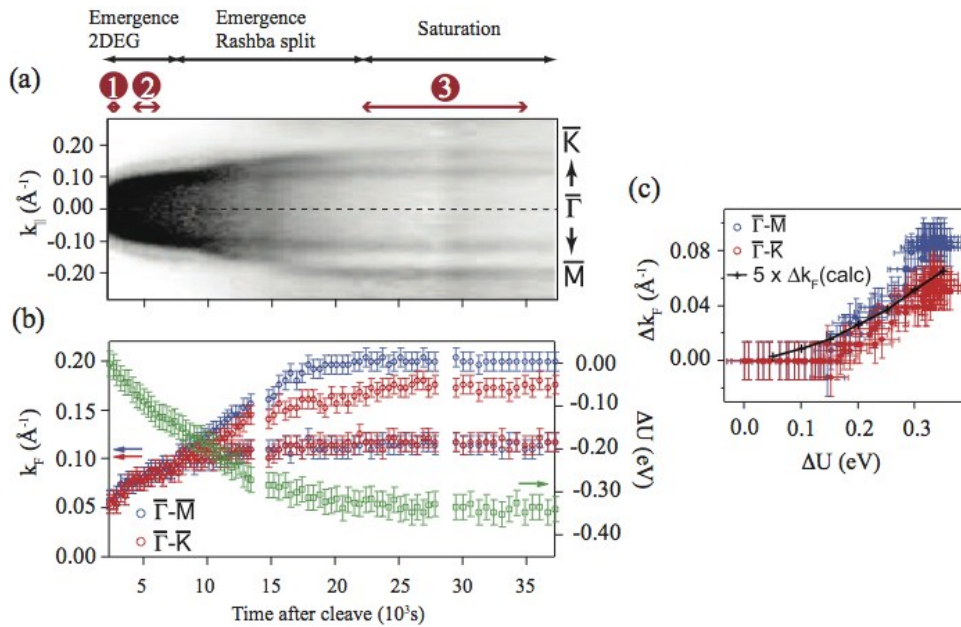


Figure 3.22: Information extracted from the dataset used also for Fig. 3.21. (a) Evolution with time from cleave of the Fermi wave vector along the two directions  $\bar{\Gamma}\bar{M}$  and  $\bar{\Gamma}\bar{K}$ . The red arrows and red encircled numbers (1,2,3) indicate the time ranges of Figs. 3.21(a),(b) and (c) respectively. (b) Extracted  $k_F$  positions and band-bending ( $\Delta U$ ) which induces the 2DEG. (c)  $k_{\parallel}$  splitting at the Fermi level of the measured (points) and calculated (lines) 2DEG as a function of the effective gate potential  $\Delta U$ .

Again our simple Schottky model can be applied, even in the more sophisticated way described in Ref. [47], giving quite good agreement with the experimental data as shown in

the previous case of Fig. 3.16. What turns out, as briefly mentioned above, is that the lowest lying 2DEG, located nearer to the surface (in this case approximately between 10 and 50 Å from the surface) where the surface potential  $U(z)$  is stronger, will also be the one showing a larger splitting. Note also that here the potential is acting as a real gating voltage.

In order to describe the Rashba-split, however, we need to introduce an additional simple model. For reasons of completeness, even though it is again beyond the experimental cut of this work and has been implemented by our collaborators, it will briefly be addressed. This model is typically used for III-V semiconductor quantum wells [109, 110], and therefore we have to keep in mind that they have quite a different band structure and much weaker spin-orbit interaction (SOI) than in our case. This model considers a Rashba parameter ( $\alpha$  in eq. 1.6) proportional to

$$\left\langle \psi(z) \left| \frac{d}{dz} \left[ \frac{1}{\epsilon'(z)} - \frac{1}{\epsilon'(z) - \Delta} \right] \right| \psi(z) \right\rangle. \quad (3.1)$$

Here  $\psi(z)$  is the eigenstate resulting from the Schottky model,  $\epsilon'(z) = \epsilon + U(z) + E_g$ , where  $\epsilon$  is the 2DEG energy relative to the CB,  $U(z)$  is the potential inducing the band bending and  $E_g$  is the band gap.  $\Delta$  represents a measure of the spin-orbit coupling within a  $\mathbf{k} \cdot \mathbf{p}$  approach as described by Kane in Ref. [111]. All these parameters are obtained from the Schottky model and from the literature, while for the SOI we can use a representative value of  $\Delta = 1$  eV. What turns out is that these calculations underestimate the splitting between different 2DEGs (subbands) by a factor of 4–5 for the first 2DEG. However it has to be noted how such a simple model is already able to describe the right trend of the splitting.

More sophisticated calculations have been published recently in Ref. [102]. These do not underestimate the splitting and further support our interpretation as the leading factor for the ageing effect, over the others discussed in Chap. 3.2.3 like van der Waals gap expansion, that though surely occurring, will play a marginal role.

However, the possibility of having a gating voltage on the surface, able to quantise states in the CB and furthermore to split them in a Rashba manner thanks to the SOI, had provoked our curiosity in investigating the band bending process even further with another experiment.

### 3.2.6 Surface doping via alkali deposition

M. Bianchi<sup>1</sup>, R. C. Hatch<sup>1</sup>, Z. Li<sup>1</sup>, Ph. Hofmann<sup>1</sup>, F. Song<sup>24</sup>, J. Mi<sup>6</sup>, B. B. Iversen<sup>6</sup>, Z. M. A. El-Fattah<sup>25</sup>, P. Löptien<sup>27</sup>, L. Zhou<sup>27</sup>, A. Khajetoorians<sup>27</sup>, J. Wiebe<sup>27</sup>, R. Wiesendanger<sup>27</sup>, and J. W. Wells<sup>26</sup>

Contribution: experimental design, strategy and execution, sample preparation, acquisition, minor analysis on ARPES data.

Reference paper: *Robust surface doping of  $Bi_2Se_3$  by Rb intercalation*, M. Bianchi, *et al.* **ACS Nano**. **8**, 7009-15 (2012).

Alkali deposition, in particular Rb, has been used in order to exploit the n-doping effect it has on the surface. This method is used in various systems, for example using K on graphene grown on different substrates (e.g. in Refs. [112, 113]).

Furthermore this opens the possibility of discerning the importance of the van der Waals gap expansion. This is because another process that can occur at surfaces is intercalation and, considering the Bohr radius of Rb ( $\approx 2.64 \text{ \AA}$ ), this can in principle lead to a considerable relaxation of the interlayer distance. So far a similar intercalation process from surface adsorbates has been reported only for the case of Ag on  $Bi_2Se_3$  [114], where this is observed at room temperature. Also in that case, the Ag adsorption leads to a shift of the entire electronic structure to higher binding energies and to the appearance of additional 2DEGs. This, however, is not interpreted as band bending but ascribed to an increased spacing of the van der Waals gap, caused by the intercalation of Ag. Indeed, first principles calculations mentioned before can bring about features similar to the experimental ones, but only if an increase of the van der Waals gap by 40% is assumed.

In the case of Rb, depending on its interaction with the substrate, it is likely that the adsorption also renders the surface much more reactive, due to the getter properties of the alkali.

This experiment was started originally on the SGM 3 beamline, but then further necessary investigations have been performed, mostly in the same conditions, using XPS at the SGM 1 beamline at ASTRID and STM by our collaborators, using always the very same preparation. For this reason we will start from the former.

Fig. 3.23 shows the electronic structure of the Ca-doped  $Bi_2Se_3$  after cleaving and upon the adsorption of a sub-monolayer coverage of Rb at 190 K within 20 min of cleaving. Exposure to Rb was performed *in situ*, using commercial SAES getter dispensers, and the surface coverage was determined by the relative intensity of Rb and substrate core level lines obtained by XPS measurement. The coverage is given in monolayers (ML), i.e. relative to the number of Se atoms in the first layer.

Initially the topological surface state with its characteristic Dirac cone is observed to be 50 meV below the Fermi level, resulting in a small circular Fermi surface. After Rb deposition, two Rashba-split 2DEGs can be observed similarly to the previously described cases, leading to a complex Fermi contour consisting of five concentric features: four from the 2DEGs and

<sup>24</sup>Zernike Institute of Advanced Materials, University of Groningen, 9747 AG, The Netherlands and Dept. of Physics, Norwegian University of Science and Technology (NTNU), Trondheim, Norway.

<sup>25</sup>Centro de Física de Materiales CSIC/UPV-EHU-Materials Physics Center and Donostia International Physics Center (DIPC), Manuel Lardizabal 5, 20018 San Sebastián, Spain.

<sup>26</sup>MAX IV laboratory, Lund University, Sweden and Dept. of Physics, Norwegian University of Science and Technology (NTNU), Trondheim, Norway.

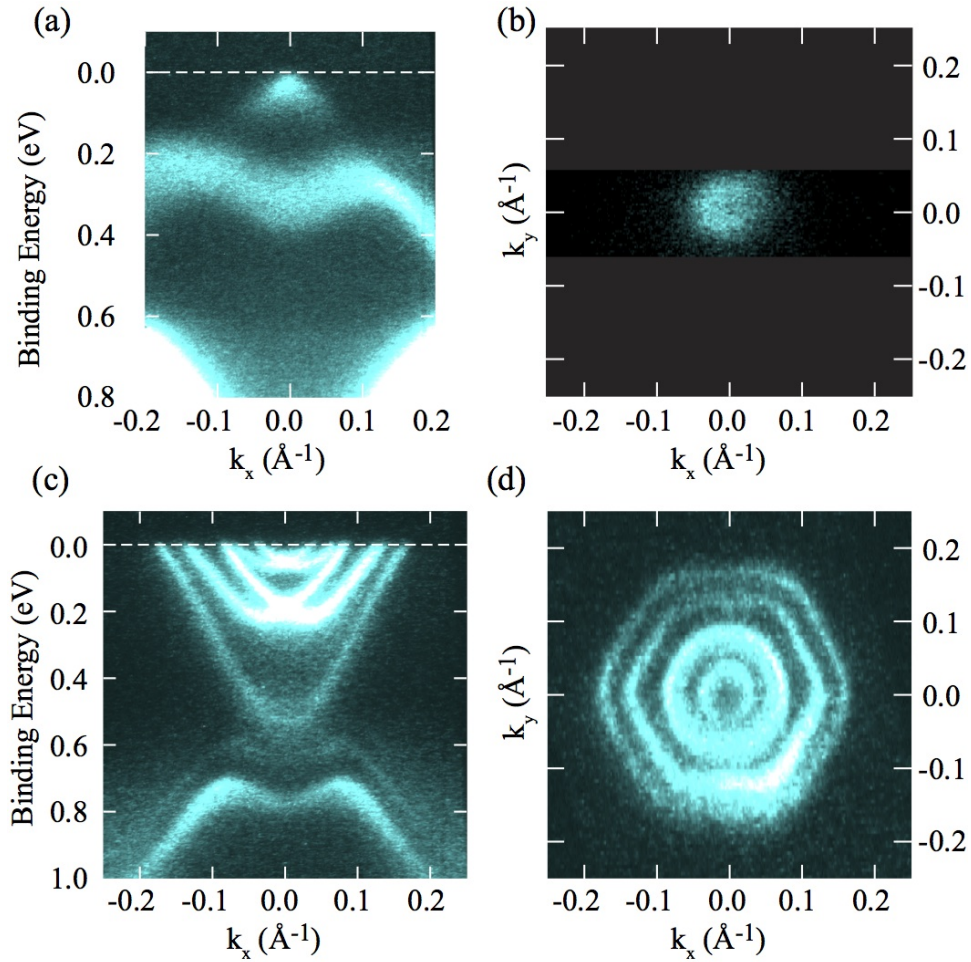


Figure 3.23: (a) ARPES measurement of the near-surface electronic structure of clean, calcium-doped  $\text{Bi}_2\text{Se}_3$  through the Brillouin zone centre and (b) the photoemission intensity at the Fermi level (high photoemission intensity is bright). (c) The corresponding electronic structure and (d) Fermi surface after deposition of sub-monolayer quantities of Rb. Measurements were performed using photon energies of 16 eV and 32 eV for (a),(b) and (c),(d), respectively.

one from the topological surface state (two contours nearly coincide), consistent also with Refs. [115, 116]. Similar ARPES measurements have been carried out to test the role of the Ca doping, but we have found no indication of different behaviour, as expected, due to the small quantity of Ca.

In order to verify if intercalation is already taking place at 190 K, a preliminary test has been performed that exploits the reactivity of Rb with  $O_2$ . Naively, it can be expected that the intercalation of Rb protects it from being oxidised. The Rb dosed surface was therefore exposed to molecular oxygen, similarly to what has been done in the CO case and the exposure is given in Langmuir (L). Results are shown in Fig. 3.24 (e-g), evidencing how the surface rapidly deteriorates under exposure to  $O_2$ . Already after  $\approx 300$  L, the CB QWS are barely discernible. The topological state, still weakly visible, has drifted back towards higher binding energies.

In order to facilitate an eventual intercalation, a newly cleaved and similarly Rb-dosed surface has been annealed to a temperature of 350 K for 2 min. The annealing results in an electronic structure slightly sharper than the former, the doping strength is slightly reduced (the DP shifts from  $\approx 0.7$  to  $\approx 0.6$  eV), but otherwise the two cases are remarkably similar. Exposing this to the same pressure of  $O_2$  for a much longer time only results in a marginal reduction in the doping, see Fig. 3.24 (a-d). It is thus illustrated that the annealed surface is much more stable toward a reaction with oxygen: after 6400 L of  $O_2$  neither the 2DEGs nor the TS are significantly degraded.

In principle the annealing could also lead to thermal desorption instead of intercalation, as proposed in the case of potassium doping in Ref. [116]. This is a plausible alternative mechanism. However, it can not be reconciled with our experimental findings. First of all, a thermal desorption of the Rb atoms is expected to reverse the observed band bending, such that the initial electronic structure is recovered, something that clearly is not the case.

This is also not compatible with the more quantitative results obtained from XPS measurements. With these, a more accurate description of the dynamics of Rb upon annealing the  $Bi_2Se_3$  substrate can be achieved by monitoring the Bi 4f, Rb 3d and Se 3d core levels during the anneal. These measurements, shown in Fig. 3.25, display the emergence of a clear Rb 3d core level on the as dosed samples. A smaller component of a second doublet at lower binding energies is also visible. The intensity of the low-binding energy doublet is very weak at the beginning, but, as soon as the temperature is increased, it increases at the expense of the high-binding energy one. These two doublets can be interpreted in terms of the chemical shift caused by the intercalation process. It is likely that in the intercalated Rb the 3d core levels will be affected differently by the surrounding environment (i.e. they will lie at a different binding energy) than in the non-intercalated case. Spectra obtained at grazing angle also support the identification of the lower binding energy component as coming from the intercalated Rb through considerations of the inelastic mean free path. These spectra show, in fact, a prominent decrease of the lower binding energy doublet, consistent with this being related to emitters lying under the surface.

Desorption, on the contrary, would lead to a decrease of the Rb 3d core level intensity, not to the appearance of a new component in the spectrum. Also the Bi and Se core levels are affected by the doping, as expected, shifting their energy by 0.4 eV upon deposition of Rb, and then recovering slightly upon annealing.

STM measurements performed by our collaborators in Hamburg, here only summarised, also allow us to state that the influence of defect migration to the surface is negligible in this case. The STM topograph shown in Fig. 3.26 allows us to identify the features of Rb adatoms together with the Se and Ca defects. This has been acquired on a sample with a much smaller density of on-surface Rb than the one used for the photoemission experiment. The reason

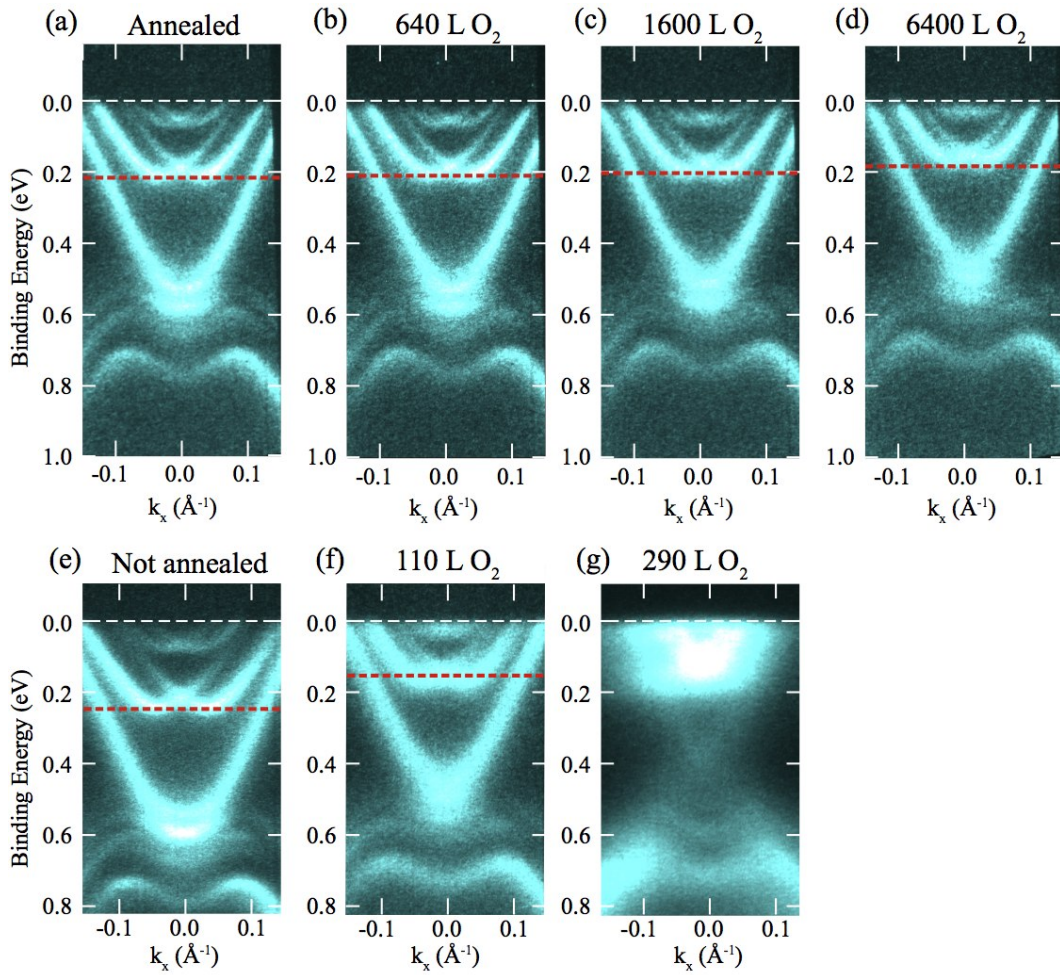


Figure 3.24: ARPES measurements of Ca-doped  $\text{Bi}_2\text{Se}_3$  (a) after depositing 0.23 ML of Rb at 190 K and annealing for one minute to 350 K and (b), (c) and (d) following exposure to 640 L, 1600 L and 6400 L of  $\text{O}_2$ , respectively. (e) A similar sample after a similar deposition of Rb at 190 K, but without subsequent annealing and (f) and (g), the same not-annealed sample following exposure to 110 L and 290 L of  $\text{O}_2$ , respectively. Data were collected at 70 K using a photon energy of 16 eV. In each case, a red dotted line indicates the approximate position of the first Rashba split 2DEG, such that a comparison of the extent of the doping is easier.

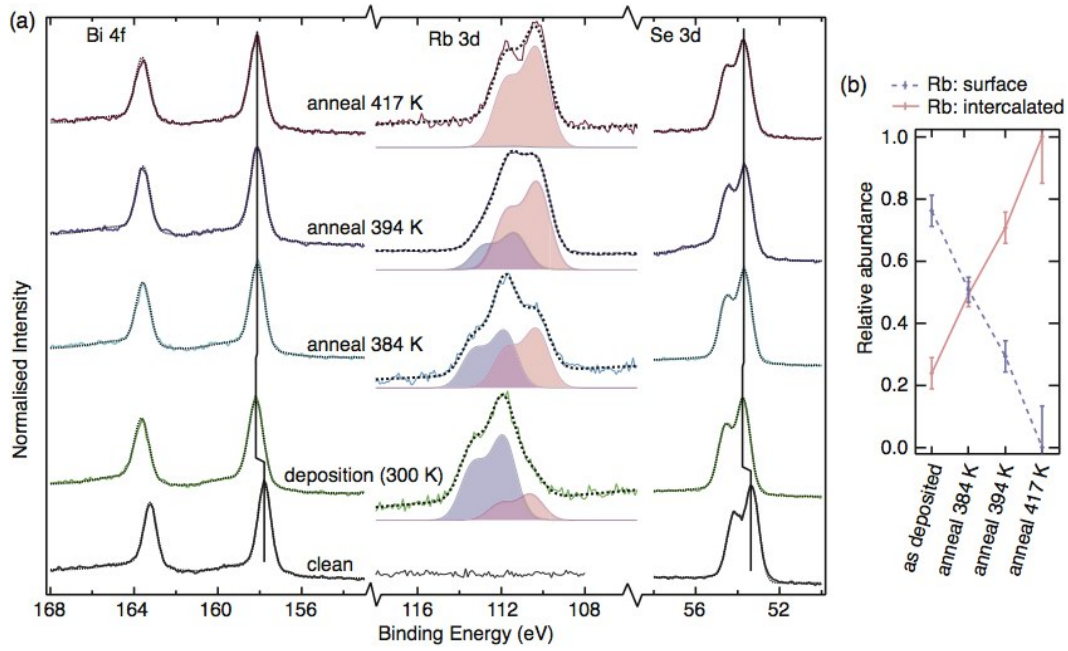


Figure 3.25: (a) Bi 4f, Se 3d, and Rb 3d core levels (coloured lines) and fits (black dotted lines) of a clean surface (bottom), followed by deposition of 0.23 ML Rb and incremental annealing for 5 min at the temperatures given. The Rb 3d core levels can be fitted by two doublets that are assigned to on-surface Rb (purple) and intercalated Rb (pink). Measurements were collected at room temperature using a photon energy of 353 eV on SGM 1 beamline on ASTRID. They have been normalised such that the principal components are of equal intensity. (b) Relative intensity of the surface and intercalated Rb components at selected stages of the experiment.

for this is that for samples with a much higher density of on-surface Rb, the subsurface Se and Ca defects are hardly visible in STM topographs due to the high contrast given by the alkali species. Triangular shaped protrusions are visible, having a lateral extent of  $\approx 2$  nm

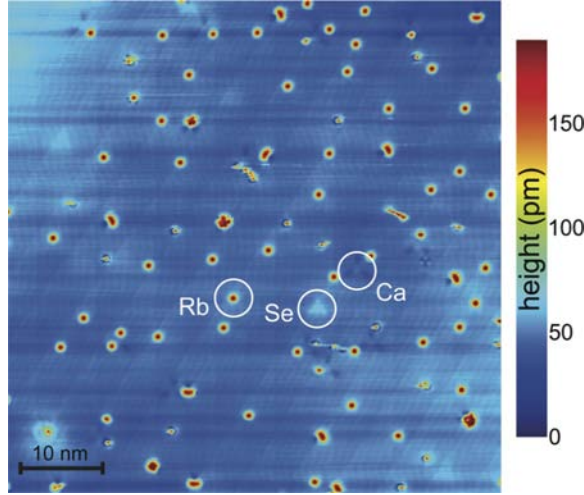


Figure 3.26: STM topograph ( $V = +1$  V,  $I = 15$  pA) of a sample with a much smaller density of on-surface Rb than shown in the photoemission data. White circles indicate the Rb adatoms and the Se and Ca defects.

and an apparent height of  $\approx 10$  pm. Consistent with the earlier publication Ref. [84], and with the other STM measurements shown in this thesis, these can be attributed to subsurface Se vacancies, while the clover leaf shaped depressions with a lateral extent of  $\approx 2$  nm are attributed to subsurface Ca acceptors. The on-surface Rb gives a very different contrast. It appears as a circular protrusion with a lateral extent of only  $\approx 1$  nm and a much larger apparent height of 150 pm. This facilitates the identification of the alkali species by their shape and corrugation. Further STM experiments were also performed on the bare Ca doped samples and, for annealing temperatures below  $150^\circ\text{C}$ , segregation of Se or Ca to the surface was not noticeable. In Fig. 3.27 a summary of the STM experiments on the Rb intercalation via annealing is presented for two different coverages, 0.025 and 0.12 ML, the latter being closer to the coverage used in the photoemission experiment, before (a,c) and after (b,d) annealing. The formation of dimers can be observed after deposition in both cases, but they do not represent the majority of protrusions among the ones ascribed to Rb. In the former case (0.025 ML) the coverage of Rb after annealing is reduced by 20%, while in the higher coverage case the reducing effect is three times larger (60%). After annealing, a limited quantity of clusters is also observed, possibly related to residual gas adsorption, but without dimers. It is interesting to note the distribution of the Rb atoms before and after the annealing. The remaining adsorbed alkali adatoms are indeed much more homogeneously distributed after annealing. This observation, together with the enhanced tendency for intercalation at higher coverage, indicates that these behaviours can be ascribed to a strong Coulomb interaction between the Rb atoms. These are, in fact, likely to be highly ionic due to a charge transfer to the bulk as described in Refs. [115, 117].

We can therefore conclude that Rb adsorption has a very pronounced effect on the near-surface electronic structure and that the formation of QWS in the CB and VB already takes

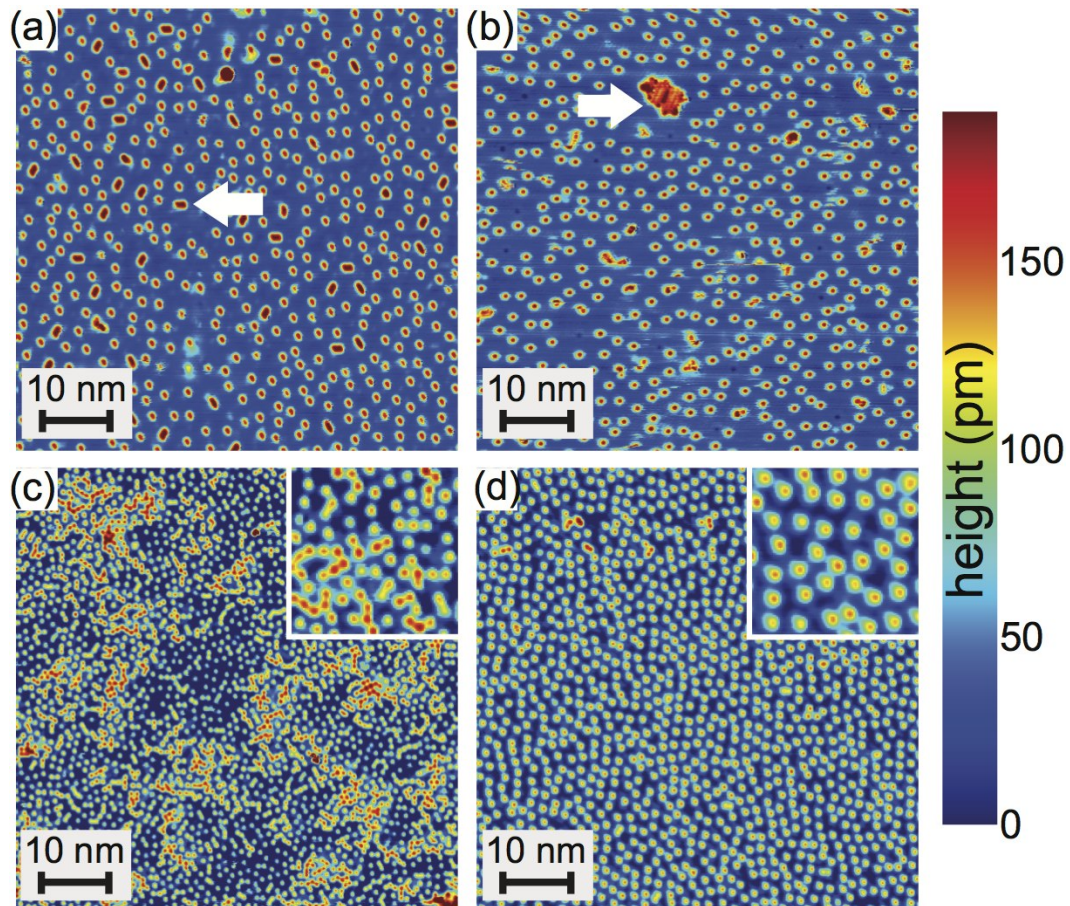


Figure 3.27: STM topograph ( $V = 1$  V,  $I = 15$  pA, temperature: 1.2 K) of 0.025 ML Rb on  $\text{Bi}_2\text{Se}_3$  before (a) and after (b) annealing at 400 K for 10 min. White Arrows indicate dimers and clusters formed. (c,d) Analogous data for a higher initial coverage (0.12 ML) of Rb before (c) and after (d) annealing. Insets show magnified views (10 nm  $\times$  10 nm).

place when Rb atoms are adsorbed on the surface. The further intercalation leads to negligible changes in the surface electronic structure, although it does lead the developed structure to become more stable, surviving in UHV for several days. An increased van der Waals interlayer spacing upon intercalation is very likely, but it is probably quite small.

An interesting experiment that could be done at this time, would be to passivate the surface in a similar way but with species giving rise to the opposite (upward) band bending, leading to a depleted charge layer (in a similar way as it has been done for graphene in Refs. [118, 119]). Such an experiment has indeed been performed in a preliminary measurement where we have deposited AlBr<sub>3</sub> on Bi<sub>2</sub>Se<sub>3</sub>. Results are still not conclusive, probably due to the p-doping caused by Br being too weak to counteract the n-doping of the impurities adsorbed during the deposition.

Having addressed all these issues, we can now concentrate on the topological state without the ageing effect misleading us. As already mentioned, the similarities between what happens in the cases shown until now, where a non-magnetic impurity is introduced on the surface, with the case of magnetic impurities, are striking. Roughly speaking, the reason for studying such a system is, ultimately, to open a gap at the Dirac point through the introduction of a perturbation capable of breaking time-reversal symmetry. Therefore we will continue now presenting the case of magnetic impurities.

### 3.2.7 Fe on Bi<sub>2</sub>Se<sub>3</sub>

T. Schlenk<sup>27</sup>, M. Bianchi<sup>1</sup>, A. Eich<sup>27</sup>, O. Pietzsch<sup>27</sup>, M. Koleini<sup>28</sup>, T. O. Wehling<sup>28,29</sup>, T. Frauenheim<sup>28</sup>, A. Balatsky<sup>30,31</sup>, J. L. Mi<sup>6</sup>, B. B. Iversen<sup>6</sup>, J. Wiebe<sup>27</sup>, A. A. Khajetoorians<sup>27</sup>, Ph. Hofmann<sup>1</sup> and R. Wiesendanger<sup>27</sup>.

Contribution: ARPES experiment strategy and execution, sample preparation, acquisition, analysis.

Reference paper: *Controllable magnetic doping of the surface state of a topological insulator*, T. Schlenk, *et al.* ArXiv e-prints (2012), 1211.2142, **Phys. Rev. Lett.** (accepted).

One of the main characteristics of the TS is the absence of spin degeneracy and this lifted degeneracy prevents back-scattering of the helical fermion. Therefore it means that, in the case of unbroken time-reversal symmetry, in order to back-scatter, the fermion must spin flip, changing its w.f. to one orthogonal to the initial one. What is experimentally done in order to study this is to introduce on the surface magnetic impurities, and the commonly used ones are Fe atoms. Calculations described in the reference paper [94] show that the magnetic spin moments of Fe ( $m_{\text{Fe}}$ ) atoms in the different lattice sites on Bi<sub>2</sub>Se<sub>3</sub> are indeed retained:  $2.7\mu_B < m_{\text{Fe}} < 3.5\mu_B$  in the Fe d shell. It has to be noted, however, that in Ref. [104] it is argued that, in order to open a gap in the case of adatoms, an ordering of the magnetic moment is needed perpendicular to the surface.

<sup>27</sup>Institute for Applied Physics, Universität Hamburg, D-20355 Hamburg, Germany.

<sup>28</sup>Bremen Center for Computational Materials Science, University of Bremen, D-28359 Bremen, Germany.

<sup>29</sup>Institute for Theoretical Physics, Bremen University, D-28359 Bremen, Germany.

<sup>30</sup>Theoretical Division and Center for Integrated Nanotechnologies, Los Alamos National Laboratory, Los Alamos, New Mexico 87545, USA

<sup>31</sup>Nordic Institute for Theoretical Physics (NORDITA), S-106 91 Stockholm, Sweden

From the spectroscopic point of view, in Ref. [103] it is described how Fe deposition on  $\text{Bi}_2\text{Se}_3$  leads to the very same change in the electronic structure that we have observed with CO, Rb and rest gas physisorption at low temperature. Also in this case, the spectral changes in the VB region resemble the quantisation of the VB near the surface, though possibly appearing as a gap opening, and leading to additional states. These unfortunately hide the spectral signature of the DP, making it difficult to identify it.

Photoemission results presented in this chapter are part of a more extended project involving STM measurements performed in Hamburg by our collaborators. These measurements (STM topographs) indicate that via low temperature deposition followed by annealing, the Fe atoms can be introduced into the topmost layers of  $\text{Bi}_2\text{Se}_3$ , both for Ca-doped and intrinsic samples. The topographs allow us to argue that a deposition of Fe on the clean substrate at  $T \approx 150$  K leads to a coverage of primarily individual Fe adatoms consistent with Ref. [120]. Fig. 3.28 shows how, after annealing to  $T \approx 260$  K, the overall density of Fe adatoms decreases, but also some clusters are formed. Together with these, also triangular shaped

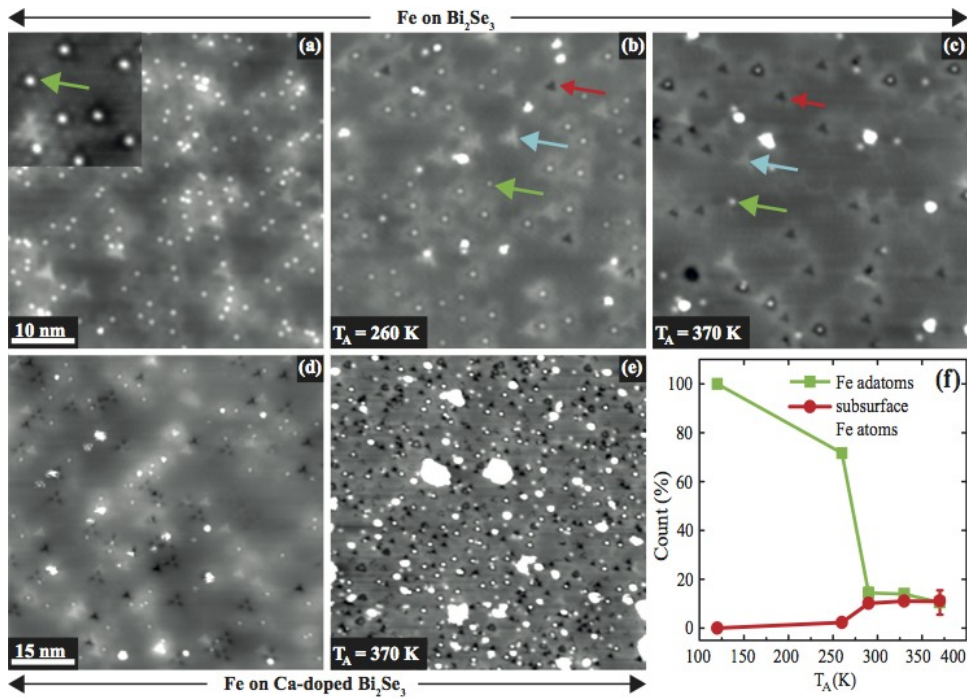


Figure 3.28: Constant current STM images of differently prepared samples of Fe on  $\text{Bi}_2\text{Se}_3$  ( $I_t = 50$  pA,  $V_b = 0.25$  V (a-d),  $V_b = 1$  V (e).) (a) Cold deposited Fe ( $\approx 1\%$  of a ML) on pristine  $\text{Bi}_2\text{Se}_3$ . Inset: magnified view showing 8 individual Fe adatoms ( $10\text{nm} \times 10\text{nm}$ ,  $V_b = 0.3$  V,  $I_t = 1$  nA). (b), (c) Samples prepared as in (a) annealed to  $T \approx 260$  K and 370 K, respectively. (d) Cold deposited Fe (0.5% ML) on Ca-doped  $\text{Bi}_2\text{Se}_3$ . (e) Sample prepared as in (d) but with 6% ML Fe and annealed to  $T \approx 370$  K. (f) Number of Fe adatoms and subsurface Fe atoms relative to initial Fe adatom number as a function of annealing temperature. Emergent clusters were not counted in the statistics. Subsurface Fe atoms are highlighted by red arrows, Fe adatoms by green arrows, and Se vacancies by cyan arrows respectively.

depressions in the STM topograph appear and, according to the literature [121, 122, 123], it seems to be established that these are an indication of substitutional Fe atoms residing in Bi sites. After a higher temperature annealing ( $T \approx 370$  K) this process continues, and the density of the triangular-shaped depressions increases significantly, accompanied by an increase of the clusters' size, at the expense of the number of Fe adatoms.

This preliminary insight into what happens at the surface once Fe has been deposited allowed us to find the right parameters for the sample preparation used for the photoemission experiment. For the ARPES measurements we have proceeded as follows: after in-situ cleaving, subsequent iterations of cold Fe deposition at  $T=150$  K and annealing to  $T= 370$  K were performed with no cleaving in between. The amount of subsequently deposited Fe was increased for each iteration (1%, 2.5%, 5%, 10%). Calibrations were performed by XPS, analogous to what has been done in Ref. [124] (which appeared as a preprint a few weeks after our measurement), and by calibration of the evaporator on different substrates. The time elapsed between two measurements with a deposition in between was about 5 min. Figs. 3.29 and

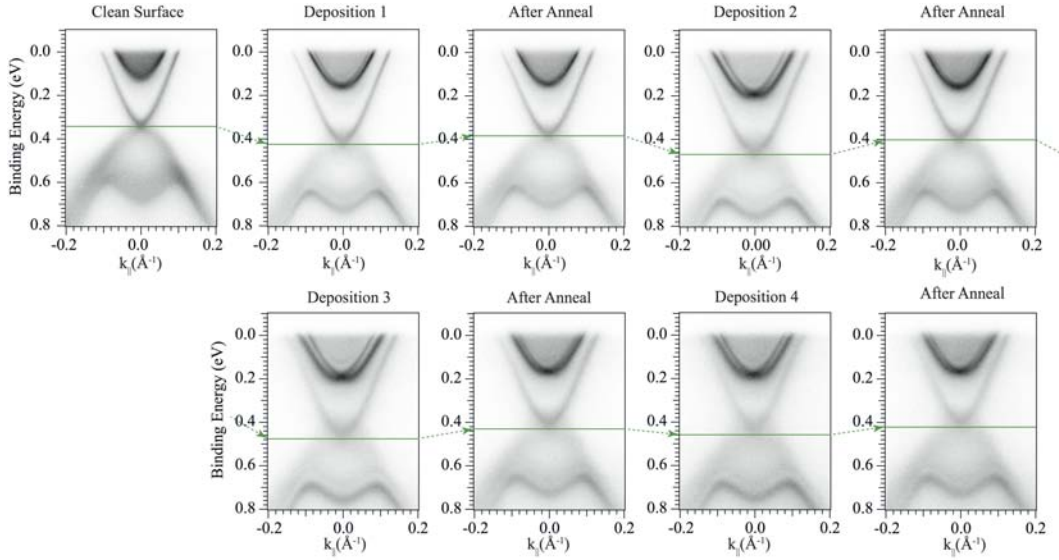


Figure 3.29: ARPES measurements for pristine  $\text{Bi}_2\text{Se}_3$  (gen. V) samples after different Fe deposition and annealing steps. On the top-left initial spectra after in-situ cleaving are shown. Subsequent cycles of cold deposition of Fe ( $T \approx 150$  K) and annealing at  $T \approx 370$  K followed. The DP position is marked with a green horizontal line. Deposition 1 corresponds to 1%, 2 to 2.5%, 3 to 5% and 4 to 10%.

3.30 show the spectra acquired after each stage for intrinsic and Ca-doped crystals respectively. The images were acquired after each cold deposition, but before subsequent annealing, (Deposition 1, 2, etc. in both Fig. 3.29 and 3.30). They show the downward shift of the DP as compared to its pristine position. We can thus conclude that Fe adatoms are donors and therefore induce downwards band bending. The similarity of this behaviour with the cases investigated in the previous chapters should be noted. Indeed such band bending leads to the described QWS in both the conduction and the valence bands, with the Rashba splitting of the 2DEGs. After annealing to the temperatures where STM data show diffusion into the

subsurface, the DP shifts upward as indicated by the horizontal green lines in Figs. 3.29 and 3.30 and the QWS are barely detectable.

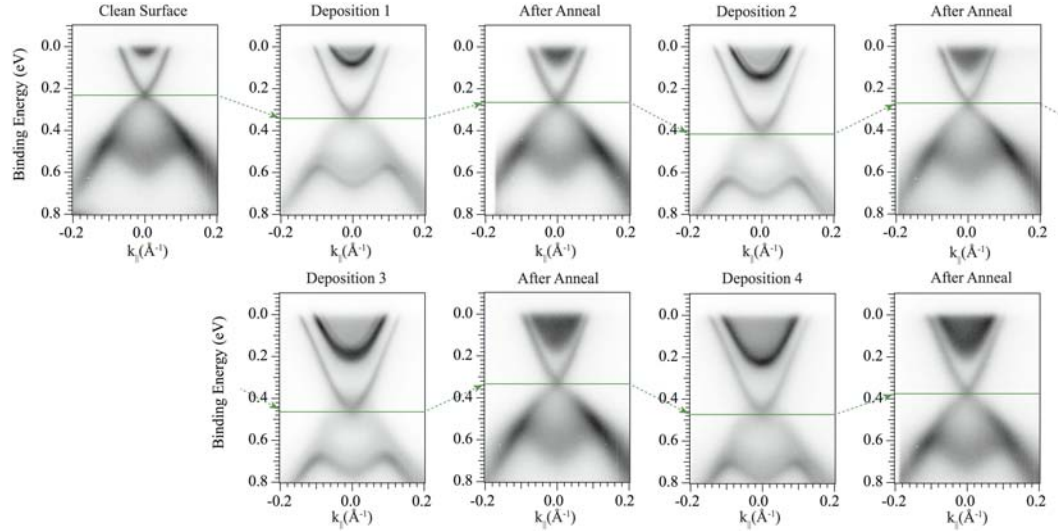


Figure 3.30: ARPES measurements for Ca-doped  $\text{Bi}_2\text{Se}_3$  (gen. VII) samples after different Fe deposition and annealing steps. On the top-left initial spectra after in-situ cleaving are shown. Subsequent cycles of cold deposition of Fe ( $T \approx 150\text{K}$ ) and annealing at  $T \approx 370\text{K}$  followed. The DP position is marked with a green horizontal line. Deposition 1 corresponds to 1%, 2 to 2.5%, 3 to 5% and 4 to 10%.

In order to exclude the influence of the elevated level of rest gas ( $1 \times 10^{-9}$  mbar) generated by the Fe source, that would also lead to a downward band bending after deposition and upward banding after anneal, the following test has been performed. The very same procedure of Fe deposition has been followed but keeping the shutter of the Fe evaporator closed. No appreciable change in the band bending has been observed after this simulated deposition.

Taking into account the STM-observed thermally-induced subsurface diffusion of Fe adatoms, this sequence of ARPES experiments indicates that substitutional (subsurface) Fe atoms are either neutral dopants or electron acceptors, while the Fe adatoms that are prepared by cold deposition are electron donors. No gap opening has been observed. This is clearer in this case, rather than in the previous ones, as the doping level is lower and the DP is not hidden by the VB QWS as happens in the case of CO and Rb doping.

This result is contrary to the recent ARPES study that finds surface electron doping for Fe deposition at RT and hole doping for cold deposited Fe in Ref. [124]. This striking difference for such a similar experiment can only be attributed to the different quality of the crystals used or a different deposition rate. It is known in fact that a leading factor in diffusion is the surface quality and density of defects. Furthermore, even though negligible in the previous case of Rb, where the doping is stronger, it is possible that here diffusion of defects during the anneal may play an important role. Such a discrepancy, however, clearly needs further investigation, and is left as an open question. This issue might be addressed in the future by using high resolution ESCA microscopy on a different crystal generation.

### 3.2.8 Stability of $\text{Bi}_2\text{Se}_3$

Richard C. Hatch<sup>1</sup>, Marco Bianchi<sup>1</sup>, Dandan Guan<sup>1,2</sup>, Shining Bao<sup>2</sup>, Jianli Mi<sup>6</sup>, Bo Brummerstedt Iversen<sup>6</sup>, Louis Nilsson<sup>1</sup>, Liv Hornekær<sup>1</sup> and Philip Hofmann<sup>1</sup>

Contribution: experimental design, strategy and execution, sample preparation, acquisition, minor part in analysis.

Reference Paper: *Stability of the topological state on  $\text{Bi}_2\text{Se}_3$* , R. C. Hatch, *et al.* **Phys. Rev. B** **83**, 241303(R) (2011).

The limitations on backscattering introduced at the beginning of the previous chapter does not mean that the TS is protected in an absolute sense from scattering, as there are still coupling and decay processes allowed. Among these interactions, the electron-phonon coupling has been shown to be easily accessible with our experimental apparatus. In fact, exploiting the relations presented in Eq. 1.19, what can be done with our equipment is to monitor the peak position and the width of the relevant states at different temperatures as shown in Fig. 3.31.

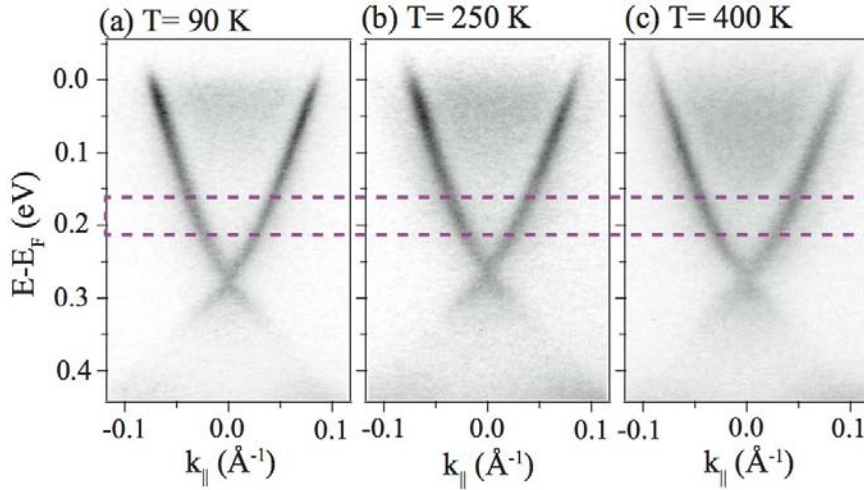


Figure 3.31: ARPES spectra taken at (a) 90 K, (b) 250 K and (c) 400 K with a photon energy  $h\nu = 16$  eV. The magenta dashed lines indicate the region considered for the analysis.

As  $\mathcal{A}(\omega, \mathbf{k})$  is a 3D function<sup>32</sup>, what can be done is to restrict our attention to a certain direction, typically a high symmetry direction, constraining  $\mathcal{A}(\omega, k_{\parallel})$  to be 2D. In this way it is possible to analyse the width of the state in the energy direction (Energy Distribution Curves EDC, i.e. intensity versus energy at a fixed  $\theta$ <sup>33</sup>) or in the momentum direction (Momentum Distribution Curves MDC, i.e. intensity versus  $\phi$  at a fixed energy<sup>33</sup>  $E$ ), see Eq. 1.16. Due to the presence of the Fermi edge and the fact that the spectral function itself in the EDC

<sup>32</sup> $\mathcal{A}(\omega, \mathbf{k})$  versus kinetic energy (or binding energy) and  $\mathbf{k} = (k_x, k_y)$ .

<sup>33</sup>As during this work most of the data were  $k$ -warped before the analysis, by EDC we mean also intensity versus energy at fixed  $k_{\parallel}$  instead of  $\theta$ . Analogously, by MDC it is meant both intensity versus  $\phi$  at fixed energy and intensity versus  $k_{\parallel}$  at fixed energy.

is complicated near  $E_F$  (see discussion in Chap. 1.3.1), the best choice is to do an MDC analysis.

The biggest challenge in this experiment is the ageing of the surface states. This constrains the time available to acquire the data and therefore the number of temperatures that can be probed. For this reason we have opted for measuring as many cleaves and samples (gen. V) as possible and, for each of them, we acquired spectra only at a low (80 K) and at a high (250 K) temperature<sup>34</sup>. The time elapsed between the cleave and the end of the last acquired spectra never exceeded 15 min. The measurements shown were always performed starting from low temperature and proceeding to high temperature. However, analogous sets of data have been acquired from high temperature to low temperature, but, due to the time needed to cool the sample, the latter procedure took more than 25 min (data not shown).

Fig. 3.32 presents the quantitative analysis of the line-shape and peak position that was performed as follows for each cleave, sample and temperature: the dispersion of the state has been obtained by fitting with two Lorentzians each single MDC lying in a 50 meV wide energy range, centred at 100 meV over the DP. This energy range has been chosen as it is away from the CB bottom rim, which not only simplifies the fitting, but also restricts the phase space available for EPC scattering (see further discussion). The position of the MDC peak has been fitted with a polynomial to obtain a noise-free group velocity ( $\nu$ ) which finally, combining it with the Lorentzian FWHM, allowed us to obtain  $\Sigma''$  as described in Eq. 1.21.

Once we obtained  $\Sigma''$  for the two temperatures, the slope of  $\Sigma''$  was obtained, which is proportional to  $\lambda$ . This method is justified in the realm of a full Debye model, where  $\Sigma''$  behaves linearly with temperature when  $T \gtrsim T_\Theta$ . In the case of  $Bi_2Se_3$  the Debye temperature of the system is  $T_\Theta \approx 182$  K [60]. As noted in Chap. 1.3.1, a linear approximation turns out to be acceptable also for temperatures somewhat lower than  $T_\Theta$ . This is shown in Fig. 3.32 (c) where the calculation of the electron-phonon scattering related self-energy in the Debye model is depicted.

As the values of  $\Sigma''$  vary between cleaves and samples, as result of an inhomogeneous defect distribution (see Fig. 3.32 (a)), the data sets have been individually offset in energy such that a line fit through all the data points minimised  $\chi^2$  (Fig. 3.32 (b)). The obtained  $\lambda$  is  $0.25 \pm 0.05$ .

Even though the experimental procedure adopted minimised the acquisition time, the actual value of  $\lambda$  might be slightly smaller due to time dependent life-time broadening. Fig. 3.32 (d) represents the measured  $\Sigma''$  as a function of time after cleave at room temperature and shows it increasing with a rate of 0.35 meV/minute. The last measurement allows a correction to be made to  $\Sigma''$  at high temperature, that is measured  $\approx 5$  min after the low temperature one. This leads to a correction of 1.75 meV in  $\Sigma''$  and a corrected value of  $\lambda_{\text{corr}} = 0.21$  consistent with the previous value.

In order to understand the meaning of this value, we can compare it to some known, albeit extreme, cases. The measured lambda is higher than that of a good conductor, for example noble metals have  $\lambda \approx 0.1$ . On the other hand it is smaller than a BCS superconductor, where  $\lambda \approx 1$ . In the context of these two extrema the measured value is surprisingly high for a TS, as will become clear in the following discussion.

Let us now address this point with some considerations of the phase-space available for scattering, depicted in Fig. 3.33. Assuming a photo-hole of energy  $E$  and due to the finite

---

<sup>34</sup>Even though 80 K is not the minimum temperature reachable by the manipulator, this value has been chosen as it represents a good compromise between the time needed for the sample to cool down and what is meant by *low* temperatures in the Debye model, see Chap. 1.3.1.

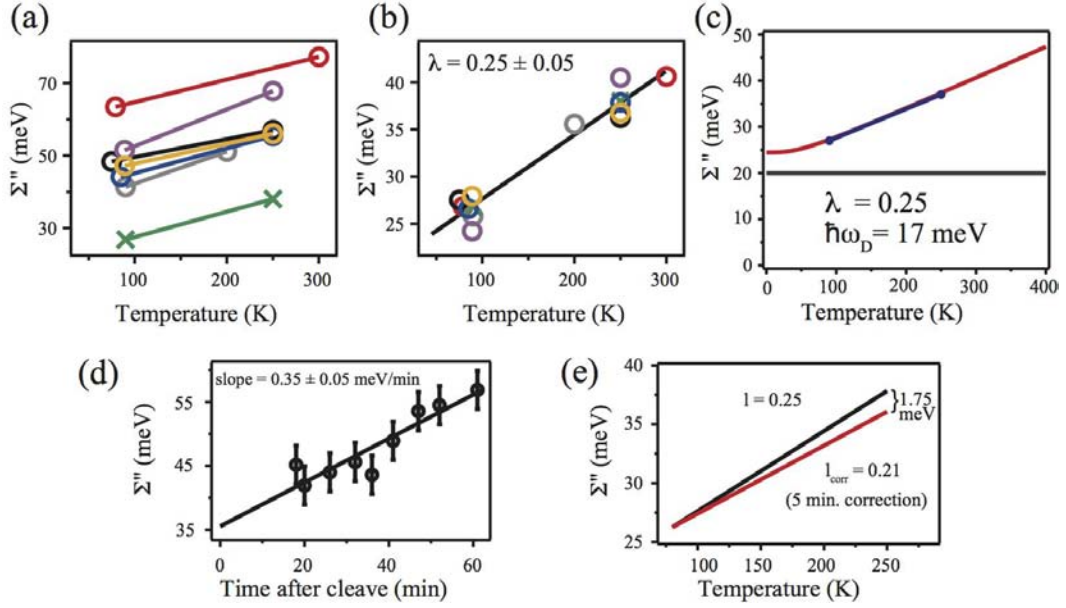


Figure 3.32: (a) Temperature dependence of  $\Sigma''$  for different samples or cleaves. The estimated uncertainty for each point is  $\pm 3$  meV. (b) Data from (a) where the values have been shifted in energy such that a line fit through all the data minimises  $\chi^2$ . (c)  $\Sigma''$  temperature dependence as calculated in a full Debye model (red) and comparison with a linear fitting (blue) in the experimental temperature range. The parameters for the calculations are  $\lambda = 0.25$ , the Debye energy  $\hbar\omega_D = 17$  meV [60] and a binding energy consistent with that where the MDC fit has been performed (0.2 eV). (d) Linear time dependence of  $\Sigma''$  at room temperature (300 K) revealing a slope of  $0.35 \pm 0.05$  meV/min. (e) Time broadening correction to  $\Sigma''$  temperature dependence. The black line represents the data presented in (c) while the red assumes a 5 min delay between scans using results from (d) and gives the corrected value of  $\lambda_{\text{corr}} = 0.21$ .

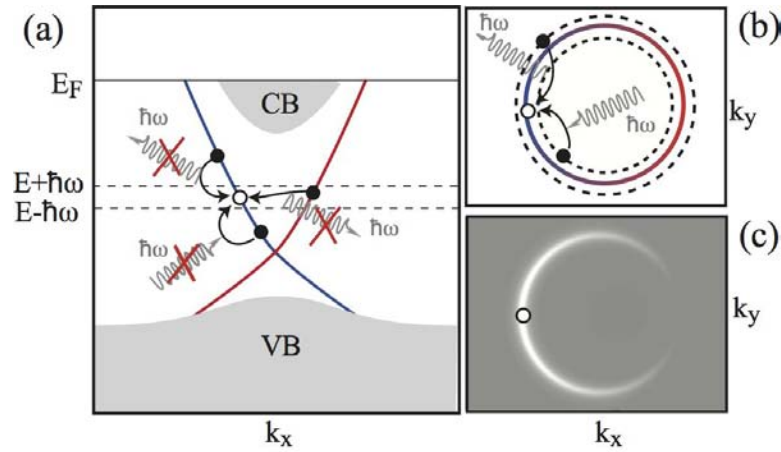


Figure 3.33: (a) Sketch of the band structure of  $Bi_2Se_3$  showing the topological surface states lying in the bulk band gap between the VB and CB. A photo-hole of energy  $E$  can be filled by electrons which absorb or emit a phonon and originate from an energy window of  $\pm\hbar\omega$  where  $\hbar\omega$  is the maximum phonon energy in the material. With red crosses are highlighted which kind of transitions are not permitted, either due to wrong energy scale, or spin conservation. (b) Sketch showing how the absorption or emission of a phonon can excite electrons to fill the photo-hole. (c) Spin dependence of the probability that an electron with a certain  $k_x$  and  $k_y$  will fill the photo-hole (bright areas having the highest probability).

phonon energy spectrum available, whose maximum energy can be taken as  $\hbar\omega$ , only electrons that originate from an energy window of  $\pm\hbar\omega$  can emit or adsorb a phonon in order to fill the hole. Furthermore the phase space available is reduced by the spin conservation during the process. As the topological state is characterised by a defined spin polarisation, a photo-hole of momentum  $-k$  can not be filled by an electron with opposite momentum as it will have the opposite spin direction. The probability of this process will follow, in fact, from the projection of the electron's spin polarisation into that of the photo-hole. This effect is clarified by Fig. 3.33(c) that depicts the probability of an electron in this energy range to fill a photo-hole in a certain  $k_x$  and  $k_y$ .

It is worth comparing this result to the situation in Ag(111), where the intra- and inter-band contributions to  $\lambda$  have been calculated in Ref. [126] and the intra-band contribution (described in 3.34(b)) is very small. These are summarised in Fig. 3.34(a) where the combined contribution to  $\lambda \approx 0.14$  at  $E_F$  is shown, out of which only 0.02 is given by the intra-band scattering.

A brief discussion about the scattering from static defects can also be introduced at this point. In order to address this issue a test has been done exploiting the creation of defects using 15 seconds of sputtering<sup>35</sup> with 0.7 keV  $Ne^+$  at a pressure of  $3 \times 10^{-6}$  mbar. This should

<sup>35</sup>This ion-bombardment technique is commonly used in order to clean the surface of a single crystal exploiting their scattering with impurities on the surface. This technique is unfortunately not suitable for alloys because of the difference in scattering cross-section of the species present in the alloy. In this case, for example, this technique will probably lead to a Se- or a Bi-enriched surface.

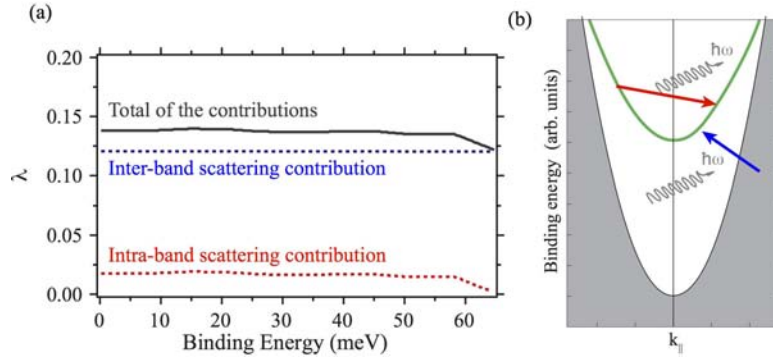


Figure 3.34: (a) Calculations of the two different contributions, inter-band (blue) and intra-band (red) scattering, to  $\lambda$  (gray) in the case of Ag(111) as a function of binding energy. (b) Schematic of the (111) surface state (green line) of noble metals with inter-band (blue arrow) and intra-band (red arrow) scattering denoted. Grey area represents the bulk continuum. (a–b) Adapted from Refs. [126, 127]

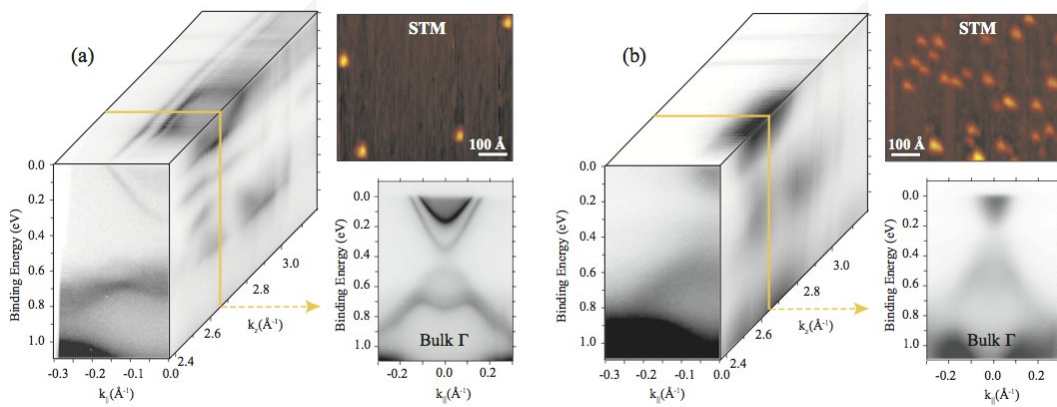


Figure 3.35: Comparison between the pristine surface (a) and the sputtered one (b). The effect of defect creation on the surface is shown by the absence of 2D features in the energy scan of the sputtered surface, while bulk features are largely unchanged. Images corresponding to the bulk Brillouin zone are shown separately. STM images ( $600 \times 500 \text{ \AA}$ ) of the surfaces before and after sputtering are also shown, courtesy of L. Nilsson.

strongly affect the 2D states associated with the surface, while having only a minor influence on the 3D bulk states. The system has then been studied both with photoemission and STM (by L. Nilsson) in analogous conditions. Results are presented in Fig. 3.35 that compare the situation before and after sputtering where a complete removal of the 2D related features is observed. While the disappearance of the 2DEG and M-state can easily be attributed to the induced perturbation, the absence of the topological state (TS) is more difficult to account for, due to its topological nature. One should notice that this measurement gives an indication that the concentration of defects on the surface obtained with this procedure is rather low as

the bulk projections are still evident and largely unchanged. STM measurements allow us to estimate an average distance between defects of 425 Å for the pristine surface, decreasing to 85 Å for the sputtered one. This facilitates the quantification of the effect of each scattering defect, by estimating the uncertainty in the crystal momentum ( $\Delta k_{\parallel}$ ) due to the change in the surface electrons mean free path  $\lambda_{\text{eff}} = 1/\Delta k_{\parallel}$  [128]. In fact, if every defect acts as a scattering centre, we can obtain for the pristine surface  $\Delta k_{\parallel} = 0.002 \text{ \AA}^{-1}$ , rising to  $0.012 \text{ \AA}^{-1}$  for the sputtered surface. The latter value appears too small to justify the extinction of the TS [102].

What can be argued however, is that, even though the TS is still there, it might be buried underneath a thick and disordered layer at the surface, and therefore inaccessible to photoemission. Such a naive idea does not seem to be so far-fetched and it has indeed been recently considered in Ref. [129] and thoroughly discussed in Ref. [130] with a theoretical approach. In the latter it is argued that two qualitatively different regimes can be reached under conditions of high disorder on the surface: one where a moderate disorder destroys the Dirac cone, inducing a diffusive metallic behaviour at the surface, and one where the TS is buried under what can actually be considered an Anderson insulator due to its high level of disorder. Given our STM results it is likely that with our sputtering experiment we reach the first regime. Again in Ref. [130] it is argued that the topological protection of the surface layer should not be taken in an absolute sense, as it is only relevant for weak disorder. On the other hand as we read in Ref. [130]:

*“... disorder with a strength comparable to or larger than the bulk gap first leads to diffusive metallic behavior and then to Anderson localization at the surface.”*

### 3.2.9 $Bi_2Se_3$ bulk electronic structure

I. A. Nechaev<sup>36,37</sup>, R. C. Hatch<sup>1</sup>, M. Bianchi<sup>1</sup>, D. Guan<sup>1</sup>, C. Friedrich<sup>38</sup>, J. L. Mi<sup>6</sup>, B. B. Iversen<sup>6</sup>, S. Blügel<sup>38</sup>, Ph. Hofmann<sup>1</sup> and E. V. Chulkov<sup>37,25</sup>.

Contribution: ARPES experiment strategy and execution, sample preparation, acquisition, analysis.

Reference Paper: *Evidence for a direct band gap in the topological insulator  $Bi_2Se_3$  from theory and experiment*, I. A. Nechaev, *et al* arXiv:1210.4477v1 (submitted).

The discussion in the previous chapter points out again the importance of the bulk electronic structure and symmetry. In particular, one of the fundamental details to be addressed concerns the energy gap that is crossed by the TS. Though many calculations are presented in the literature (e.g. Ref. [50]), only little has been shown experimentally. One of the issues is, for example, that it is still unclear if  $Bi_2Se_3$  is characterised by having a direct or indirect band gap. This detail is not only interesting from a purely scientific perspective, but also from a technical point of view, especially if these materials are to be used for electronic devices. From this latter perspective, transport through the topological state is the target one would

<sup>36</sup>Tomsk State University, 634050, Tomsk, Russia

<sup>37</sup>Donostia International Physics Center (DIPC), 20018 San Sebastián Donostia, Basque Country, Spain.

<sup>38</sup>Peter Grünberg Institut and Institute for Advanced Simulation, Forschungszentrum Jülich and JARA, D-52425 Jülich, Germany.

like to reach, accessing the topological transport regime with the chemical potential near the DP, but simultaneously in the absolute bulk band gap. However, this can only be possible at energies close to or higher than the DP, and if there are no other VB states. This is because, as seen in the previously shown energy scans (Figs. 3.8, 3.10, 3.18), the DP lies in close proximity to the VB at  $\bar{\Gamma}$ .

What is evident (and has been well established) from many traditional  $h\nu$  scans in the  $\Gamma-Z-F$  direction [44, 131, 132], is that the CB minimum lies at  $\Gamma$ . A systematic investigation of the dispersion along the  $\bar{\Gamma}\bar{M}$  direction, along which the VB maximum (VBM) is predicted to be, is still to our knowledge missing. Therefore in this part we report on combined theoretical and experimental evidence for such a direct band gap in  $\text{Bi}_2\text{Se}_3$ , systematically exploring the VB dispersion along the high symmetry directions with photoemission. For reasons of completeness the calculations will be briefly described, although the full details go beyond the scope of this work. A more detailed discussion of the calculations' insight can be found in the reference paper.

In Chap. 2.3.1 it has been introduced how, exploiting the tuneability of the photon source and the abilities of the SPECS Phoibos 150 analyser, it is possible to acquire a full 3D map of the electronic structure in the BZ. The method described here was implemented performing photon energy scans from  $h\nu=14$  to 32 eV in 0.1 eV steps. The combined energy resolution for these measurements was  $\lesssim 22$  meV and the angular resolution was  $\approx 0.15^\circ$ . Samples were cleaved as usual at room temperature, then cooled to  $\approx 70$  K for the measurements. The  $k_z$  values for the three-dimensional representation of the scans were calculated using Eq. 2.2 with  $V_0 = 11.8$  eV. This value has been tested thoroughly by iteratively changing  $V_0$  such that the  $k_z$  value corresponding to the observed  $\Gamma$  and  $Z$  points agrees with the size of the  $\text{Bi}_2\text{Se}_3$  BZ. It should be noted that this value is not only in good agreement with the one reported previously and in Refs. [46, 134], but also it turns out to be the only one giving a correct  $\Gamma-Z$  distance between 4 and 26 eV.

Due to the intrinsic problems of visualising such a 3D dataset  $(E_{\text{kin}}, k_x, k_z)$ , again only the most relevant fraction of the data, i.e. those in the  $\bar{\Gamma}\bar{M}$  direction, will be shown. We will concentrate on this direction as it is along this where the VBM is predicted to be according to DFT calculations presented in the literature [21, 51, 79, 135]. This subset of data allows us to visualise the photoemission intensity as a function of  $k_z$  for a given  $k_{\parallel} = k_{\bar{\Gamma}\bar{M}}$  or at a constant  $k_z$  as a function of  $k_{\bar{\Gamma}\bar{M}}$  as shown in Fig. 3.37(a) and (b) respectively. A scheme of the BZ is shown Fig. 3.36 that gives the relevant directions in the BZ. Note that the distinguishing feature of these ARPES measurements is that they probe a large fraction of k-space on a dense grid of emission angles and photon energies.

Having these data available, in principle, it should be straightforward to verify if we are in possession of a direct or indirect band gap, by looking around the BZ to see where the VB maximum lies. However, the problem concerning bulk band mapping in this case is the width of the bulk related features. These do not appear as sharp photoemission features and simple Lorentzians can not fit them as done in the 2D case. Furthermore the colour coding and the presence of the quantised states makes their visibility in the images presented less clear. A new way of treating the data or a new and more convincing method of analysing them still needs to be implemented, and this is an interesting technical problem to be addressed in the future. A hint on how this can be done, when in presence of faint or poorly defined features, is presented in Ref. [136] where a first derivative of the intensity as a function of the energy has been applied to render the  $\sigma$  bands of graphene on Ni(111) more visible. This method is for example commonly used for Auger spectra where peaks are broad and poorly-defined. A more advanced method is also described in Ref. [137] where a second derivative in two variables is used.

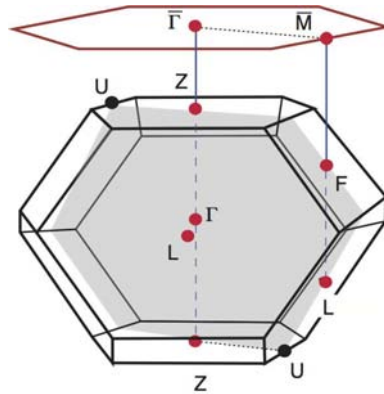


Figure 3.36: Bulk Brillouin zone of  $\text{Bi}_2\text{Se}_3$  (in black) and its projection onto the (111) surface (in red). The grey plane is a bulk mirror plane.

What has been done here, in order to guide the interpretation of such spectra, is to compare the as  $k$ -warped data with results of DFT calculations supplied by our collaborators as presented in Fig. 3.37. Fig. 3.37(a) corresponds to  $k_{\bar{\Gamma}\bar{M}} = 0 \text{ \AA}^{-1}$  (normal emission) and shows two features that disperse along  $k_z$ . This is analogous to the previously shown energy scans. As said before, these two features derive from the CB and VB, and, as usual for intrinsic samples, the CB is partially occupied. The three non-dispersing features (i.e. with 2D character) are the topological state at the Dirac point (at a binding energy (BE)  $\approx 0.45 \text{ eV}$ ) and the previously discussed 2DEG (BE  $\approx 0.25 \text{ eV}$ ) and M-State (at BE  $\approx 0.75 \text{ eV}$ ). Note that the intensity of these is enhanced at the photon energies for which bulk states with a similar wavefunction periodicity along  $k_z$  is observed. In particular the TS and 2DEG are enhanced at  $\Gamma$  while the M-state is enhanced near Z.

The results of different *ab initio* calculations are also shown on top of the experimental data represented by points and curves. These DFT calculations are based on the LDA (Local Density Approximation) and GGA (Generalized Gradient Approximation). Details on the algorithm used for these calculations and theoretical considerations are beyond the scope of this thesis. Furthermore a discussion on the DFT calculations and the pro and cons of using LDA instead of GGA is not appropriate here. However, for those who might not be familiar with such a field, an extremely sketchy outline will be provided that gives the basic ideas, another introduction can also be found in Ref. [138]. The expert reader might be asked for his sympathy if such a complex and delicate theory will be simplified to the bones.

As briefly introduced in Chap. 1 the problems of solving the Schrödinger equation for such a complicated system are the many interactions and correlations between particles. A traditional quantum mechanical approach attacks the Schrödinger equation directly, and frequently applies approximations in order to get the eigenstates  $\Psi$ . Having these, it is possible to calculate the expectation value of the interesting observables, e.g. the density of particles  $n(\bar{\mathbf{r}})$ .

Density Functional Theory is able to justify an approach to the problem that, conceptually, goes exactly backwards. In the DFT<sup>39</sup> it is demonstrated how from a certain  $n(\mathbf{r})$ , it is possible to obtain the eigenvalues and the external potential characterising the Schrödinger

<sup>39</sup>The heart of the theory can somehow be considered the Hohenberg-Kohn theorems.

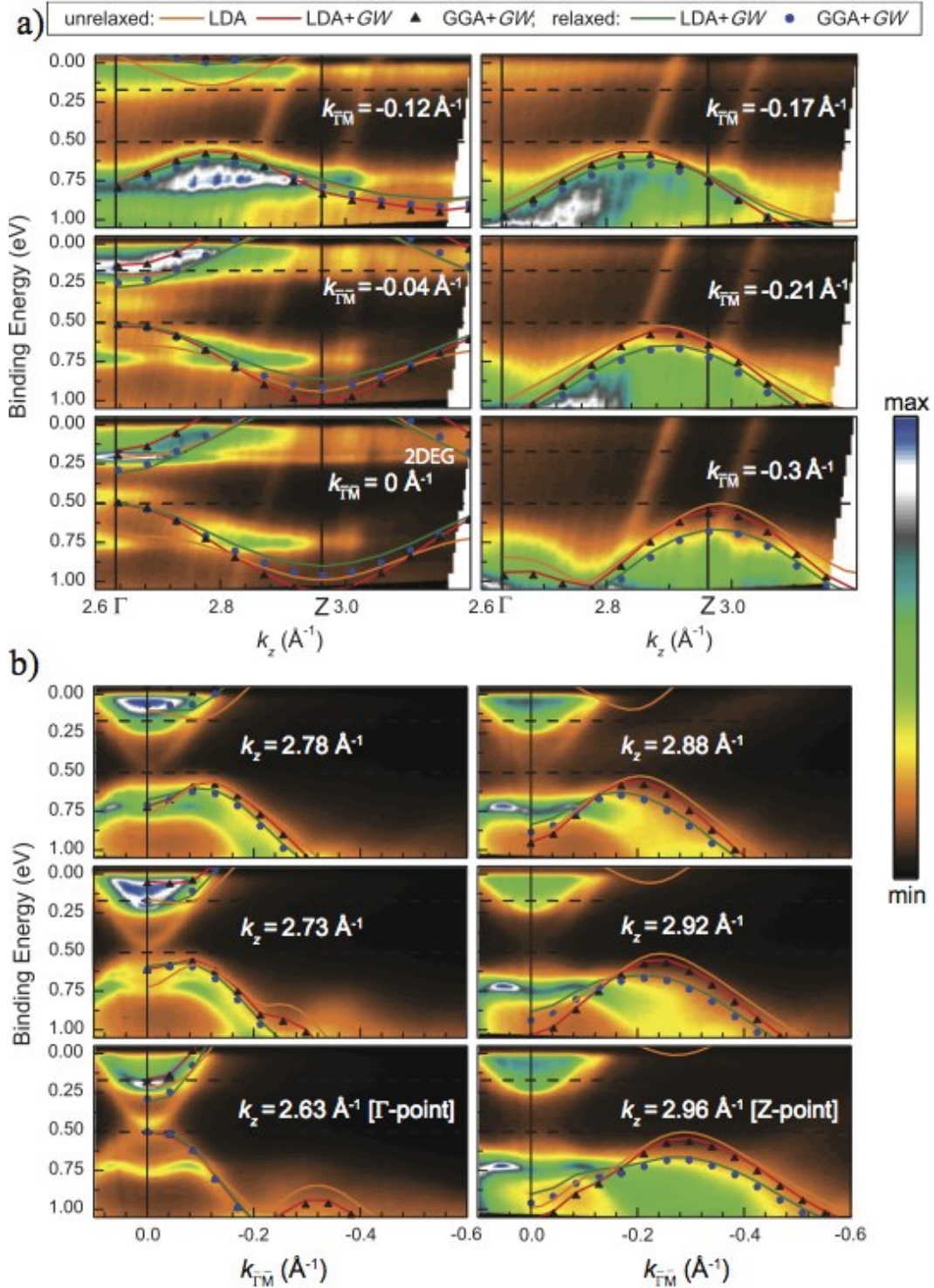


Figure 3.37: Slices extrapolated from a  $h\nu$  scan showing photoemission intensity at different constant parallel momenta  $k_{\Gamma M}$  along directions parallel to  $\Gamma$ - $Z$  (a) and normal momenta  $k_z$  along directions parallel to  $ZU$  (b). Dashed horizontal lines correspond to the experimentally observed energies of the VBM and the CBM. The theoretical curves have been shifted to have the VBM at the same energy as in the ARPES experiment. They represent the lowest conduction band and the uppermost valence band obtained for the experimental [86] (unrelaxed) and relaxed atomic positions without (LDA) and with (LDA+GW or GGA+GW) the GW corrections to the DFT (LDA or GGA) band structure. In (a), the two parallel and nearly vertical lines of higher photoemission intensity seen at  $k_z$  values of roughly  $2.8$  and  $3.0 \text{ \AA}^{-1}$  correspond to Bi  $5d$  core levels which have been excited by second-order light coming from the monochromator.

eq. and therefore the expectation value of the observables. In other words, this justifies rewriting the Schrödinger eq. in terms of functionals of  $n(\mathbf{r})$  and reorganising all the terms so that all the “hard” parts are included in a term called Exchange-Correlation  $E_{XC}$ . The name originates from the fact that typically it is decomposed in an Exchange term  $E_X$ , originating from the Pauli principle, and a Correlation term  $E_C$ . Note that the theory is formally exact, the approximations come into play only when trying to calculate  $E_{XC}$ . Two commonly used local approximations for  $E_{XC}$  are the LDA and the GGA. The LDA approximates the real inhomogeneous system as a sum of many infinitesimal “cells” where the density and the effective potential are constant. The GGA is a semi-local approximation where the spatially varying density  $n(\mathbf{r})$  is approximated somehow by the LDA’s local density with a correction of the form  $\nabla n(\mathbf{r})$ .

The LDA and GGA allow us to reveal the effect of different reference one-particle band structures on the GW approximation results. The GW is used to take into account the many-body corrections. In this approximation the self-energy  $\Sigma$  is expanded in terms of the single particle Green function (G) and the screened coulomb interaction (W), hence the name GW.

Note that in this work, the GW approximation is also where the SOI is taken into account as done in Ref. [139]. Two different sets of atomic positions for Bi and Se atoms in a rhombohedral crystal structure have been considered: one labelled “unrelaxed” that uses the experimental lattice parameters taken from Ref. [86], and one labelled “relaxed” where the parameters were obtained during a relaxation procedure optimising the atomic positions under the constraint of fixed volume.

Experimentally we observe the VBM at  $0.505 \pm 0.030$  eV and the CBM  $0.170 \pm 0.025$  eV, giving an experimental value for the band gap of  $0.332 \pm 0.055$  eV. The best agreement between experiment and calculations seems to be reached in the case of the LDA+GW calculations using relaxed atomic positions, even though the band gap is not well reproduced (0.19 eV). On the contrary the unrelaxed one gives a value for the gap that is in better agreement (0.34 eV).

In the case of the GGA the introduction of the GW diminishes the calculated value for the gap from 0.31 to 0.30 eV in the unrelaxed case, and from 0.28 to 0.21 eV in the relaxed case. A summary of these results can be found in Table 3.1.

| Exchange Correlation term | Gap type | Unrelaxed positions | Relaxed positions |
|---------------------------|----------|---------------------|-------------------|
| LDA                       | indirect | 0.30                | 0.25              |
| LDA+GW                    | direct   | 0.34                | 0.19              |
| GGA                       | indirect | 0.31                | 0.28              |
| GGA+GW                    | direct   | 0.30                | 0.21              |

Table 3.1: Calculated band-gap type and values in eV for  $Bi_2Se_3$  using the different approximations considered.

Fig. 3.38 also summarises the results of such calculations for the different approximations that have been considered. This figure shows the projections of the lowest CB and uppermost VB in the high symmetry mirror plane in the BZ onto the  $\bar{\Gamma}\bar{M}$  direction. Looking at these, three general trends should be noted. First of all, as indicated by the red arrows, taking the GW approximation into account leads to a decrease in the band gap at  $\bar{\Gamma}$ . Secondly, the GW is also responsible for moving the VBM towards  $\bar{\Gamma}$  in both the LDA and the GGA. These two trends have also been consistently observed in previous studies presented in Ref. [140]. Thirdly, as a general trend in the projections considered and away from  $\bar{\Gamma}$ , the two bands are moved apart by considering the GW approximation (dark yellow arrows in Fig. 3.38).

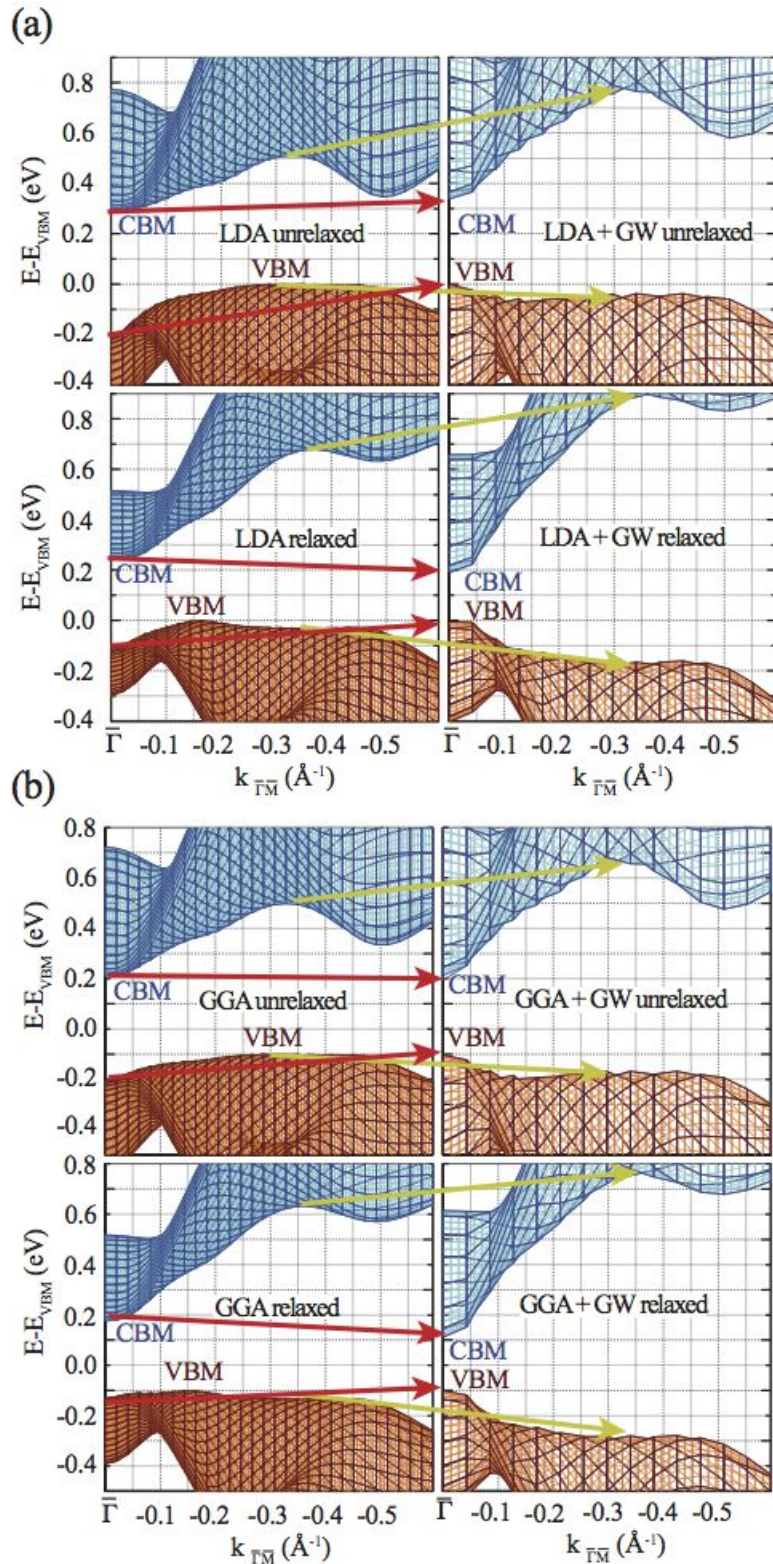


Figure 3.38: Projections of the lowest CB and the uppermost VB in the mirror plane on the  $\bar{\Gamma}M$  direction of the surface BZ. The presented results are obtained for the unrelaxed (upper row) and relaxed (lower row) atomic positions with and without the GW corrections to the LDA (a) and GGA (b) band structure, respectively. Red arrows highlight the shrinking of the gap at  $\bar{\Gamma}$  once the GW approximation is introduced for the relaxed and unrelaxed LDA and GGA cases. Dark-yellow arrows highlight the general moving apart of the bands away from  $\bar{\Gamma}$ .

Such a combined movement can be traced back to a reduction of the “penetration” (hybridisation) of the bands into each other near  $\Gamma$ . What can be argued is that this is due to the band inversion that is generated by the SOC and responsible for  $Bi_2Se_3$  being a TI. This is ultimately the cause of the two bands getting closer at  $\Gamma$ , contrary to the more common situation without band inversion [140].

Concluding, we can say that results of LDA+GW and GGA+GW superimposed on the experimental data give a strong indication of a direct band gap in  $Bi_2Se_3$ .



# Chapter 4

## Outlook

Part of this PhD project consisted of designing a new end-station to be mounted on the SGM 3 beamline at the new synchrotron radiation facility ASTRID2. This opportunity was also taken to improve the properties of the end-station, enriching it with more capabilities for sample preparation and surface characterisation. The science involved in designing a beamline and a synchrotron goes beyond the scope of this thesis, and a justification of the choice of every single detail in the design of the end-station would be tedious and unnecessary. Therefore the scope of this chapter is to present the principles that have guided this work, together with the design requirements, and to show the final result. This work has been realised together with the engineers and design team at the department of Physics and Astronomy and the ISA group working on the new synchrotron and beamlines. In particular John Erik Vad Andersen has to be acknowledged for his essential help giving technical suggestions and realising (and checking) all the drawings, of which a few are presented here.

The new beamline on ASTRID2 will have the same energy characteristics as the original SGM 3, and also the same undulator and monochromator. The major improvements are being made to the storage ring and by the new optics on the beamline. Very briefly, through a smaller electron bunch at the undulator position, frequent top-up injections and a new mirror system, a brighter light spot at the sample position can be obtained. This, roughly speaking, means both a smaller and a more intense spot than the previous one, allowing a better angular resolution and intensity at the detector. This means that the last pinhole will not be needed anymore. The new optics are designed in such a way that the light will arrive at the sample parallel to the floor at a height of 1 m, instead of at an angle as it is in the current setup. This last detail simplifies the design of the frame holding the chamber, minimises wear on the moving and rotating mechanical parts, and allows for more comfortable operation and maintenance.

Before starting the design of a chamber, what has to be clear in mind is the knowledge of the instruments that are going to be mounted on it and the possible (reasonable) experiments that a scientist in the field would like to run (e.g. concerning surface preparation and characterisation, different ARPES acquisition schemes, flexibility in mounting different instruments in the future). It is clear that the problem contains hidden complexity, as a chamber is an intricate system in UHV where many different instruments work and fit together in a very constricted space. Furthermore it is desirable that an external user, with general UHV experience but not accustomed to that particular chamber, is able to run experiments mostly independently from the beamline's staff and in a safe way. These details are fundamental if one considers that, on a daily basis, a sample needs to be transferred, prepared, checked,

measured with different techniques and all in the fastest, simplest and most comfortable way possible.

The first fundamental boundary condition given for such a project is necessarily the position of the beamline's (the light's) focus. This not only fixes the measurement position for the sample, and therefore the manipulator holding it, but also that of the analyser. The task was to design a new flexible system analogous to the one used here and described in Chap. 2.3, recycling as much as possible from it, and adding the following abilities:

1. Faster recovery of UHV from high pressure conditions ( $> 1 \times 10^{-3}$  mbar), i.e. smaller UHV volumes;
2. Controllable epitaxial growth;
3. Ability to perform *in situ* STM measurements;
4. Ability to perform *in situ* XPS measurements with a commercial X-ray source;
5. More degrees of freedom in sample rotations: automatic tilt and azimuthal rotations in the measurement position;
6. Lower sample temperature during ARPES measurements.

All of these are closely interconnected problems (e.g. having a cryostat running in the MC manipulator creates vibration that prohibits normal STM operation). This project will be, however, presented in two sections. The first describes how with the new chamber design the first 4 tasks can be achieved. The second describes a new manipulator designed to fulfil the last two requirements. Note that the requirements for the new chambers must take into account not only the design of the new manipulator but also the limited space available in the ring-hall for the end-station<sup>1</sup>.

## 4.1 The new ARPES end-station on ASTRID2

Figs. 4.1 and 4.2 show an overview of the new end-station from the top and from the side respectively. The overall system is similar to the previous one: a load lock (LL) is mounted on a preparation chamber (PC1) that is connected via a valve to a main chamber (MC). PC1 is the original one, however a modification of the LL was necessary in order to accommodate a commercial Aarhus STM that will be mounted on the CF150 flange indicated by the green arrow in Fig. 4.1. Considering the scientific experiments presented in this work, the importance of being able to perform *in situ* STM measurements is clear.

PC1 will be pumped as before by: a cryo-pump, a Ti sublimation pump, an ion-pump, and a magnetic levitating turbo-pump; the rough pumping is shared with the LL via a set of valves. A shortening of the pumping tube was necessary, where the turbo-pump and the ion-pump are placed. This was done to make the pumping more efficient, fit the entire system in the new lower setup and let the human operations on it be more convenient.

The LL has been modified also to be used, when not occupied in the loading of a sample into UHV, as a supplementary pumping system for gas-lines, the rotational feedthrough etc.. This will be pumped by a magnetically levitating turbo-pump. The MC is a  $\mu$ -metal chamber, smaller than the previous one, thanks to the absence of the old VG Scienta analyser. This chamber can be divided into two levels. At the highest level the transfer of samples from PC1

---

<sup>1</sup>Pillars and walls are present near the end of the beamline.

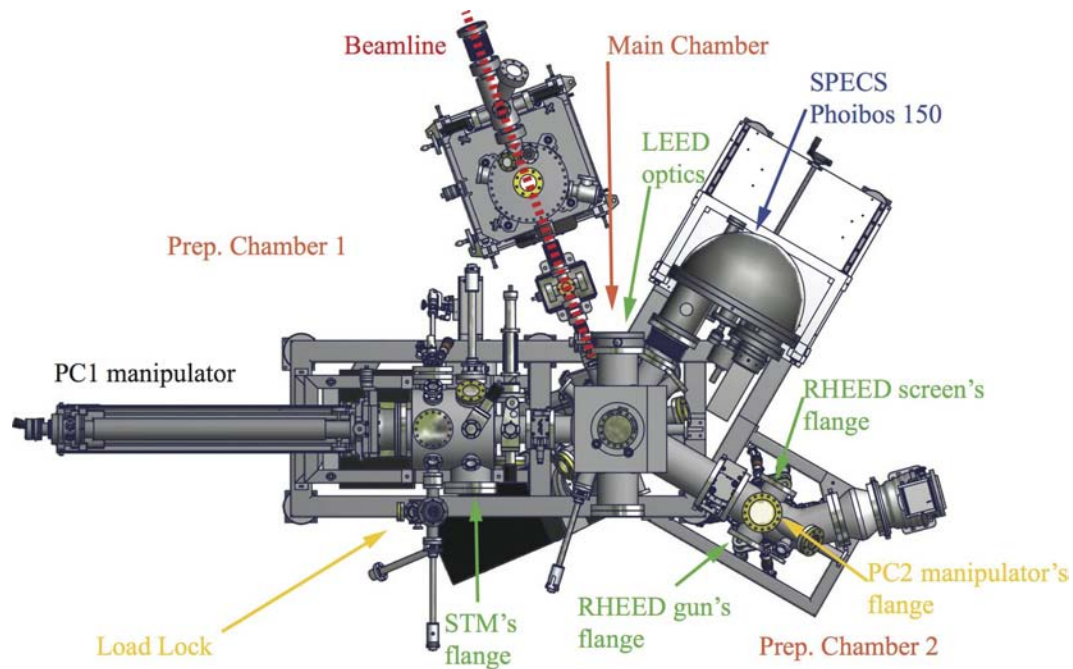


Figure 4.1: Top view of the new SGM3 end-station with the last mirror of the beamline whose axis is indicated by the red dashed line. Red arrows indicate the main bodies of the end-station, the green ones indicate the measurement instruments, in blue the analyser and in yellow the LL and the PC2 elements are indicated.

and LEED measurements are performed. At the lowest level the ARPES data are acquired and transfers to a second preparation chamber (PC2) are done.

PC2 is a new chamber and it is where the epitaxial growth of crystals can be performed in a controlled way. It is pumped by a magnetically levitating turbo-pump and the rough pump is a scroll pump. PC2 is equipped with:

- a CF150 flange able to host up to 4 retractable evaporators mounted vertically, or 3 evaporators and a sputter gun;
- a manipulator with 2 degrees of freedom, where the sample will be held facing down towards the evaporators;
- a RHEED<sup>2</sup> system that allows the monitoring of the thin film growth;
- a “Tungsten heater”<sup>3</sup>, where a sample can be heated to high temperature using e-bombardment, monitoring the temperature with a pyrometer;
- a gas line or a sputtergun;

<sup>2</sup>Reflection High Energy Electron Diffraction

<sup>3</sup>This has been inspired by our collaborators in Hamburg and it minimises the degassing during the heating procedure.

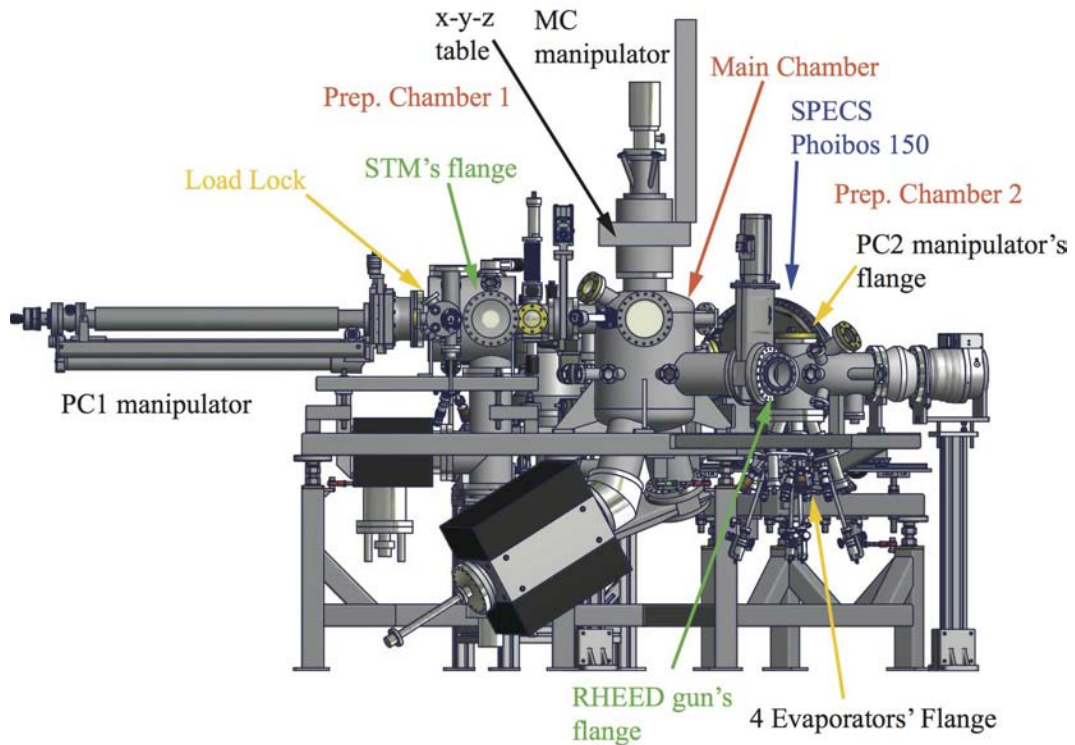


Figure 4.2: Side view of the new SGM3 end-station from the side opposite to the beamline. Red arrows indicate the main bodies of the end-station, green ones indicate the measurement instruments, in blue the analyser and in yellow the LL and the PC2 elements are indicated.

- a long magnetic transfer arm with a rotating shaft for the transfer to the MC (not shown).

The MC remains the core of the end-station and it has been designed to fulfil the following requirements:

- be as small as possible;
- compatibility with both the original and the new manipulators;
- hosting the SPECS Phoibos 150 analyser, the beamline and the LEED optics;
- be magnetically shielded at the ARPES position<sup>4</sup>;
- allow the view of the chamber's interior during the transfer of samples;
- flexibility to accommodate an XPS source or eventually evaporators;
- must be easily mountable, in order to facilitate its alignment with the beamline.

<sup>4</sup>Even though being  $\mu$ -metal, this requirement put constraints on the length of the flanges' neck depending on their diameter.

Furthermore the LEED optics and the analyser must be oriented so that the transfer from the LEED acquisition position to the ARPES one (and vice versa) is as fast as possible. The LEED optics should also be oriented so that LEED measurements can be performed even while holding the sample on the PC manipulator<sup>5</sup> or rotating azimuthally the sample on the PC socket<sup>6</sup>. A detail of a 2D horizontal section of the MC is shown in Fig. 4.3, that should

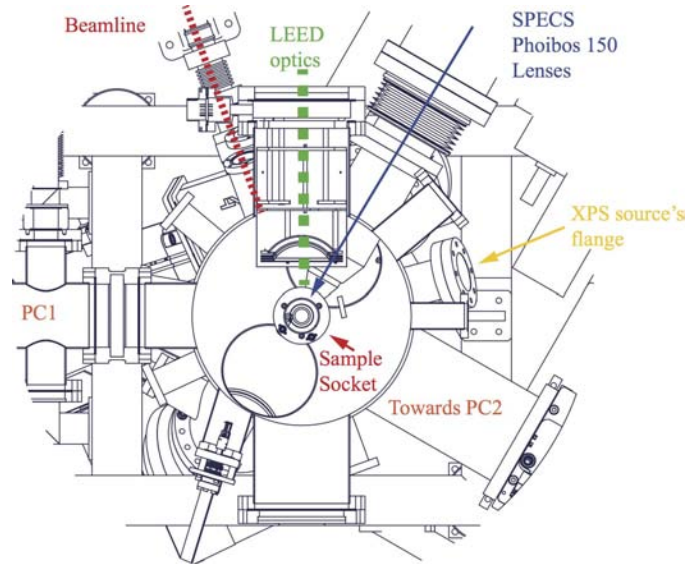


Figure 4.3: 2D horizontal section of the MC at the LEED optics level. A green dashed line indicates the LEED optics' axis while a solid blue arrow indicates that of the analyser. The top of the socket is also visible at the centre of the chamber.

help to clarify the fulfilment of these requirements. Thanks to our collaborators' care and patience, all the transfers and movements in vacuum have been checked virtually using CAD software.

When normally operating, the MC is pumped by a Ti sublimation pump, a cryo-pump, an ion-pump and a NEG-pump (Non-Evaporable Getter pump). These are at the bottom of the chamber, looking at the ARPES measurement position from the bottom. However, in the case of the ion-pump, where a magnetic field is present, this has been placed as far away as possible from the analyser and the measurement position. The MC can also be pumped by the turbo-pumps both via PC2 or via PC1. This will become handy in situations where a high pumping speed is desirable, for example during baking or for measurements of the type shown in Fig. 3.16.

Last but not least, an important detail has to be considered that is the frame holding in place the end-station. This must allow its fine alignment: the focus of the beamline (the

<sup>5</sup>Due to gravity the sample can fall off the PC manipulator. This originates ultimately from the design of the sample holder and socket.

<sup>6</sup>This possibility has been blocked recently as in the past this turned out to be a convoluted procedure for an external user. In order to reach the LEED measurement position, one should rotate both the sample and the manipulator with a very high risk of losing the sample.

light) and that of the analyser, the centre of rotation of the sample<sup>7</sup> and the surface of the sample must, in fact, coincide.

To accomplish this, the frame is made up of three bodies. A lower body, equipped with wheels and stoppers, is used for the macroscopic movements and the secure placement of the end-station. Another frame (labelled central) is mounted on top of the previous one. This allows the fine movements of the end-station, through acting on bolts and pullers, in all the directions with respect to the light focus (strictly speaking: up, down, left, right and tilt). A smaller frame is finally fixed on top of the central one; this allows the analyser movement with respect to the MC so as to adjust the focus of the lenses. Note that the entire end-station, i.e. LL, PC1, MC, PC2 and analyser moves rigidly together when adjusting the central frame.

The choice of magnetically levitating turbo-pumps and the use of vibrational dampers is justified by the goal of low vibration. This, according to their technical specifications, should allow the operation of the Aarhus STM even without having the chamber on levitating feet. *In extremis*, a system of valves can be closed allowing the turbo-pumps to be shut down, leaving PC1 pumped only by the ion-pump.

The detail that still need to be investigated is the cryostat used for the MC manipulator. This cryostat, being an expander (which is essentially a reciprocating piston), is actually the source of most of the vibrations on the chamber. Until a new, low vibration, closed-cycle He cryostat compatible with UHV becomes available on the market, we will continue to use the original one, taking care to turn it off during the STM measurements.

In order to hold the heavy and long PC1 manipulator mounted horizontally, either a suspended crane or a vertical support from the floor is needed. We have solved this issue similarly to what has been done in the original design, using a system of pulleys and counterweights. This simple idea has been further augmented by the use of a suspended double track that allows us to hold and dismount the PC manipulator easily, without the need for a crane. Using a bifurcation, it also holds the old and the new MC manipulators simultaneously, facilitating their exchange. A crane for additional maintenance will also be present on one of the tracks.

### 4.1.1 The 6 axis manipulator

The project of this manipulator has been inspired by the group of Prof. Karsten Horn<sup>8</sup> who we acknowledge also for useful discussions and collaboration.

The manipulator is mounted with its z-drive as the original one on a x-y table that allows  $\mu\text{m}$  movements of the manipulator (and therefore of the sample) in the three Cartesian directions. The table is mounted on the same rotatable flange (rotational feedthrough) that is used in the original setup to perform the polar ( $\theta$ ) rotations during the ARPES scan. The core of the manipulator is the head, where the copper socket holding the sample is mounted on a support (Fig. 4.4 (a)) that holds also the long rotating shafts implementing the rotations. The particulars of the head's design are presented in Fig. 4.4 where the sample front (b) and rear (c) side are shown. The head is made of three independently-moving copper bodies that, starting from the sample holder going towards the manipulator, are:

1. a central cylinder actuating the azimuthal rotations and holding the sample, heating filament and thermocouples;

---

<sup>7</sup>These are the MC manipulator rotations.

<sup>8</sup>Electronic Structure of Surfaces and Interfaces group, Department of Physical Chemistry, Fritz-Haber-Institut der Max-Planck-Gesellschaft, Berlin, Germany.

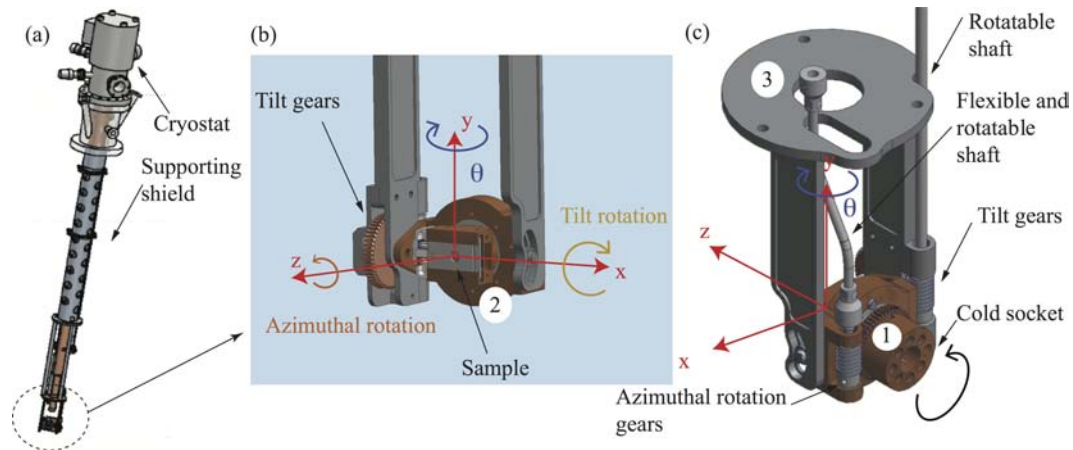


Figure 4.4: Schematics of the new manipulator (a) with particulars of the new sample socket from the sample front (b) and rear (c) side respectively. The manipulator linear translations are indicated by the red arrows. Orange arrows in (b) and black in (c) indicate the new degrees of freedom which are automatically controlled. The blue arrows in (b) and (c) indicate the  $\theta$  rotation also available in original manipulator. Numbers inscribed in circles are consistent with the labelling given in the text.

2. a horseshoe-shaped body that holds the former and actuates the tilt rotation;
3. a C shaped frame holding everything in place.

Two sets of worm gears separately mounted on 1 and 2 provide tilt and azimuthal rotations. The design is intended to be easily maintained and repaired and solid enough to support (and allow) the transfer of the sample many times per day.

Note that 3 is supported by an outer shield on the manipulator, which also holds the rotating shafts, and is therefore at room temperature. Only 1 is connected directly to the cryostat on the top of the manipulator via a flexible copper braid on the back (not shown in Fig. 4.4). All the thermal insulation between stages 1, 2 and 3 is achieved with a careful choice of materials, knowing that the junction between a metal and a ceramic, or a metal and a plastic material results in a thermally insulating junction.

In particular, where the dimensions allow it, ceramic ball-bearings (in particular  $\text{ZrO}_2$ ) will be used, and where this is not possible, metallic ball-bearings with a PEEK<sup>9</sup> retainer are adopted. Concerning the worm gears, representing a possible heat source, the choice has been to use a metallic worm wheel with a PEEK worm screw. Our collaborators using a similar design were able to reach a lower temperature than the existing manipulator using an open cycle of liquid He and metallic bearings. Note that all these parts, aside from the ceramic bearings, are either easily machinable in the department's workshop or can be quickly purchased for replacements.

The shafts actuating the two additional sample rotations are connected to a rotatable feedthrough on the top of the manipulator. These are moved by two stepper motors controlled by the acquisition software. The issues concerning such a manipulator are the size of the

<sup>9</sup>PolyEther Ether Ketone is a commonly used organic polymer thermoplastic in engineering applications that is practically UHV compatible.

external shield holding the shafts and the head, and the overall weight of the manipulator with cryostat, x-y table and z-drive. The last problem concerns the ability of both the MC and the rotatable flange<sup>10</sup> to bear the weight of the manipulator without deforming<sup>11</sup>. This is solved by the system of pulleys and counter weights that holds the manipulator's weight.

Note that now all the degrees of freedom are remotely controlled (in the previous system only the  $\theta$  rotations was remotely controlled). This opens new possibilities for ARPES acquisition schemes, e.g. the acquisition of a real azimuthal scan keeping the incident light at constant angle during Fermi surface mapping, and it allows the detection of all the high symmetry directions in a  $h\nu$ -scan without the need to physically remount the sample with a different orientation.

The chamber and the new manipulator are under construction at the time this work has been submitted.

---

<sup>10</sup>This can hold a maximum of 80 Kg.

<sup>11</sup>Unfortunately  $\mu$ -metal is softer than stainless steel.

# Chapter 5

## Conclusions

The surface electronic structure of the topologically non-trivial semimetal Sb(110) and the topological insulator Bi<sub>2</sub>Se<sub>3</sub>(111) have been investigated with ARPES. The discussion of the presented results has been supported by STM measurements and theoretical calculations performed by our collaborators. The conclusions have been drawn in each section of Chap. 3 and will be summarised in the following.

**Sb(110): Fermi surface mapping and topology.** A high resolution Fermi surface map of Sb(110) has been measured and compared with DFT calculations clarifying the dispersion of the surface states. Along directions connecting TRIMs without any bulk Fermi-surface contribution, the observed band dispersion is in agreement with the predictions of the surface bands topology. The topological arguments become invalid if the projected bulk Fermi surface is present and the surface bands are allowed to mix with the bulk state.

**Bi<sub>2</sub>Se<sub>3</sub> pristine surface electronic structure.** This has been presented for nominally stoichiometric and calcium-doped samples and shows the topological surface state in the bulk band gap. The ageing effect that brings the Dirac point towards higher binding energies has also been described for different samples.

**Quantised states in the conduction and valence band.** The ageing effect, consisting of a band bending, leads to the appearance of additional states near the Fermi level resembling the features of two-dimensional electron gasses (2DEG). These can be interpreted as quantised states in the conduction band and are described by a simple Schottky model. This model is able to reproduce the general trend of their Rashba splitting that is observed for stronger band bending. It has been discussed how an interpretation in terms of band bending is also consistent with the appearance of quantised states in the valence band.

**Origin of the band bending.** The origin of the ageing effect in UHV can be identified as the adsorption of impurities (e.g. CO) on the surface coming from the rest gas of the UHV chamber. However, different interpretations have also been discussed. The cold deposition of Rb and Fe on the surface leads to very similar effects, with different n-doping. In the case of CO, a situation similar to the pristine surface can be recovered by heating the sample. XPS and STM measurements indicate that annealing the sample in the case of Rb and Fe facilitates their intercalation into subsurface layers. For adatoms the n-doping effect is always stronger than for sub-surface atoms. This

shows that relaxation of the last quintuple layers' van der Waals gap does not play the main role in the formation of the additional 2D-states observed here.

**Stability of the topological state** The stability of the topological state has been investigated via temperature-dependent ARPES prior to the ageing effect becoming appreciable. In particular the electron-phonon coupling strength  $\lambda$  is found to be 0.21. Scattering from static defects has also been investigated combining ARPES and STM. This study shows how the introduction of a moderate amount of defects already leads to the disappearance of the topological state. A possible interpretation for such an effect has been discussed. These results are consistent with a recent theory describing a similar behaviour of the TS under conditions of high disorder on the surface of a TI.

**Bi<sub>2</sub>Se<sub>3</sub> bulk band structure** Experimental data for the electronic bulk band structure of Bi<sub>2</sub>Se<sub>3</sub> along  $\bar{\Gamma}\bar{M}$  direction have been presented together with DFT calculations. Both indicate the presence of a direct band gap which is measured to be  $0.332 \pm 0.055$  eV.

Finally in Chap. 4 the design of the new SGM 3 beamline's end-station at ASTRID2 has been presented. This allows for more capabilities in sample preparation (molecular beam epitaxy) and surface characterisation (via STM, RHEED and XPS) thanks to the new equipment that can be hosted in the new chamber. This was presented together with the description of a new manipulator that allows for more flexibility in ARPES acquisition schemes and lower sample temperatures.

# List of Abbreviations

|                         |   |
|-------------------------|---|
| <b>ARPES</b>            | Angle-Resolved Photoemission Spectroscopy |
| <b>BE</b>               | Binding Energy                            |
| <b>BZ</b>               | Brillouin Zone                            |
| <b>CB</b>               | Conduction Band                           |
| <b>CBM</b>              | Conduction Band Minimum                   |
| <b>DFT</b>              | Density Functional Theory                 |
| <b>DP</b>               | Dirac Point                               |
| <b>EPC</b>              | Electron-Phonon Coupling                  |
| <b><math>E_F</math></b> | Fermi Energy                              |
| <b>FL</b>               | Fermi Level                               |
| <b>FWHM</b>             | Full Width at Half Maximum                |
| <b>GGA</b>              | General Gradient Approximation            |
| <b>LDA</b>              | Local Density Approximation               |
| <b>QWS</b>              | Quantum Well State                        |
| <b>SBZ</b>              | Surface Brillouin Zone                    |
| <b>SOC</b>              | Spin-Orbit Coupling                       |
| <b>SOI</b>              | Spin-Orbit Interaction                    |
| <b>SS</b>               | Surface State                             |
| <b>STM</b>              | Scanning Tunneling Microscopy             |
| <b>TB</b>               | Tight Binding                             |
| <b>TI</b>               | Topological Insulator                     |
| <b>TRIM</b>             | Time-Reversal-Invariant Momentum          |
| <b>TS</b>               | Topological State                         |
| <b>UHV</b>              | Ultra-High Vacuum                         |
| <b>VB</b>               | Valence Band                              |
| <b>VBM</b>              | Valence Band Maximum                      |
| <b>w.f.</b>             | Wavefunction                              |
| <b>XPS</b>              | X-ray Photoemission Spectroscopy          |
| <b>2DEG</b>             | Two-Dimensional Electron Gas              |



# Bibliography

- [1] L. Fu and C. L. Kane, Phys. Rev. Lett. **100**, 096407 (2008).
- [2] J. Linder, Y. Tanaka, T. Yokoyama, A. Sudbø, and N. Nagaosa, Phys. Rev. Lett. **104**, 067001 (2010).
- [3] X.-L. Qi, R. Li, J. Zang, and S.-C. Zhang, Science **323**, 1184 (2009), URL <http://www.sciencemag.org/cgi/content/abstract/323/5918/1184>.
- [4] L. Fu and C. L. Kane, Physical Review B **76**, 045302 (pages 17) (2007), URL <http://link.aps.org/abstract/PRB/v76/e045302>.
- [5] L. Fu, C. L. Kane, and E. J. Mele, Physical Review Letters **98**, 106803 (pages 4) (2007), URL <http://link.aps.org/abstract/PRL/v98/e106803>.
- [6] J. E. Moore and L. Balents, Phys. Rev. B **75**, 121306 (2007).
- [7] D. Hsieh, D. Qian, L. Wray, Y. Xia, Y. S. Hor, R. J. Cava, and M. Z. Hasan, Nature **452**, 970 (2008), URL <http://dx.doi.org/10.1038/nature06843>.
- [8] S. C. Zhang, Physics **1**, 6 (2008).
- [9] J. E. Moore, Nature **464**, 194 (2010), URL <http://dx.doi.org/10.1038/nature08916>.
- [10] S. Murakami, Physical Review Letters **97**, 236805 (pages 4) (2006), URL <http://link.aps.org/abstract/PRL/v97/e236805>.
- [11] N. E. Ashcroft and N. D. Mermin, *Solid state physics* (Saunders College, Philadelphia, 1976), international ed.
- [12] C. Kittel, *Solid state physics* (Wiley, 1995).
- [13] G. D. Mahan, Physical Review B **2**, 4334 (1970).
- [14] B. Bransden and C. Joachain, *Physics of atoms and molecules*, Pearson Education (Longman, 1983), ISBN 9780582444010, URL [http://books.google.dk/books?id=b6x\\_z8nZbw0C](http://books.google.dk/books?id=b6x_z8nZbw0C).
- [15] P. Hofmann, *Solid State Physics. An Introduction* (Wiley-VCH Berlin, ISBN-10: 3-527-40861-4, 2008).

- [16] P. Hofmann, C. Søndergaard, S. Agergaard, S. V. Hoffmann, J. E. Gayone, G. Zampieri, S. Lizzit, and A. Baraldi, *Physical Review B* **66**, 245422 (2002).
- [17] L. F. J. Piper, L. Colakerol, P. D. C. King, A. Schleife, J. Zuniga-Perez, P.-A. Glans, T. Learmonth, A. Federov, T. D. Veal, F. Fuchs, et al., *Physical Review B* **78**, 165127 (pages 5) (2008), URL <http://link.aps.org/abstract/PRB/v78/e165127>.
- [18] P. D. C. King, T. D. Veal, D. J. Payne, A. Bourlange, R. G. Egdell, and C. F. McConville, *Phys. Rev. Lett.* **101**, 116808 (2008).
- [19] P. D. C. King, T. D. Veal, C. F. McConville, J. Zúñiga Pérez, V. Muñoz Sanjosé, M. Hopkinson, E. D. L. Rienks, M. F. Jensen, and P. Hofmann, *Phys. Rev. Lett.* **104**, 256803 (2010).
- [20] E. M. L. L. D. Landau, *Quantum Mechanics* (Pergamon Press, Oxford, 1991).
- [21] H. Zhang, C.-X. Liu, X.-L. Qi, X. Dai, Z. Fang, and S.-C. Zhang, *Nat Phys* **5**, 438 (2009), URL <http://dx.doi.org/10.1038/nphys1270>.
- [22] Y. Galperin, *Introduction to Modern Solid State Physics*.
- [23] J. Friedel, P. Lenglart, and G. Leman, *Journal of Physics and Chemistry of Solids* **25**, 781 (1964), ISSN 0022-3697, URL <http://www.sciencedirect.com/science/article/pii/0022369764900903>.
- [24] J. H. Dil, *Journal of Physics: Condensed Matter* **21**, 403001 (2009), URL <http://stacks.iop.org/0953-8984/21/i=40/a=403001>.
- [25] E. I. Rashba, *Soviet Physics - Solid State* **2**, 1109 (1960).
- [26] Y. A. Bychkov and E. I. Rashba, *Journal of Physics C - Condensed Matter Physics* **17**, 6039 (1984).
- [27] Y. A. Bychkov and E. I. Rashba, *JETP Letters* **39**, 78 (1984).
- [28] L. Petersen and P. Hedegard, *Surface Science* **459**, 49 (2000).
- [29] R. Winkler, *Spin-orbit coupling effects in two-dimensional electron and hole systems*, vol. 191 of *Springer Tracts in Modern Physics* (Springer-Verlag, Berlin, Heidelberg, 2003).
- [30] S. Datta and B. Das, *Appl. Phys. Lett.* **56**, 665 (1990).
- [31] S. LaShell, B. A. McDougall, and E. Jensen, *Physical Review Letters* **77**, 3419 (1996).
- [32] I. A. Nechaev, M. F. Jensen, E. D. L. Rienks, V. M. Silkin, P. M. Echenique, E. V. Chulkov, and P. Hofmann, *Physical Review B* **80**, 113402 (2009), URL <http://link.aps.org/abstract/PRB/v80/e113402>.
- [33] D. Guan, M. Bianchi, S. Bao, E. Perkins, F. Meier, J. H. Dil, J. Osterwalder, and P. Hofmann, *Phys. Rev. B* **83**, 155451 (2011).

- [34] J. B. Pendry and S. J. Gurman, *Surface Science* **49**, 87 (1975), URL <http://www.sciencedirect.com/science/article/...>
- [35] M. Z. Hasan and C. L. Kane, *Rev. Mod. Phys.* **82**, 3045 (2010).
- [36] J. C. Y. Teo, L. Fu, and C. L. Kane, *Physical Review B* **78**, 045426 (pages 15) (2008), URL <http://link.aps.org/abstract/PRB/v78/e045426>.
- [37] M. König, S. Wiedmann, C. Brune, A. Roth, H. Buhmann, L. W. Molenkamp, X.-L. Qi, and S.-C. Zhang, *Science* **318**, 766 (2007), URL <http://www.sciencemag.org/cgi/content/abstract/318/5851/766>.
- [38] T. Ando, Y. Matsumoto, and Y. Uemura, *Journal of the Physical Society of Japan* **39**, 279 (1975), URL <http://jpsj.ipap.jp/link?JPSJ/39/279/>.
- [39] K. v. Klitzing, G. Dorda, and M. Pepper, *Phys. Rev. Lett.* **45**, 494 (1980).
- [40] D. J. Thouless, M. Kohmoto, M. P. Nightingale, and M. den Nijs, *Phys. Rev. Lett.* **49**, 405 (1982), URL <http://link.aps.org/doi/10.1103/PhysRevLett.49.405>.
- [41] M. Kohmoto, *Annals of Physics* **160**, 343 (1985), ISSN 0003-4916, URL <http://www.sciencedirect.com/science/article/pii/0003491685901484>.
- [42] C. L. Kane and E. J. Mele, *Physical Review Letters* **95**, 146802 (pages 4) (2005), URL <http://link.aps.org/abstract/PRL/v95/e146802>.
- [43] J. Moore, *Nat Phys* **5**, 378 (2009), URL <http://dx.doi.org/10.1038/nphys1294>.
- [44] Y. L. Chen, J. H. Chu, J. G. Analytis, Z. K. Liu, K. Igarashi, H. H. Kuo, X. L. Qi, S. K. Mo, R. G. Moore, D. H. Lu, et al., *Science* **329**, 659 (2010), URL <http://www.sciencemag.org/cgi/content/abstract/329/5992/659>.
- [45] D. Hsieh, Y. Xia, L. Wray, D. Qian, A. Pal, J. H. Dil, J. Osterwalder, F. Meier, G. Bihlmayer, C. L. Kane, et al., *Science* **323**, 919 (2009), URL <http://www.sciencemag.org/cgi/content/abstract/323/5916/919>.
- [46] Y. Xia, D. Qian, D. Hsieh, L. Wray, A. Pal, H. Lin, A. Bansil, D. Grauer, Y. S. Hor, R. J. Cava, et al., *Nature Physics* **5**, 398 (2009), URL <http://dx.doi.org/10.1038/nphys1274>.
- [47] P. D. C. King, R. C. Hatch, M. Bianchi, R. Ovsyannikov, C. Lupulescu, G. Landolt, B. Slomski, J. H. Dil, D. Guan, J. L. Mi, et al., *Phys. Rev. Lett.* **107**, 096802 (2011).
- [48] S. K. Mishra, S. Satpathy, and O. Jepsen, *Journal of Physics: Condensed Matter* **9**, 461 (1997), URL <http://stacks.iop.org/0953-8984/9/i=2/a=014>.
- [49] G. Zhang, H. Qin, J. Teng, J. Guo, Q. Guo, X. Dai, Z. Fang, and K. Wu, *Applied Physics Letters* **95**, 053114 (2009).
- [50] H. Zhang, C.-X. Liu, X.-L. Qi, X. Dai, Z. Fang, and S.-C. Zhang, *Nature Physics* **5**, 438 (2009), URL <http://dx.doi.org/10.1038/nphys1270>.

- [51] S. Eremeev, Y. Koroteev, and E. Chulkov, *JETP Letters* **91**, 387 (2010), ISSN 0021-3640, 10.1134/S0021364010080059, URL <http://dx.doi.org/10.1134/S0021364010080059>.
- [52] M. Bianchi, R. C. Hatch, D. Guan, T. Planke, J. Mi, B. B. Iversen, and P. Hofmann, *Semiconductor Science and Technology* **27**, 124001 (2012), URL <http://stacks.iop.org/0268-1242/27/i=12/a=124001>.
- [53] Y. Liu and R. E. Allen, *Physical Review B* **52**, 1566 (1995).
- [54] L. M. Falicov and P. J. Lin, *Phys. Rev.* **141**, 562 (1966).
- [55] A. Einstein, *Annalen der Physik* **322**, 132 (1905).
- [56] R. D. Mattuck, *A guide to Feynmann diagrams in the many-body problem* (Dover Publications, 1992).
- [57] G. Grimvall, *The electron-phonon interaction in metals* (North-Holland, 1981).
- [58] P. Hofmann, I. Y. Sklyadneva, E. D. L. Rienks, and E. V. Chulkov, *New Journal of Physics* **11**, 125005 (2009), URL <http://stacks.iop.org/1367-2630/11/i=12/a=125005>.
- [59] C. Kirkegaard, T. K. Kim, and P. Hofmann, *New Journal of Physics* **7**, 99 (2005).
- [60] G. E. Shoemaker, J. A. Rayne, and R. W. Ure, *Phys. Rev.* **185**, 1046 (1969).
- [61] B. K. Agarval, *X-Ray Spectroscopy*, Second ed. (Springer-Verlag, Berlin, 1991).
- [62] S. Doniach and M. Sunjic, *Journal of Physics C: Solid State Physics* **3**, 285 (1970).
- [63] L. Hedin and A. Rosengren, *Journal of Physics F: Metal Physics* **7**, 1339 (1977), URL <http://stacks.iop.org/0305-4608/7/i=7/a=032>.
- [64] S. V. Hoffmann, C. Søndergaard, C. Schultz, Z. Li, and P. Hofmann, *Nuclear Inst. and Methods in Physics Research, A* **523**, 441 (2004).
- [65] URL <http://www.isa.au.dk>.
- [66] J. A. Clarke, *The science and technology of undulators and wigglers*, Oxford series on synchrotron radiation (Oxford University Press, Oxford, 2004), URL <http://dx.doi.org/10.1093/acprof:oso/9780198508557.001.0001>.
- [67] K. Wille, *Rept.Prog.Phys.* **54**, 1005 (1991).
- [68] S. Krinsky, J. Bittner, A. M. Fauchet, E. D. Johnson, J. Keane, J. Murphy, R. J. Nawrocky, J. Rogers, O. V. Singh, and L. H. Yu, in *American Institute of Physics Conference Series* (1992), vol. 249 of *American Institute of Physics Conference Series*, pp. 762–858.
- [69] D. P. Woodruff and T. A. Delchar, *Modern techniques of surface science - second edition* (Cambridge University Press, 1994).

- [70] S. Hüfner, *Photoelectron spectroscopy* (Springer, Berlin, 2003), 3rd ed.
- [71] T. C. Chiang, *Surface Science Reports* **39**, 181 (2000), ISSN 0167-5729.
- [72] K. Sugawara, T. Sato, S. Souma, T. Takahashi, M. Arai, and T. Sasaki, *Physical Review Letters* **96**, 046411 (2006).
- [73] S. Agergaard, C. Søndergaard, H. Li, M. B. Nielsen, S. V. Hoffmann, Z. Li, and P. Hofmann, *New Journal of Physics* **3**, 15.1 (2001).
- [74] J. W. Wells, J. H. Dil, F. Meier, J. Lobo-Checa, V. N. Petrov, J. Osterwalder, M. M. Ugeda, I. Fernandez-Torrente, J. I. Pascual, E. D. L. Rienks, et al., *Physical Review Letters* **102**, 096802 (pages 4) (2009), URL <http://link.aps.org/abstract/PRL/v102/e096802>.
- [75] Y. M. Koroteev, G. Bihlmayer, J. E. Gayone, E. V. Chulkov, S. Blügel, P. M. Echenique, and P. Hofmann, *Physical Review Letters* **93**, 046403 (2004).
- [76] P. Hofmann, *Progress in Surface Science* **81**, 191 (2006), ISSN 5.
- [77] M. Bianchi, D. Guan, A. Stróżecka, C. H. Voetmann, S. Bao, J. I. Pascual, A. Eiguren, and P. Hofmann, *Phys. Rev. B* **85**, 155431 (2012), URL <http://link.aps.org/doi/10.1103/PhysRevB.85.155431>.
- [78] Y. L. Chen, J. G. Analytis, J. H. Chu, Z. K. Liu, S. K. Mo, X. L. Qi, H. J. Zhang, D. H. Lu, X. Dai, Z. Fang, et al., *Science* **325**, 178 (2009), URL <http://www.sciencemag.org/cgi/content/abstract/325/5937/178>.
- [79] D. Hsieh, Y. Xia, D. Qian, L. Wray, J. H. Dil, F. Meier, J. Osterwalder, L. Patthey, J. G. Checkelsky, N. P. Ong, et al., *Nature* **460**, 1101 (2009), URL <http://dx.doi.org/10.1038/nature08234>.
- [80] S. G. Louie, P. Thiry, R. Pinchaux, Y. Petroff, D. Chandleris, and J. Lecante, *Physical Review Letters* **44**, 549 (1980).
- [81] J. Navrátil, J. Horák, T. Plecháček, S. Kamba, P. Losták, J. Dyck, W. Chen, and C. Uher, *Journal of Solid State Chemistry* **177**, 1704 (2004), ISSN 0022-4596.
- [82] K. Kuroda, M. Arita, K. Miyamoto, M. Ye, J. Jiang, A. Kimura, E. E. Krasovskii, E. V. Chulkov, H. Iwasawa, T. Okuda, et al., *Phys. Rev. Lett.* **105**, 076802 (2010).
- [83] L. Fu, *Phys. Rev. Lett.* **103**, 266801 (2009).
- [84] Y. S. Hor, A. Richardella, P. Roushan, Y. Xia, J. G. Checkelsky, A. Yazdani, M. Z. Hasan, N. P. Ong, and R. J. Cava, *Phys. Rev. B* **79**, 195208 (2009).
- [85] M. Bianchi, D. Guan, S. Bao, J. Mi, B. B. Iversen, P. D. C. King, and P. Hofmann, *Nature Communications* **1**, 128 (2010).
- [86] R. W. G. Wyckoff, *Crystal structures*, vol. 2 (Interscience, 1963).
- [87] C. R. Ast, J. Henk, A. Ernst, L. Moreschini, M. C. Falub, D. Pacile, P. Bruno, K. Kern, and M. Grioni, *Physical Review Letters* **98**, 186807 (2007).

- [88] P. D. C. King, T. D. Veal, and C. F. McConville, *Physical Review B* **77**, 125305 (pages 7) (2008), URL <http://link.aps.org/abstract/PRB/v77/e125305>.
- [89] P. Cheng, C. Song, T. Zhang, Y. Zhang, Y. Wang, J.-F. Jia, J. Wang, Y. Wang, B.-F. Zhu, X. Chen, et al., *Phys. Rev. Lett.* **105**, 076801 (2010).
- [90] H.-J. Noh, H. Koh, S.-J. Oh, J.-H. Park, H.-D. Kim, J. D. Rameau, T. Valla, T. E. Kidd, P. D. Johnson, Y. Hu, et al., *Europhysics Letters* **81**, 57006 (2008), URL <http://stacks.iop.org/0295-5075/81/i=5/a=57006>.
- [91] D. Hsieh, Y. Xia, D. Qian, L. Wray, F. Meier, J. H. Dil, J. Osterwalder, L. Patthey, A. V. Fedorov, H. Lin, et al., *Physical Review Letters* **103**, 146401 (pages 4) (2009), URL <http://link.aps.org/abstract/PRL/v103/e146401>.
- [92] S. V. Eremeev, M. G. Vergniory, T. V. Menshchikova, A. A. Shaposhnikov, and E. V. Chulkov, *New Journal of Physics* **14**, 113030 (2012), URL <http://stacks.iop.org/1367-2630/14/i=11/a=113030>.
- [93] N. Fukui, T. Hirahara, T. Shirasawa, T. Takahashi, K. Kobayashi, and S. Hasegawa, *Phys. Rev. B* **85**, 115426 (2012), URL <http://link.aps.org/doi/10.1103/PhysRevB.85.115426>.
- [94] T. Schlenk, M. Bianchi, M. Koleini, A. Eich, O. Pietzsch, T. O. Wehling, T. Frauenheim, A. Balatsky, J.-L. Mi, B. B. Iversen, et al., *ArXiv e-prints* (2012), 1211.2142.
- [95] T. Koga, J. Nitta, H. Takayanagi, and S. Datta, *Physical Review Letters* **88**, 126601 (2002).
- [96] J. Wunderlich, B.-G. Park, A. C. Irvine, L. P. Zárbo, E. Rozkotová, P. Nemeč, V. Novák, J. Sinova, and T. Jungwirth, *Science* **330**, 1801 (2010), URL <http://www.sciencemag.org/content/330/6012/1801.abstract>.
- [97] H.-C. Chang, H. H. Richardson, and G. E. Ewing, *The Journal of Chemical Physics* **89**, 7561 (1988), URL <http://link.aip.org/link/?JCP/89/7561/1>.
- [98] M. Pan, S. Hoang, J. Gong, and C. B. Mullins, *Chem. Commun.* **0**, 7300 (2009), URL <http://dx.doi.org/10.1039/B914308D>.
- [99] H. M. Benia, C. Lin, K. Kern, and C. R. Ast, *Phys. Rev. Lett.* **107**, 177602 (2011), URL <http://link.aps.org/doi/10.1103/PhysRevLett.107.177602>.
- [100] E. I. Vul, B. M. Zavaritskaya and V. N. Zavaritskii, *JETP Letters* **35**, 259 (1978).
- [101] B. Vul and E. Zavaritskaya, *JETP Letters* **27**, 547 (1982).
- [102] M. S. Bahramy, P. D. C. King, A. de la Torre, J. Chang, M. Shi, L. Patthey, G. Balakrishnan, P. Hofmann, R. Arita, N. Nagaosa, et al., *Nat Commun* **3** (2012), URL <http://dx.doi.org/10.1038/ncomms2162>.
- [103] L. A. Wray, S.-Y. Xu, Y. Xia, D. Hsieh, A. V. Fedorov, Y. S. Hor, R. J. Cava, A. Bansil, H. Lin, and M. Z. Hasan, *Nature Physics* **7**, 32 (2011), URL <http://dx.doi.org/10.1038/nphys1838>.

- [104] D. A. Abanin and D. A. Pesin, *Phys. Rev. Lett.* **106**, 136802 (2011).
- [105] Y. S. Hor, A. J. Williams, J. G. Checkelsky, P. Roushan, J. Seo, Q. Xu, H. W. Zandbergen, A. Yazdani, N. P. Ong, and R. J. Cava, *Phys. Rev. Lett.* **104**, 057001 (2010).
- [106] M. Hoesch, T. Greber, V. Petrov, A. Muntwiler, M. Hengsberger, W. Auwärter, and J. Osterwalder, *Journal of Electron Spectroscopy and Related Phenomena* **124**, 263 (2002), ISSN 0368-2048.
- [107] F. Meier, H. Dil, J. Lobo-Checa, L. Patthey, and J. Osterwalder, *Physical Review B* **77**, 165431 (pages 7) (2008), URL <http://link.aps.org/abstract/PRB/v77/e165431>.
- [108] G. Öhrwall, P. Karlsson, M. Wirde, M. Lundqvist, P. Andersson, D. Ceolin, B. Wannberg, T. Kachel, H. Dürr, W. Eberhardt, et al., *Journal of Electron Spectroscopy and Related Phenomena* **183**, 125 (2011), ISSN 0368-2048, URL <http://www.sciencedirect.com/science/article/pii/S0368204810002045>.
- [109] E. A. de Andrada e Silva, G. C. La Rocca, and F. Bassani, *Phys. Rev. B* **50**, 8523 (1994), URL <http://link.aps.org/doi/10.1103/PhysRevB.50.8523>.
- [110] E. A. de Andrada e Silva, G. C. La Rocca, and F. Bassani, *Phys. Rev. B* **55**, 16293 (1997), URL <http://link.aps.org/doi/10.1103/PhysRevB.55.16293>.
- [111] E. O. Kane, *J. Phys. Chem. Solids.* **1**, 249 (1957).
- [112] A. Bostwick, T. Ohta, J. L. McChesney, T. Seyller, K. Horn, and E. Rotenberg, **148** (2007), URL <http://dx.doi.org/10.1140/epjst/e2007-00220-x>.
- [113] M. Bianchi, E. D. L. Rienks, S. Lizzit, A. Baraldi, R. Balog, L. Hornekær, and P. Hofmann, *Phys. Rev. B* **81**, 041403 (2010).
- [114] M. Ye, S. V. Eremeev, K. Kuroda, M. Nakatake, S. Kim, Y. Yamada, E. E. Krasovskii, E. V. Chulkov, M. Arita, H. Miyahara, et al., *ArXiv e-prints* 1112.5869 (2011), [arXiv/1112.5869](http://arXiv/1112.5869).
- [115] T. Valla, Z.-H. Pan, D. Gardner, Y. S. Lee, and S. Chu, *Phys. Rev. Lett.* **108**, 117601 (2012), URL <http://link.aps.org/doi/10.1103/PhysRevLett.108.117601>.
- [116] Z.-H. Zhu, G. Levy, B. Ludbrook, C. N. Veenstra, J. A. Rosen, R. Comin, D. Wong, P. Dosanjh, A. Ubaldini, P. Syers, et al., *Phys. Rev. Lett.* **107**, 186405 (2011), URL <http://link.aps.org/doi/10.1103/PhysRevLett.107.186405>.
- [117] C.-L. Song, B. Sun, Y.-L. Wang, Y.-P. Jiang, L. Wang, K. He, X. Chen, P. Zhang, X.-C. Ma, and Q.-K. Xue, *Phys. Rev. Lett.* **108**, 156803 (2012), URL <http://link.aps.org/doi/10.1103/PhysRevLett.108.156803>.
- [118] A. L. Walter, K.-J. Jeon, A. Bostwick, F. Speck, M. Ostler, T. Seyller, L. Moreschini, Y. S. Kim, Y. J. Chang, K. Horn, et al., *Applied Physics Letters* **98**, 184102 (pages 3) (2011), URL <http://link.aip.org/link/?APL/98/184102/1>.

- [119] N. A. Vinogradov, K. A. Simonov, A. V. Generalov, A. S. Vinogradov, D. V. Vyalikh, C. Laubschat, N. Martensson, and A. B. Preobrajenski, *J Phys Condens Matter* **24**, 314202 (2012).
- [120] J. Honolka, A. A. Khajetoorians, V. Sessi, T. O. Wehling, S. Stepanow, J.-L. Mi, B. B. Iversen, T. Schlenk, J. Wiebe, N. B. Brookes, et al., *Phys. Rev. Lett.* **108**, 256811 (2012), URL <http://link.aps.org/doi/10.1103/PhysRevLett.108.256811>.
- [121] Y. Okada, C. Dhital, W. Zhou, E. D. Huemiller, H. Lin, S. Basak, A. Bansil, Y.-B. Huang, H. Ding, Z. Wang, et al., *Phys. Rev. Lett.* **106**, 206805 (2011).
- [122] D. West, Y. Y. Sun, S. B. Zhang, T. Zhang, X. Ma, P. Cheng, Y. Y. Zhang, X. Chen, J. F. Jia, and Q. K. Xue, *Phys. Rev. B* **85**, 081305 (2012), URL <http://link.aps.org/doi/10.1103/PhysRevB.85.081305>.
- [123] C.-L. Song, Y.-P. Jiang, Y.-L. Wang, Z. Li, L. Wang, K. He, X. Chen, X.-C. Ma, and Q.-K. Xue, *Phys. Rev. B* **86**, 045441 (2012), URL <http://link.aps.org/doi/10.1103/PhysRevB.86.045441>.
- [124] M. R. Scholz, J. Sánchez-Barriga, D. Marchenko, A. Varykhalov, A. Volykhov, L. V. Yashina, and O. Rader, *Phys. Rev. Lett.* **108**, 256810 (2012), URL <http://link.aps.org/doi/10.1103/PhysRevLett.108.256810>.
- [125] R. C. Hatch, M. Bianchi, D. Guan, S. Bao, J. Mi, B. B. Iversen, L. Nilsson, L. Hornekær, and P. Hofmann, *Phys. Rev. B* **83**, 241303 (2011).
- [126] A. Eiguren, B. Hellsing, E. V. Chulkov, and P. M. Echenique, *Physical Review B* **67**, 235423 (2003).
- [127] F. Reinert, G. Nicolay, S. Schmidt, D. Ehm, and S. Hübner, *Physical Review B* **63**, 115415 (2001).
- [128] S. Kevan, *Physical Review B* **33**, 4364 (1986).
- [129] S. V. Eremeev, G. Landolt, T. V. Menshchikova, B. Slomski, Y. M. Koroteev, Z. S. Aliev, M. B. Babanly, J. Henk, A. Ernst, L. Patthey, et al., *Nat Commun* **3** (2012), URL <http://dx.doi.org/10.1038/ncomms1638>.
- [130] G. Schubert, H. Fehske, L. Fritz, and M. Vojta, *Phys. Rev. B* **85**, 201105 (2012), URL <http://link.aps.org/doi/10.1103/PhysRevB.85.201105>.
- [131] V. A. Greanya, W. C. Tonjes, R. Liu, C. G. Olson, D.-Y. Chung, and M. G. Kanatzidis, *Journal of Applied Physics* **92**, 6658 (2002), URL <http://link.aip.org/link/?JAP/92/6658/1>.
- [132] P. Larson, V. A. Greanya, W. C. Tonjes, R. Liu, S. D. Mahanti, and C. G. Olson, *Phys. Rev. B* **65**, 085108 (2002), URL <http://link.aps.org/doi/10.1103/PhysRevB.65.085108>.
- [133] I. A. Nechaev, R. C. Hatch, M. Bianchi, D. Guan, C. Friedrich, I. Aguilera, J. L. Mi, B. B. Iversen, S. Blügel, P. Hofmann, et al., arXiv:1210.4477v1 (2012).

- [134] L. A. Wray, S.-Y. Xu, Y. Xia, Y. S. Hor, D. Qian, A. V. Fedorov, H. Lin, A. Bansil, R. J. Cava, and M. Z. Hasan, *Nature Physics* **advance online publication**, (2010), URL <http://dx.doi.org/10.1038/nphys1762>.
- [135] S. Kim, M. Ye, K. Kuroda, Y. Yamada, E. E. Krasovskii, E. V. Chulkov, K. Miyamoto, M. Nakatake, T. Okuda, Y. Ueda, et al., *Phys. Rev. Lett.* **107**, 056803 (2011).
- [136] A. Varykhalov, J. Sánchez-Barriga, A. M. Shikin, C. Biswas, E. Vescovo, A. Rybkin, D. Marchenko, and O. Rader, *Phys. Rev. Lett.* **101**, 157601 (2008), URL <http://link.aps.org/doi/10.1103/PhysRevLett.101.157601>.
- [137] P. Zhang, P. Richard, T. Qian, Y.-M. Xu, X. Dai, and H. Ding, *Review of Scientific Instruments* **82**, 043712 (pages 7) (2011), URL <http://link.aip.org/link/?RSI/82/043712/1>.
- [138] K. Capelle, *Brazilian Journal of Physics* **36**, 1318 (2006), ISSN 0103-9733.
- [139] R. Sakuma, C. Friedrich, T. Miyake, S. Blügel, and F. Aryasetiawan, *Phys. Rev. B* **84**, 085144 (2011), URL <http://link.aps.org/doi/10.1103/PhysRevB.84.085144>.
- [140] O. V. Yazyev, E. Kioupakis, J. E. Moore, and S. G. Louie, *Phys. Rev. B* **85**, 161101 (2012), URL <http://link.aps.org/doi/10.1103/PhysRevB.85.161101>.